UNIVERSITÀ
DEGLI STUDI
FIRENZE

DOTTORATO DI RICERCA IN
FISICA E ASTRONOMIA

CICLO_XXXIV

COORDINATORE Prof. Raffaello D'Alessandro

Accretion on all time scales, from TDEs to QSOs

Settore Scientifico Disciplinare FIS05

Dottorando
Dott. *Sacchi Andrea*
(firma)

Tutore
Prof. Risaliti Guido
(firma)

Coordinatore
Prof. *D'Alessandro Raffaello*
(firma)

Anni 2018/2021

Contents

Abstract

Supermassive black holes are amongst the most energetic and interesting astrophysical objects in our known Universe. Their study, started almost a century ago, shed light on several aspects of their nature, both through theoretical and observational means. However many others remain mysteries.
One of the most interesting feature these objects exhibit is the wide variety in the time scales of their accretion: supermassive black hole can be found accreting material regularly, keeping a steady-state across centuries, or being in a non-accreting state for as much long; or they can suddenly burst, emitting in days the energy hundreds of galaxies emit in years, along with all the intermediate states.
This thesis addresses the matter of accretion on different time scales mainly by focusing on two phenomena: tidal disruption events and quasi-stellar objects. Both phenomena indicates supermassive black holes accreting at time scales which differ by several orders of magnitudes.
This thesis is, as the entire supermassive black hole research field is, a multi-technique work, coupling theoretical analysis, numerical simulations, observational efforts and catalog searches in order to investigate these most interesting titanic monsters.

Introduction

Most of the known galaxy are thought to be hosting a supermassive black hole (SMBH), with a mass ranging from millions to billions of solar masses, at their centre. A fraction of these SMBHs are surrounded by a thick torus of material feeding an accretion disk and thus powering accretion processes which are "stable" on decades and centuries time-scales (Antonucci, 1993; Urry & Padovani, 1995). For this fraction of SMBHs, hosted in active galactic nuclei (AGN), direct investigation is possible. For the vast majority of SMBHs however, which are in a dormant state (like for example the SMBH hosted by the Milky Way, Sgr A*), direct investigation is not possible at all times. Nonetheless every SMBH, residing in the crowded environment of a galactic nucleus, is surrounded by orbiting stars. If one of these stars wonders too close to the hole, it will get destroyed by tidal forces and its debris will be partially accreted, generating bright electromagnetic emission, neutrinos and possibly gravitational waves. Theses rare phenomena, called tidal disruption events (TDEs), allow us to study otherwise quiescent SMBHs, even if only over a narrow time window, through all sort of different messengers.

This thesis aim is to exploit both presented scenarios, exploring accretion phenomena onto SMBHs thanks to the persistent emission of AGN and the transient one of TDEs, across a wide range of temporal regimes, from the days/weeks time-scale of the latter to decades/centuries of the former. At the same time this thesis mirrors the research path followed by the author, transitioning from a theoretical approach, supported by numerical simulations, to an observational investigation, corroborated by X-rays data analysis.

The first part of this thesis, which includes the initial three chapters, is focused on TDEs. Chapter 1 and 2 exploit theoretical efforts and N-bodies numerical simulations, while Chapter 3 focuses on a more observational approach, based on the search for overlooked TDE in X-rays archival observations. The second part of the thesis, composed by the two final chapters, is centred on QSOs, in particular on the possibility of using these sources as standard candles in cosmological studies. Both Chapter 4 and 5 heavily rely on the usage and analysis of X-rays as well optical/UV catalogs of AGN.

Chapter 1 is focused on the role of an initial proper rotation of the star which is going to be disrupted by the black hole in the TDE. In particular we focused on a configuration in which the initial stellar rotation is opposing the tidal forces imposed on the star by the hole.

Through analytical arguments and numerical simulations we found out that if the star is spinning with sufficient velocity, although some material gets ripped off the stellar core, no disruption is to be expected and no material will be accreted onto the hole. On the contrary the stripped stellar material will eventually fall back onto its core generating a smaller-scale accretion disc. Through qualitative analysis we predict the spectrum for the emission of this stellar disc to peak in the X-rays band and its luminosity to be consistently above the Eddington value for the star.

Furthermore the stellar core, which at the beginning of our simulations moves on a unbound parabolic trajectory with respect to the black hole, will end up on a highly eccentric close orbit and will eventually come back to be disrupted during subsequent flybys of the black hole.

The results described in this chapter have been published in Sacchi & Lodato 2019.

Chapter 2 faces the problem of gravitational instability tidal debris. After a star gets destroyed by a SMBH roughly half of the stellar debris get ejected while the other half will come back to the hole to be circularized in an accretion disc and eventually swallowed. Traveling around the hole, both bound and unbound debris form a stretching cylinder. Investigating the physical properties of this structure is crucial as they will ultimately affect the observational outcome of the TDE.

In particular, previous literature results predict that if the stream of stellar debris undergoes fragmentation, forming a string of beads rather than a continuous stream of gas, this will result in a series of micro-TDEs increasing the overall luminosity of the main event. Literature also provides a criterion to determine whether the debris stream will collapse under its self-gravity or not, unfortunately it has two main flows: it only accounts for the tidal forces generated by the hole, neglecting the stream pressure and dynamic; in the case we are most interested in, such as the case of adiabatic gas, this is only a necessary and not sufficient condition for fragmentation.

The aim of our work was both to understand whether the adiabatic case is susceptible of fragmentation and to identify a satisfying criterion for the collapse of tidal debris streams. We did so by analytical investigation as well as high resolution numerical simulations in order to account for every effect that could play an import role in our scenario: the stream stretching, its internal pressure and self-gravity and the hole tides.

Thanks to this approach we were able to identify a solid criterion for fragmentation based on the results obtained in the 70s in star formation studies. We also

found that, in the adiabatic case, although fragmentation occurs in the stream of debris, it only affects the unbound part of it, hence no observational outcome is to be expected by the stream self-gravity induced collapse.

The results described in this chapter have been published in Sacchi et al. 2020.

Chapter 3 represents a bridge between the TDE and AGN souls of this thesis. We searched the more than 5.5×10^5 X-ray sources of the latest XMM-Newton catalogue searching for potentially interesting objects ranging from overlooked thermal TDEs to supersoft AGN that often exhibit peculiar spectral and variability properties.

We obtained a final sample of 60 sources sharing similar spectral features and X-ray luminosities well above 10^{41} erg/s. Out of these 60 sources, 15 turned out to be well known TDEs, TDE candidates, or AGNs with extreme spectral/variability properties, confirming that our selection criteria indeed reveal the correct population of X-ray sources. By performing a complete X-ray spectral analysis of the remaining 45 sources, we identified 9 sources with spectral properties that most significantly deviate from the expected behavior based on optical classification and/or that do not resemble those of standard AGNs. Among these 4 sources show the typical spectral appearance of thermal TDEs.

Chapter 4 is nested in a series of works which explore and exploit the non-linear relation between UV and X-rays luminosity of QSOs. This observed relation allows to use the QSOs as "standardizable" candles and in principle could prolong the Hubble-Lemaître diagram way deeper than z=2. The relation has been well known for more than forty years, but only since 2015 our group has been able to exploit it efficiently by proving that the observed dispersion is mostly attributable to observational issues and can therefore be significantly reduced by cleaning wisely the sample of source one is working with.

In this picture this chapter aims at enlarging the sample of QSOs for cosmological studies. We did so by employing the latest catalogs of optical/UV and X-rays observations as well as the largest available compilation QSOs, the MILLIQUAS catalog. By doing so we were able to double the dimension of the latest published version of our sample, going from $\sim$ 2000 QSOs to more than 5000.

Chapter 5, as the previous one, is focused on the luminosities relation of QSOs. As said, the observed non-linear relation between UV and X-rays luminosities of QSOs has been well know for more than forty years but we still lack of a convincing model able to explain it. This makes difficult convincing the most sceptical minds in the scientific community about the solidity of the usage of cosmological QSOs. One way to solve this problem is to prove beyond any doubts that the luminosities relation dispersion disappears when one is able to remove all observational issues.

We show that by choosing a narrow bin at high redshift where we have high quality observations we are able to reduce the dispersion to never before reached values. This residual dispersion can be proven to be entirely due to the intrinsic variability and inclination effects of the sources.

Our work hence achieves a double goal: on the one hand it proves that the relation, although lacking a fully convincing physical explanation, can be solidly employed for cosmological studies; on the other hand that given enough high quality observations one can remove all observational issues and reduce the dispersion and therefore the power of the QSOs as cosmological probes.

1 "Failed" tidal disruption events and X-ray flares from the Galactic Center

The process of tidal disruption of stars by a supermassive black hole (SMBH) provides luminous UV and soft X-ray flares with peak luminosities of $\approx 10^{46}$ ergs/sec and duration of a few months. As part of a wider exploration of the effects of stellar rotation on the outcome of a TDE, we have performed hydrodynamical simulations of the disruption of a rotating star whose spin axis is opposite to the orbital axis. Such a retrograde rotation makes the star more resilient to tidal disruption, so that, even if its orbit reaches the formal tidal radius, it actually stays intact after the tidal encounter. However, the outer layers of the star are initially stripped away from the core, but then fall back onto the star itself, producing a newly formed accretion disc around the star. We estimate that the accretion rate onto the star would be strongly super-Eddington (for the star) and would result in an X-ray flare with luminosity of the order of $\approx 10^{40}$ ergs/sec and duration of a few months. We speculate that such events might be responsible for the known X-ray flares from Sgr A* in the recent past.

1.1 - Introduction

In the last two decades a new class of X-ray outbursts have started to be detected (Bade et al., 1996; Gezari et al., 2003). Having high variability (with timescales ranging from weeks to even a few days) and bright but soft spectrum ($L \geq 10^{42\text{-}43}$ erg/s) along with other unusual characteristics, such as no sign of Seyfert activity of the host galaxy, the explanation for these events has to be sought in the then uncharted class of phenomena of tidal disruption events (TDEs).

These events happen when the strong gravity of a supermassive black hole (SMBH) disrupts a passing star through tidal forces, if the latter approaches the compact object at a distance smaller than the SMBH's tidal radius, which is the distance at which the tidal force equals the stellar self-gravity.

Several putative TDEs have been found, observed in almost every band of the

electromagnetic spectrum: soft X-ray (Bade et al., 1996), optical and UV (Gezari, 2012; Komossa, 2012, 2015; Hung et al., 2017), radio (Zauderer et al., 2011), hard X-ray and gamma (Bloom et al., 2011; Cenko et al., 2012; Brown et al., 2015; Auchettl et al., 2017; Blagorodnova et al., 2017). However, TDEs had been studied for almost twenty years before the observational discovery, both from a theoretical point of view (Lacy et al., 1982; Rees, 1988; Phinney, 1989) and through numerical simulations (Carter & Luminet, 1982, 1983; Evans & Kochanek, 1989), due to their importance as a tool to study the properties of BHs, especially in the center of galaxies.

In the simplest theoretical scenario, a star in hydrostatic equilibrium is set on a parabolic orbit around a SMBH, with pericenter distance equal to the tidal radius. Under the impulse approximation (Rees, 1988), meaning that the interaction between the two objects occurs instantaneously rather than gradually as the star approaches the SMBH, the former remains unperturbed up to the pericenter, where it is tidally disrupted. After that, roughly half of the stellar material is launched onto hyperbolic orbits allowing the debris to escape the system, while the other half remains bound to the SMBH in highly elliptical orbits and therefore will eventually return to the compact object forming a bright accretion disc. The most bound material is the first to complete its orbit and accrete onto the black hole.

Under the assumption that the time the debris need to form the disc and accrete onto the black hole is much shorter than the time it takes to complete the elliptical orbit, the luminosity of the event is found to be proportional to the mass return rate at the pericentre:

$$L \propto \frac{\mathrm{d}M}{\mathrm{d}t} \propto \frac{\mathrm{d}M}{\mathrm{d}E} t^{-5/3}. \tag{1.1}$$

Assuming the flatness of the energy distribution, it is possible to find what is considered to be the "smoking gun" of these phenomena: a light curve that should fall as $t^{-5/3}$. Results from numerical simulations and analytical considerations, however, found that these phenomena depend on a wide range of parameters, such as the stellar internal structure (Lodato et al., 2009), the properties of the black hole (Hayasaki et al., 2016; Tejeda et al., 2017), the penetration factor $\beta = R_{\mathrm{t}}/R_{\mathrm{p}}$ (where R_{t} is the tidal radius and R_{p} is the pericentre distance) (Guillochon & Ramirez-Ruiz, 2013) and the physics of disc formation (Hayasaki et al., 2013; Bonnerot et al., 2016), that can consistently modify the $t^{-5/3}$ behavior.

Interestingly, the very first theoretical investigations on this subject had our own Galactic Center in mind as a possible source of TDEs (Lacy et al., 1982). However, no TDE has ever been observed from our galactic center (although some recent flare have been associated with the tidal disruption of asteroids Kostić et al. 2012). There is however evidence of past activity from Sgr A* in the form of rapid flare and variability, that can be inferred based on the echo that these flares produce on

the surrounding medium. In particular, Churazov et al. (2017) argue that a recent X-ray flare has occurred in the Galactic center. Thanks to X-ray observations of the molecular clouds near the Galactic Center they were able to infer that these clouds reflect emission originating ≈ 110 years ago from the central black hole in our Galaxy. They conclude that the original flare had a luminosity of $\approx 10^{41}$ erg/s in the 1-100 keV band, and lasted for a period of less then a few years.

Theoretical investigations of the disruption of stars by supermassive black holes have concentrated mostly on the case where the star does not possess a spin and, while basic dynamical arguments readily show that a TDE induces a spin in the disrupted star (in the same sense of the orbital angular momentum), only a couple of works (Golightly et al., 2019; Kagaya et al., 2019) to date investigated the effect of stellar spin on the TDE characteristics (and only over a limited range of parameters). In this Chapter, we concentrate on one specific setup, in which the stellar rotation axis is antiparallel to the orbital angular momentum of the star, so that the spin is retrograde with respect to the orbit. We show that such a configuration can lead to a "failed" TDE, where a star with $\beta = 1$ (which would be disrupted in the absence of spin) can survive the encounter with the SMBH and rather produce a fainter flare, whose features resemble the observed flares from Sgr A*.

This work is divided as follow: in Section 1.2 we will present the standard picture of TDEs and how an initial stellar rotation can suppress the disruption; in Section 1.3 we will discuss the numerical setup used in our simulations; finally in Section 1.4 there will be a discussion of our results and our conclusions.

1.2 - **Analytical estimates**

In this section we briefly summarize the standard analytical estimates on TDE dynamics, mainly following the approach of Rees (1988). We will also give a taste of the relation between tides and rotation and then we will show how an initial stellar rotation affects these estimates and how it can even suppress a TDE.

1.2.1 *The standard picture*

Let us consider a star, of radius $R_\star$ and mass $M_\star$, on a parabolic orbit around a black hole of mass M_h. If the orbital pericenter is within the tidal radius:

$$R_\mathrm{t} \simeq R_\star \left(\frac{M_\mathrm{h}}{M_\star}\right)^{1/3} \approx 0.5\,\mathrm{AU} \left(\frac{R_\star}{R_\odot}\right) \left(\frac{M_\mathrm{h}}{10^6\,M_\odot}\right)^{1/3} \left(\frac{M_\star}{M_\odot}\right)^{-1/3}, \qquad (1.2)$$

the distance at which tidal forces equal the stellar self-gravity, the star will be destroyed by the black hole tidal forces. After the disruption roughly half of the

stellar debris will be launched on hyperbolic orbits, while the remaining half will be bound to the black hole. These bound debris will form an accretion disc around the black hole (Bonnerot et al., 2016) and eventually they will get accreted.

In the simplest scenario it is possible to estimate the lightcurve of the event through the mass return rate at pericenter: the two quantities will be proportional under the assumption that the circularization and accretion time are considerably shorter than the orbital period of the debris. While the validity of the previous assumptions is currently under debate (the disc might not form efficiently, Svirski et al. 2017, and even if the disc forms the single wavelength lightcurve might deviate significantly from the bolometric behaviour, Lodato & Rossi 2011), there is some empirical evidence that the optical luminosity does follow approximately the behaviour predicted analytically, hence giving credit that it might be related directly to the fallback process (Lodato, 2012). In this picture, the luminosity of the event will scale as the rate at which the stellar debris fall back onto the black hole, which is easily computed from Kepler's third law, assuming the debris to follow Keplerian orbits after disruption. This gives the standard result

$$L \propto \frac{\mathrm{d}M}{\mathrm{d}t} = \frac{(2\pi G M_{\mathrm{h}})^{2/3}}{3} \frac{\mathrm{d}M}{\mathrm{d}E} t^{-5/3}. \tag{1.3}$$

The energy spread ΔE of the debris right before the disruption is determined only by how deep in the potential well the debris are. It is therefore possible to estimate the energy spread in a straightforward way as

$$\Delta E = \left.\frac{\mathrm{d}E_{\mathrm{p}}}{\mathrm{d}r}\right|_{R_{\mathrm{p}}} \Delta r = \frac{G M_{\mathrm{h}}}{R_{\mathrm{p}}^2} R_{\star}, \tag{1.4}$$

where R_{p} is the pericentre distance of the orbit. Defining the minimum return time

$$t_{\mathrm{min}} = \frac{2\pi G M_{\mathrm{h}}}{(2\Delta E)^{3/2}}, \tag{1.5}$$

as the time it takes for the first debris to come back at pericenter and the fallback peak rate

$$\dot{M}_{\mathrm{p}} = \frac{M_{\star}}{3 t_{\mathrm{min}}}, \tag{1.6}$$

it is possible to write down the fallback rate in a compact way as follow:

$$\frac{\mathrm{d}M}{\mathrm{d}t} = \dot{M}_{\mathrm{p}} \left(\frac{t}{t_{\mathrm{min}}}\right)^{-5/3} \tag{1.7}$$

This result and the $-5/3$ power-law time decay has been traditionally considered the signature of TDE (even if later works, i.e. Lodato et al. 2009 showed that this time dependency is only reached at later times and it is strongly affected by the stellar internal structure).

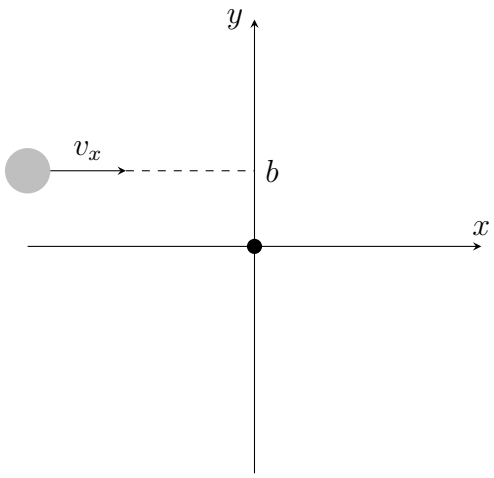

Figure 1.1: *Schematic view of the geometry of the example proposed.*

1.2.2 *The effect of tidal forces on stellar rotation*

It is interesting to notice that even if the incoming star does not posses any initial proper rotation, the tidal forces induce one.

To heuristically derive this fact we can imagine the star as moving on a $x - y$ plane with positive velocity v_x towards the source of gravitational field (a mass $M_{\rm h}$ placed in the origin of the coordinates system) and impact parameter b (figure 1.1).

In the impulse approximation the star will perceive the gravity source upon reaching the y axis, at that moment it will feel an acceleration directed along the negative direction of the y axis of magnitude $GM_{\rm h}/b^2$ for a time $2b/v_x$: this will generate a velocity along y given by

$$v_y = -\frac{GM_{\rm h}}{b^2}\frac{2b}{v_x} = -\frac{2GM_{\rm h}}{bv_x}. \tag{1.8}$$

Since the orbital energy must be conserved during the passage, there will also be a change in the v_x component:

$$\Delta v_x \approx -\frac{v_y^2}{2v_x} = -\frac{2G^2M_{\rm h}^2}{b^2v_x^3}, \tag{1.9}$$

where given the impulse approximation (i.e. $\Delta v_x/v_x \ll 1$) we neglected the square term in Δv_x. One can see that this change in the velocity depends on the closeness with respect to the gravity field source b, so that material that is closest to the hole will experience a stronger reduction in horizontal velocity: the star will thus gain

a spin, prograde with respect to the orbital motion, that we can estimate as

$$\omega \approx \frac{\mathrm{d}\Delta v_x}{\mathrm{d}b} = \frac{4G^2 M_\mathrm{h}^2}{b^3 v_x^3} = \sqrt{\frac{2GM_\star}{R_\star^3}}, \tag{1.10}$$

where we assumed a parabolic orbit for the star with pericenter equal to the tidal radius. We can compare this value with the break-up velocity of the star: defined as the velocity at which the centrifugal force overcome the stellar self-gravity:

$$\omega_\mathrm{b} = \sqrt{\frac{GM_\star}{R_\star^3}}. \tag{1.11}$$

This simple calculation, although approximated, shows therefore that the induced rotation exceed easily the break-up velocity of the star: tidal forces acts inducing a strong rotation in the approaching star.

1.2.3 *The effect of stellar rotation on tidal disruption*

It is possible to analyze the effects of an initial stellar rotation on a TDE using the same approximations of the picture presented above. The main difference will lie in the energy spread calculation: with respect to the previous case of a non-spinning star, now also the kinetic energy will depend on the position of the debris.

Let us assume the stellar rotation to be rigid: the angular velocity, ω, is constant within the star and parametrized by the dimensionless quantity

$$\alpha = \frac{\omega}{\omega_\mathrm{b}}. \tag{1.12}$$

Considering the rotation axis perpendicular to the orbital plane, the kinetic energy of the debris will be

$$E_\mathrm{k} = \frac{1}{2}\left[v_\mathrm{o} + \alpha\omega_\mathrm{b}(r - R_\mathrm{p})\right]^2, \tag{1.13}$$

where

$$v_\mathrm{o} = \sqrt{\frac{2GM_\mathrm{h}}{R_p}} \tag{1.14}$$

is the (parabolic) orbital velocity of the debris. Positive and negative values of α account for prograde and retrograde rotations respectively.

Taking into account the stellar rotation, the energy spread will have therefore an extra term:

$$\Delta E = \frac{\mathrm{d}}{\mathrm{d}r}\bigg|_{R_\mathrm{p}} (E_\mathrm{k} + E_\mathrm{p}) = \frac{GM_\mathrm{h}}{R_\mathrm{p}^2} R_\star (1 + \sqrt{2}\alpha). \tag{1.15}$$

Therefore, positive values of α (prograde rotation) tend to increase the energy spread and make the star more prone to disruption, while negative α result in a reduction of the energy spread, leading to a longer $t_{\rm min}$ and a fainter TDE. Retrograde rotation makes a star more resilient to tidal disruption. In particular, there is a value of stellar rotation, $\alpha = -1/\sqrt{2}$, for which the energy spread is null: a star with such initial rotation will not be disrupted and thus in this case the TDE will be suppressed.

Obviously, given that tidal disruption induces spins comparable to break up, in order to have some effect on the TDE the initial stellar spin needs to be similarly high, close to break up. This is a quite considerable magnitude of stellar rotation: the sun, for example, spins at only 2‰ of its break-up velocity. However the star in Galactic Centers should be spinning at an higher rate due to tidal interactions and spin up (Alexander & Kumar, 2001).

1.3 - **Numerical simulation**

The model presented above predicts that retrograde rotation should suppress a TDE. To better investigate this phenomenon and to find out what would happen to the non-disrupted star we test the analytical predictions against numerical simulations.

The simulation was performed using the Smoothed Particle Hydrodynamic (SPH) code PHANTOM (Price et al., 2017). This choice is due to the fact that in SPH the resolution "follows the mass" and in our simulation the majority of space is empty. The star was modeled as a sphere with a polytropic internal structure (adiabatic index $\gamma = 5/3$). The mass and radius of the star are respectively $1\,M_\odot$ and $1\,R_\odot$, that are also our code units. The velocity unit is $v_0 = \sqrt{GM_\odot/R_\odot} \approx 4.37 \cdot 10^7$ cm/s, the energy unit $E_0 = v_0^2 M_\odot \approx 3.79 \cdot 10^{48}$ erg, the density unit $\rho_0 = M_\odot/R_\odot^3 \approx 5.90$ g/cm^3 and finally the time unit for the system is $t_0 = R_\odot/v_0 \approx 1590$ s.

In all our simulations we used approximately $5 \cdot 10^5$ SPH particles, however we tested the convergence of our results running simulations with $2.5 \cdot 10^5$ and 10^5 particles and finding no appreciable differences.

In the following subsection we will illustrate how we set our stars into rotation in our broad study of the role of stellar rotation on the behavior of TDEs, as this is a quite delicate phase, and then focus on the specific setup we discuss in this Chapter.

1.3.1 *The relaxation process*

The sphere is initially relaxed in the absence of rotation or tidal field of the black hole in order to remove any noise in the initial random displacement of the

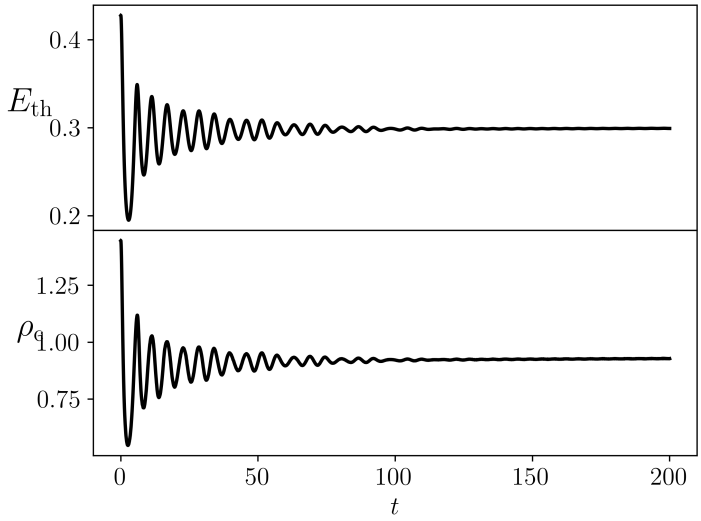

Figure 1.2: *Thermal energy (top panel) and central density (bottom panel) during the relaxation process after the rigid rotation has been imposed as a function of time. After some initial strong oscillations the star reach equilibrium after t=200 (in code units).*

SPH particles. During this phase, we apply a velocity damping, in order to reach equilibrium. We then check that the density profile does follow the expectations of a polytropic sphere (this is similar to what was done in Lodato et al. 2009).

After this first relaxation a rigid rotation is imposed in the inertial frame of the star and then it is relaxed once more until it reaches equilibrium. During this phase, no additional velocity damping is applied, as it would also damp rotation, so relaxation only occurs through internal dissipative processes in SPH, related to artificial viscosity. To check that we reach a new equilibrium, we monitor the oscillations in the star's central density and total thermal energy. Figure 1.2 shows the thermal energy and the central density of the sphere during the relaxation process. They both share a similar behavior: at the beginning strong oscillations get progressively damped until they disappear and the star is considered at equilibrium and the relaxation process is complete.

It is interesting to notice that as we increase the imposed rotation (hereinafter indicated with $\alpha_{\rm in}$), the rotation at the end of the relaxation process ($\alpha_{\rm r}$), does not grow linearly with it. While for $\alpha_{\rm in} \lesssim 0.5$ we have $\alpha_{\rm r} \approx \alpha_{\rm in}$, deviations start appearing for larger initial rotation rates and the final relaxed rate saturates to $\alpha_{\rm r} \approx 0.55$, regardless of the initial amount of rotation imposed. This is due to the fact that as $\alpha_{\rm in}$ grows the star expands, conserving the total angular momentum but decreasing the rotation angular velocity. Figure 1.3 shows $\alpha_{\rm r}$ and the polar

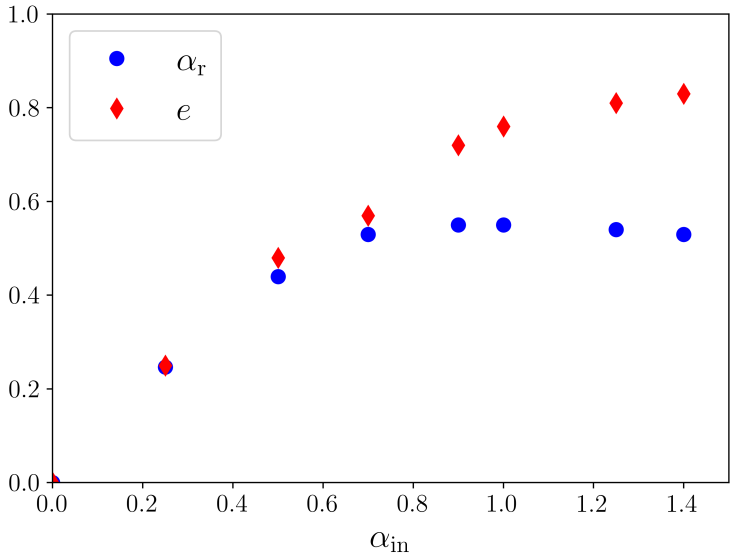

Figure 1.3: *The angular velocity at the end of the relaxation process α_r and polar eccentricity e as functions of the initial angular velocity of the star α_{in}. After a first common linear growths the first tends to saturate while the second keeps increasing.*

eccentricity $e = \sqrt{a^2 + b^2}/a$ (where a and b, the major and minor semi-axis respectively, are calculated setting a cut-off on the density equal to 10^{-2} code units) as functions of α_{in} in our simulations. The parameter α_r is calculated as the average on the angular velocity of the particles within the bulk of the star (that is, the particles rigidly rotating around the spin axis). It is notable that after an initial common linear growths, α_r saturates around a value of $\alpha_r \approx 0.55$, while the polar eccentricity keeps growing although at a lower rate: this is due to the fact that the star flattens as α_{in} increase.

Given the presence of the saturation, stars with the same α_r could come from different α_{in} and hence they have different internal structure and a different total angular momentum.

This behavior follows the analytical predictions on the polar eccentricity and angular velocity for rotating spheroids, in particular the McLaurin series (Chandrasekhar, 1987). Figure 1.4 shows the normalized squared angular velocity of our simulated rotating spheres as a function of the polar eccentricity (green triangles), superimposed to the McLaurin analytical series (solid black line). The agreement does not appear to be good, however, considering that the McLaurin series is computed for uniform density sphere while we deal with a polytropic internal structure and that our data points follow the general trend predicted by the model we can consider ourselves satisfied.

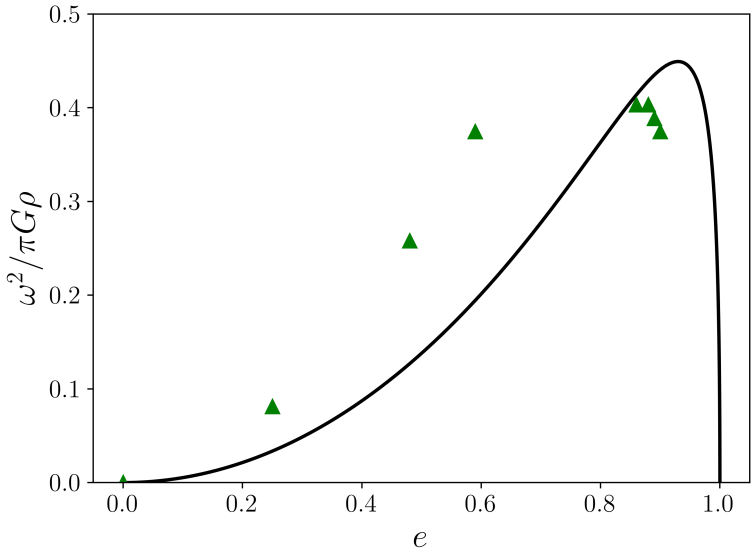

Figure 1.4: *Normalized squared angular velocity as a function of the polar eccentricity of our simulation (colored triangles) compared with the McLaurin analytical series (solid black line).*

1.3.2 *Numerical setup*

For our simulation the sphere is relaxed with a value of $\alpha_{\rm in}$ equal to 1 and a subsequent $\alpha_{\rm r} = 0.55$.

Figure 1.5 shows the density (top panel) and azimuthal velocity (bottom panel) of our sphere as functions of the distance from the rotation axis before (left panel) and after (right panel) the relaxation process. It is interesting to note that after the relaxation the bulk of the star keeps rotating rigidly, although at a reduced rate (see above). Also, a tail of particles with approximately Keplerian velocity profile is formed, with a negligible total mass.

The relaxed sphere is then injected into a parabolic orbit around a black hole of $10^6 M_\odot$ (modeled as a Keplerian potential) from a distance equal to $3R_{\rm t}$, with penetration factor $\beta = 1$. Values of β greater than 1 mean that the star undergoes a deep plunge in the black hole potential well, while values smaller than 1 mean a far away passage. A passage with $\beta = 1$ guarantees a complete stellar disruption, for $\beta < 1$ instead one only gets partial disruption or the stripping of stellar material (Guillochon & Ramirez-Ruiz, 2013). The star is set to have a retrograde rotation with spin axis perpendicular to the orbital plane.

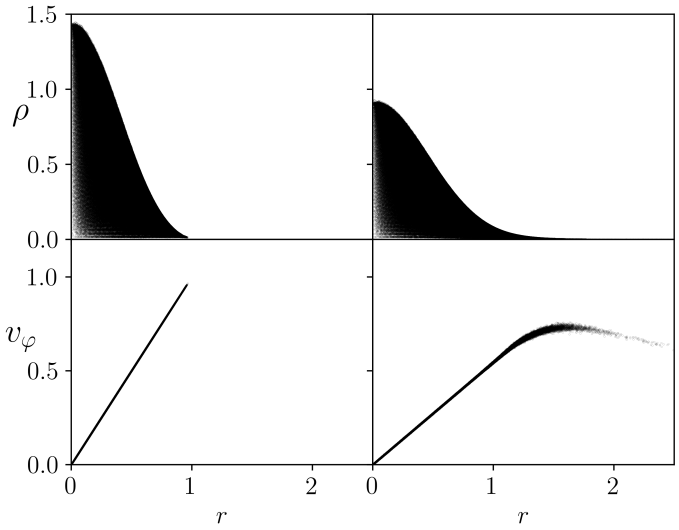

Figure 1.5: *Comparison between the stellar properties before (left side) and after (right side) the relaxation process. The top panels show the density and the bottom ones the azimuthal velocity as functions of the distance from the rotation axis.*

1.4 - **Results**

Our simulation shows that, even though the star formally reaches its tidal radius, it does not get destroyed: as predicted by our simple analytical model, an initial retrograde stellar rotation can indeed suppress the tidal disruption of a star. Nevertheless, the black hole tides are able to rip off some material from the star, however these debris do not accrete onto the black hole, indeed, at the end of the simulation, the mass loss suffered by the star is less then the 0.5% of its initial mass: their fate is to be reaccreted onto the survival stellar core. In doing so they form an accretion disc with a Keplerian velocity profile.

Figure 1.6 and 1.7 show four snapshots of our simulation taken at the time $t = 0$, $t = 20$, $t = 40$ and $t = 150$ in our code units. The star is seen from above and from the side respectively and the rendering shows the projected density in code units. It is possible to see how the stellar material gets ripped off but eventually it falls back onto the stellar core as described above. In the last snapshot, taken at the end of our simulation, it is possible to recognize a disc.

Figure 1.8 shows the velocity profile of the stellar remnant at the end of the simulation. The logarithmic plot shows the azimuthal velocity as a function of the distance from the rotation axis in the stellar center of mass frame. The plot shows how the stellar core is in rigid rotation, while the particles surrounding the core have a Keplerian velocity profile (indicated by the solid line).

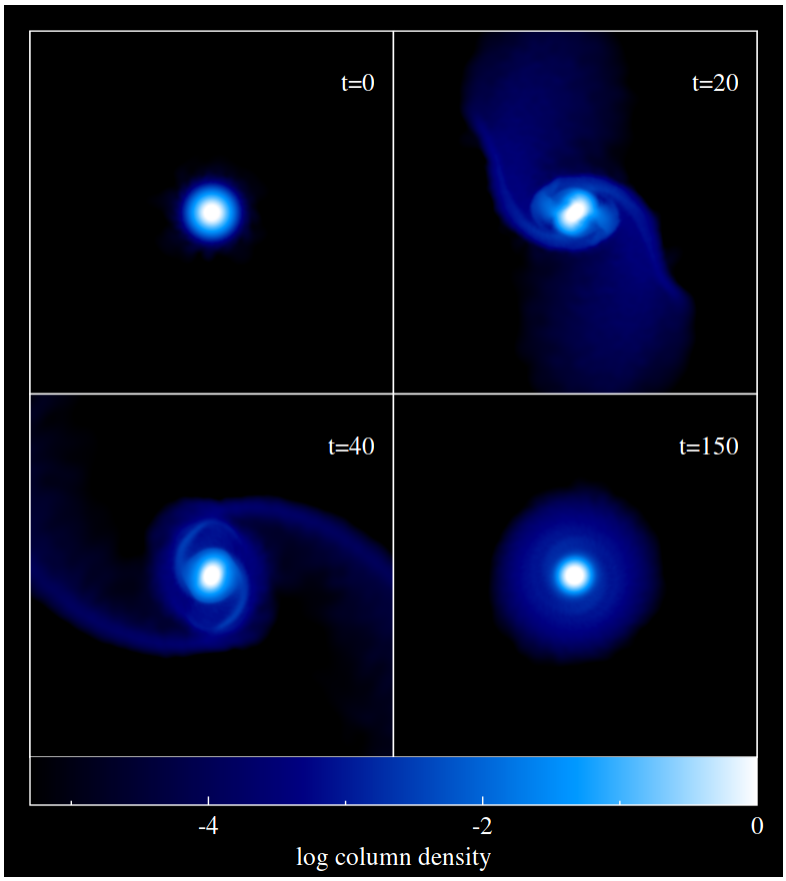

Figure 1.6: *Projected density of the star, each panel shows a snapshot taken at a different time, as indicated in the figure in code units. In physical units the snapshots refer roughly to $t = 0$, 9 hours, 18 hours and 3 days after the pericenter passage, respectively. The star is seen face-on.*

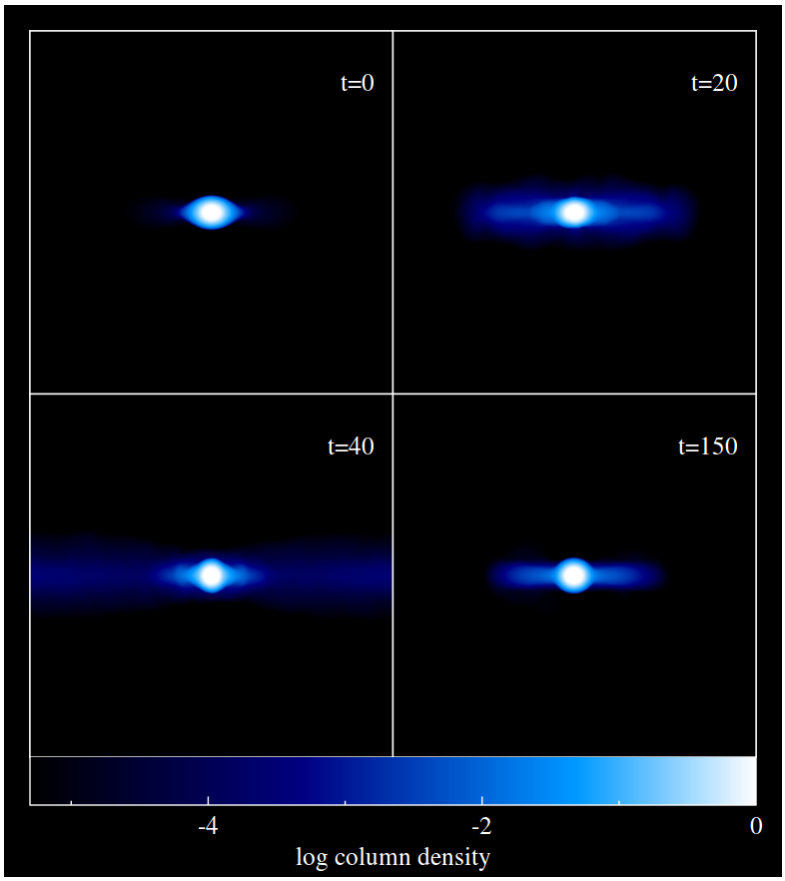

Figure 1.7: *Projected density of the star, each panel shows a snapshot taken at a different time, as indicated in the figure in code units. In physical units the snapshots refer roughly to $t = 0$, 9 hours, 18 hours and 3 days after the pericenter passage, respectively. The star is seen edge-on.*

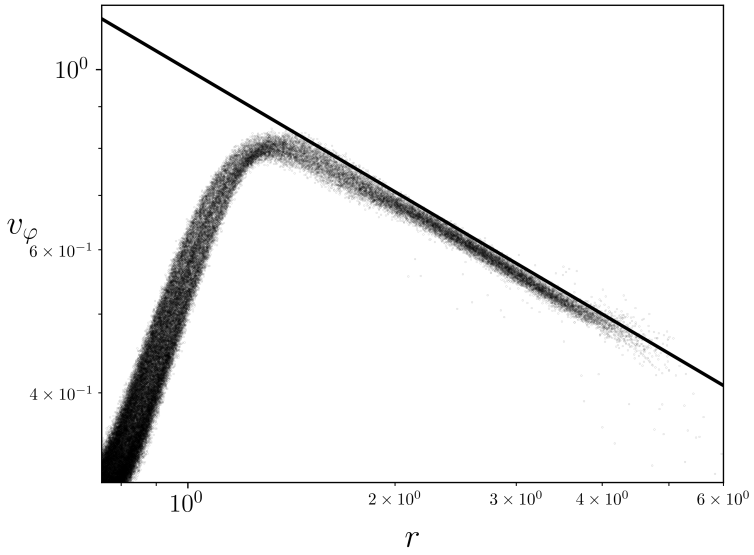

Figure 1.8: *Velocity profile of the disc: azimuthal velocity as a function of the distance from the stellar core. The solid line is the $r^{1/2}$ behavior expected for a Keplerian disc.*

1.4.1 *Observational prospects*

At the end of our simulation we thus produce a thick accretion disc around a stellar core. The disc inner and outer radius (estimated from the velocity profile considering part of the disc only the particles with Keplerian velocity) are respectively $R_\mathrm{i} \approx 1.36\, R_\odot$ and $R_\mathrm{o} \approx 4.69\, R_\odot$, with a thickness of $H \approx 1.46\, R_\odot$. The mass of the disc amounts to $M_\mathrm{d} = 3.18 \cdot 10^{-2}\, M_\odot$.

To infer the evolution of the disc we can compute the viscous time at the disc outer edge

$$t_\nu = \frac{R_\mathrm{o}^2}{\alpha_\mathrm{SS} H^2 \Omega} \simeq 1.67 \cdot 10^6 \left(\frac{0.1}{\alpha_\mathrm{SS}}\right) \mathrm{sec} \approx 0.05 \left(\frac{0.1}{\alpha_\mathrm{SS}}\right) \mathrm{yr}, \tag{1.16}$$

where Ω is the angular velocity at the outer edge of the disc, given by

$$\Omega = \sqrt{\frac{G M_\mathrm{s}}{R_\mathrm{o}^3}} \simeq 6.17 \cdot 10^{-5}\, \mathrm{sec}^{-1}. \tag{1.17}$$

We also assume that the disc evolves viscously, with a Shakura & Sunyaev (1973) parameter α_SS. A rough estimate for the accretion rate can then be given as

$$\dot{M}_\mathrm{s} \approx \frac{M_\mathrm{d}}{t_\nu} \approx 0.63 \left(\frac{0.1}{\alpha_\mathrm{SS}}\right)^{-1} M_\odot/\mathrm{yr}. \tag{1.18}$$

Given these quantities the luminosity of this kind of event should amount to

$$L \approx \frac{G M_{\rm s} \dot{M}_{\rm s}}{2 R_\odot} = 2.67 \cdot 10^{40}\,\text{erg/s} \left(\frac{\alpha_{\rm SS}}{0.1}\right) \approx 200\, L_{\rm Edd} \left(\frac{\alpha_{\rm SS}}{0.1}\right), \tag{1.19}$$

where the Eddington luminosity $L_{\rm Edd} \approx 1.26 \cdot 10^{38}$ erg/s is referred to the star. The Shakura & Sunyaev (1973) viscosity parameter, $\alpha_{\rm SS}$, in such a newly formed disc is not easy to estimate, given that we expect the magnetic field threading the disc to be weak and the magneto-rotational instability not to be effective (Bugli et al., 2018; Nealon et al., 2018). We have scaled it to $\alpha_{\rm SS} = 0.1$ in the estimates above, but even if it was lower by two orders of magnitude, we should still expect an accretion event above Eddington for the star.

At those luminosities, the expected temperature at the disc inner edge is $\approx 3.5 \cdot 10^5$ K, and thus, we expect such a hyper-accreting star to have significant emission in the X-ray band (young stars accreting at rates up to six order of magnitude smaller then our case have considerable emission in this band Feigelson et al. 2007), even though a smaller value of $\alpha_{\rm SS}$ could move it towards the UV-optical band.

The characteristics described above make our event compatible with the one described by Churazov et al. (2017): a bright X-ray flare with a duration no longer that a few years.

1.4.2 *Further stellar evolution*

At the end of our simulation the energy of the center of mass of the star is negative. This means that during the pericenter passage, the star gets captured by the black hole.

From the energy of the center of mass of the star we calculated the orbital period of the newly bound star to be roughly one hundred years and its apocenter to be placed at ≈ 4000 au.

Furthermore from the z component of the vorticity we can infer that the tidal forces are able, during the pericenter passage, to completely reverse the spin of the star.

Figure 1.9 shows the z component of the vorticity at different times during the simulation. It is possible to notice how at the beginning the z component is negative, i.e. the rotation is retrograde, while at the end it is positive: the rotation of the star is therefore prograde with the orbital motion with. Furthermore the rotation of the stellar core is rigid and with the remarkable magnitude of $\alpha \approx 0.3$.

Taking into account that the star, after the passage, gets bound to the black hole and that its spin axis gets completely reversed, we can predict that roughly a century after the "failed" TDE, the star will approach again the black hole, this

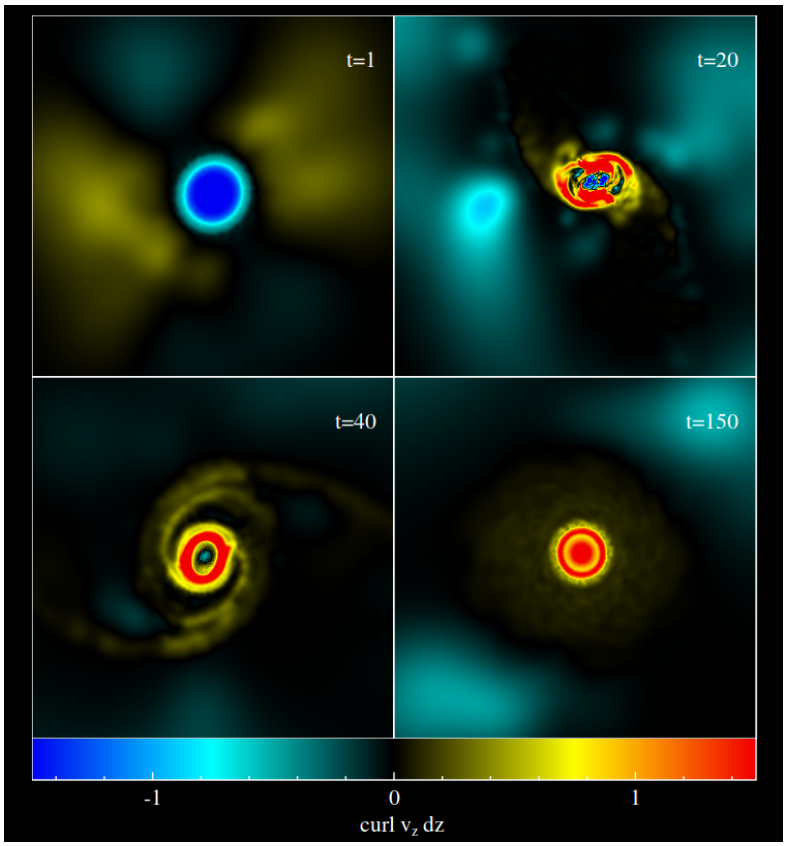

Figure 1.9: *Each panel shows the z component of the velocity at different times, as indicated in the figure in code units. In physical units the snapshots refer roughly to $t = 0$, 9 hours, 18 hours and 3 days after the pericenter passage, respectively. The star is seen face-on.*

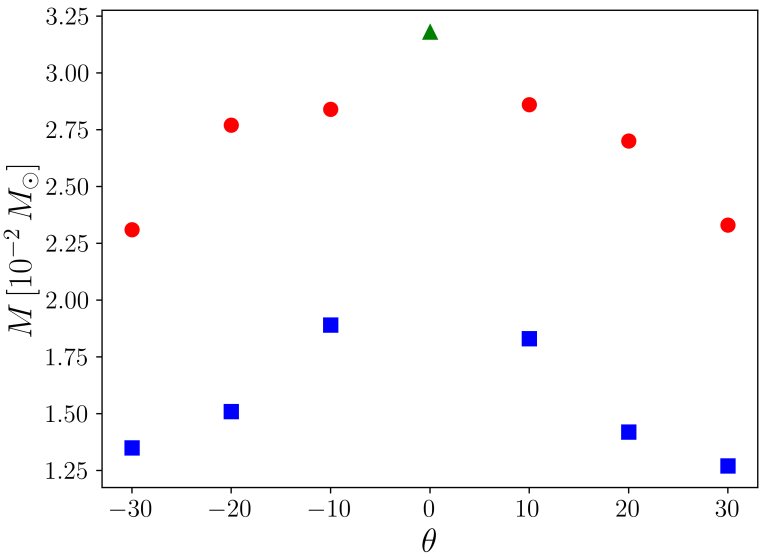

Figure 1.10: *The mass of the disc at the end of our simulations, the green triangle is the completely retrograde case while the blue squares and red circles indicates tilting around y and x axis respectively.*

time however with a prograde and considerable spin, thus originating an enhanced TDE.

1.5 - **Dependence on the orientation of the stellar spin**

The simulation described in Section 1.4 is referred to the particular case in which the stellar spin axis is exactly anti-parallel to the orbital angular momentum.

As shown by Golightly et al. (2019), the dependence of the features of a tidal disruption event on the orientation of the spin axis can be strong, and we therefore ran a few simulations with the stellar spin axis slightly misaligned with respect to the configuration considered until now.

As expected, we find that the formation of the disc of debris is inhibited as the deviation from the totally retrograde rotation regime grows. Although a disc forms, it is less massive than the perpendicular case, because more debris are ejected rather than re-accreted.

Figure 1.10 shows the mass of the disc as a function of the tilt angle with respect to the retrograde regime. The green triangle represents the mass of the disc in the retrograde case, the blue squares a tilting along the y axis while the red circles a tilting around the x axis.

While the behaviour of the system is roughly symmetric to whether the tilting

is right-handed (positive values of the angle) or left-handed (negative values), a tilting around y clearly suppress the disc formation more aggressively than one around x. However even for a significant tilting of 30° a disc still forms and its mass has dropped only by a factor ≈ 2.5 for the y-axis tilting and ≈ 1.3 if the tilting is performed around the x-axis.

1.6 - **Conclusions**

In this Chapter we discuss the possibility of a "failed" tidal disruption event at the origin of a one hundred years old X-ray flare from SGR A*.

Through analytical calculation we find that a sufficiently strong stellar retrograde rotation could suppress its disruption during a black hole pericenter passage. We then performed a numerical simulation with the SPH code PHANTOM in order to validate our predictions.

We discovered that even if the star does not get destroyed by the black hole tidal forces and thus no debris get accreted by the hole, significant electromagnetic emission can arise due to the formation of an accretion disc around the stellar core itself. This disc is made out of the material partially ripped off the star during the black hole flyby.

Through considerations about the size, mass and evolution of this newly born disc we can infer that this event should produce a luminosity of $\approx 3 \cdot 10^{40}$ erg/s on a period of few months, peaked in the X-ray band. This makes this event compatible with the one described by Churazov et al. (2017). Unfortunately, given the predicted luminosity, this kind of events will be observable only in our Galaxy.

Furthermore, as the star orbits the black hole, it gets captured by it and is placed on an highly eccentric elliptical orbit around the hole, with an orbital period of roughly one hundred years. This is coupled to a complete reversal of the stellar spin axis: where at the beginning the star is characterized by a retrograde rotation, after the pericenter passage its rotation is prograde and still fairly intense ($\alpha \approx 0.3$).

These two facts bring to the conclusion that a century after the failed TDE there will be a regular (or possibly even an enhanced) one as the incoming star is, this second time, characterized by a rotation that is prograde with respect to the orbital motion.

In this scenario the survived stellar core, would currently be on an highly eccentric orbit around SGR A* and would eventually come back to the hole to be disrupted in a typical tidal disruption event.

2 Fragmentation of debris streams from TDEs

A tidal disruption event (TDE) occurs when a star passes too close to a supermassive black hole and gets torn apart by its gravitational tidal field. After the disruption, the stellar debris form an expanding gaseous stream. The morphology and evolution of this stream is particularly interesting as it ultimately determines the observational properties of the event itself. In this work we perform 3D hydrodynamical simulations of the TDE of a star modelled as a polytropic sphere of index $\gamma = 5/3$, and study the gravitational stability of the resulting gas stream. We provide an analytical solution for the evolution of the stream in the bound, unbound and marginally bound case, that allows us to describe the stream properties and analyse the time-scales of the physical processes involved, applying a formalism developed in star formation context. Our results are that, when fragmentation occurs, it is fueled by the failure of pressure in supporting the gas against its self-gravity. We also show that a stability criterion that includes also the stream gas pressure proves to be far more accurate than one that only considers the black hole tidal forces, giving analytical predictions of the time evolution of the various forces associated to the stream. Our results point out that fragmentation occurs on timescales longer compared with the observational windows of these events and is thus not expected to give rise to significant observational features.

2.1 - Introduction

The observable properties of a TDE are closely connected to the stream of debris that forms after the stellar disruption. In particular, the self-gravity of the stream can become dominant in the transverse direction (Kochanek, 1994) and it is therefore possible to encounter a gravitational instability which my lead to fragmentation. Initially studied in the pioneer works of Coughlin & Nixon (2015), an instability criterion for a TDE debris stream can be obtained by defining a *critical density* for the SMBH, $\rho_{\rm h} \sim M_{\rm h}/r^3$, where r is the distance of a debris fluid element from the SMBH. This yields an instability condition in the form $\rho > \rho_{\rm h}$, picturing a scenario where the critical density falls at a rate that is steeper than the debris

density with respect to radial distance from the SMBH. The physical meaning of this is that the rate at which the material is torn apart is slower than the rate at which it aggregates. In this condition the debris stream is subject to fragmentation and is therefore considered to be *gravitationally unstable*.

If the debris is described by a polytropic model (Chandrasekhar, 1939), the pressure p is $p = k\rho^{\gamma}$, where k is a proportionality constant and γ is called the polytropic index. Numerical simulations confirmed that the evolution of the debris stream and its density depend on γ (Coughlin & Nixon, 2015).

Furthermore, Coughlin et al. (2016a,b) showed that the stability of the streams depends on the polytropic index, and in particular revealed how, for $\gamma \gtrsim 5/3$, the stream is susceptible to fragmentation. The newly formed clumps of material can strongly affect the light curve of the event, on account of the fact that the debris is not accreted "continuously" but rather in almost discrete blocks.

It is not clear whether a star with critical index $\gamma = 5/3$ should be gravitationally stable or should fragment. The conclusion from Coughlin et al. (2016b) is that the star should be unstable for fragmentation, though only at later times: this is due to the fact that in this peculiar case the over-densities grow as a power-law rather than exponentially as in more compact ($\gamma > 5/3$) cases. In this Chapter we wish to verify this result and better understand this pivotal case's behavior along with the stability criterion. In order to do so we will perform numerical simulations and analytical calculation, often considering the debris stream as in free-fall onto the black hole. This approximation, already employed by Coughlin & Nixon (2019) proved to be extremely effective in describing the behaviour of the marginally bound part of the stream.

The actual lightcurve of TDEs will depend on several other physical effects. The internal structure of the star may modify the long term evolution of the stream (Lodato et al., 2009; Guillochon & Ramirez-Ruiz, 2013; Law-Smith et al., 2019; Ryu et al., 2020). The possible influence of a secondary black hole (Liu et al., 2009; Coughlin et al., 2017; Coughlin & Armitage, 2018; Vigneron et al., 2018; Coughlin et al., 2019) will affect the orbital evolution of the debris. Also, the incoming debris will be affected by relativistic precession (Hayasaki et al., 2013; Bonnerot et al., 2016; Liptai et al., 2019; Gafton & Rosswog, 2019) and the emerging emission will certainly depend on the specific heating and cooling process of the accretion flow. Here, we concentrate specifically on the dynamics of the stream in the simplest configuration of a single black hole. The internal structure of the star, while modifying the long-term evolution is not expected to alter significantly the stability of the stream.

The Chapter is organized as follows: in Section 2.2 we will describe the numerical setup of the simulations we performed in order to test the $\gamma = 5/3$ case: a "standard" simulation without stellar rotation and a case with an initial stellar rotation. Our initial goal was to widen our understanding of the problem consid-

ering also the effect of rotation; in Section 2.3 we will show the results of our simulations; in Section 2.4 we will discuss the parallelism between the debris streams that form after a TDE and the gas filaments found in star forming regions and we will derive interesting analytical results using the formalism developed in that context; finally in Section 2.5 we will draw our conclusions.

2.2 - **Numerical simulations**

In order to better understand and possibly clarify the nature of the fragmentation we performed numerical simulations. We suppose that the stream follows a polytropic equation of state $p = k\rho^\gamma$, where we recall that p is the pressure of the gas, ρ its density, k is the polytropic constant and γ the polytropic index, equal in our case to $5/3$. The simulations are performed using a polytropic sphere with adiabatic index $\gamma = 5/3$ to model our to-be-disrupted star. This value of polytropic index is also particularly interesting as it is the most common choice in all of the simulation in literature since Nolthenius & Katz (1982).

The simulations employ a 3D Smoothed Particle Hydrodynamic (SPH) code, PHANTOM (Price et al., 2017). SPH codes are particularly suitable for simulating TDEs as the majority of the space covered by our simulations is empty and these codes have the key property of linking the resolution of the simulation to the mass distribution.

As in the simulations presented in Chapter 1 the mass of the star and its radius are set to be $1\,M_\odot$ and $1\,R_\odot$ and are also chosen as our code units. Likewise the density unit is $\rho_0 = M_\odot/R_\odot^3 \approx 5.09$ g/cm^3 and the time unit is $t_0 = \sqrt{R_\odot^3/GM_\odot} \approx 1590$ s, although more often we will adopt as time unit the minimum return time $t_{\rm min}$ which in our simulations amounts to ≈ 41 days.

In order to decide the optimal number of particles to use in our simulations we performed a convergence test. Convergence is reached at $\approx 1.5 \times 10^6$ SPH particles. This number is higher than the one usually used to simulate TDEs (Evans & Kochanek, 1989; Ayal et al., 2000; Bogdanović et al., 2004), as we need to resolve the instability of the stream rather than its bulk motion.

2.2.1 *Numerical setup*

The numerical setup of our simulation is prepared in the same way described in Section 1.3: the polytropic sphere is initially relaxed without the black hole gravitational potential and a velocity damping. In the case of a rotating star, after this first phase a rigid rotation is imposed and the sphere is relaxed once more, this time without the velocity damping. As we have seen in the previous Chapter the value of stellar rotation, parametrized once more with the adimensional $\alpha = \omega/\omega_{\rm b}$

varies during the relaxation process (Sacchi & Lodato, 2019), however, the value of α in our simulation is relatively small: $\alpha = 0.2$ and for this small value of stellar rotation the observed reduction during the second relaxation phase is negligible.

Once the star is relaxed, whether rotating or not, it is injected into a parabolic orbit around a $10^6\ M_\odot$ black hole, which is modelled as a Keplerian potential from a distance of 3 tidal radii.

After the star gets past the pericenter, it is disrupted. When it is sufficiently far from the source of the Keplerian potential, the latter is replaced with a sink particle of mass $10^6\ M_\odot$ and a relatively large accretion radius of 5 tidal radii. This means that every SPH particle that gets closer than 5 tidal radii from the black hole is considered to be accreted and removed from the simulation. This of course does not allow us to observe the physics of stream-stream shocks, circularization and accretion, however this choice is due to the fact that we are focusing our interest on the stream evolution properties.

2.3 - **Results**

Here we illustrate the results of our simulations. We performed two sets of simulations, the first with a non-rotating star ($\alpha = 0$) and a second set including the rotation of the star ($\alpha \neq 0$ and in our particular case $\alpha = 0.2$). To better highlight the major steps we divided the Section as follows: we will first discuss how we determined the presence or absence of fragmentation in our simulation, then we will discuss the mechanism that generates it through time scale comparison and lastly we will show what happens if one adds an initial stellar rotation to the system.

2.3.1 *Fragmentation and convergence*

The first crucial result obtained through our simulation is that the stream of gas generated by the tidal disruption of a non-rotating star modelled as a polytropic sphere with adiabatic index $\gamma = 5/3$ is affected by gravitational instabilities that bring it to fragment into smaller almost spherical blobs, as already shown by Coughlin & Nixon (2015).

The presence of fragmentation is assessed via visual analysis of the stream appearance and through the analysis of the mean density and the density fluctuations, evaluated as the standard deviation of the mean density.

Figure 2.1 shows how initially both the mean value of the density (solid black line) and the fluctuations (dashed black line) fall as a power-law with power index $n \approx -1.67$. After almost $30\ t_{\text{min}}$ the density fluctuations reach their minimum and start growing, soon overcoming the mean density of the stream. The turning point of the fluctuations is interpreted, in analogy with Cosmology (Peebles, 1980), as

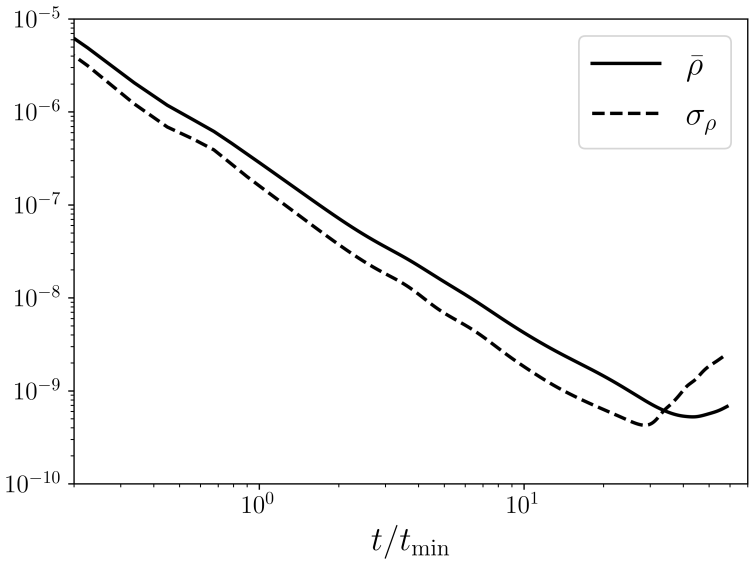

Figure 2.1: *The solid line represent the mean density of the stream while the dashed one the density fluctuations, as functions of time, normalised to the minimum return time.*

the moment where fragmentation starts.

In order to confirm this technique we analyse also the projected density of the stream taking snapshots or our simulation. Figure 2.2 shows a section of the stream at four different moments: $t = 10, 25, 35$ and $55\ t_{\rm min}$ (that is as 13 months, almost 3 years, 4 years and 6 years after the stellar disruption). These moments corresponds to an instant way before the fragmentation, right before, right after and far after the fragmentation occurred. From these snapshots it is clear that the fragmentation occurs indeed when the density fluctuations reach the turning point.

The search for a criterion able to identify effectively the time at which the stream fragments is of particular interest as the one presented in the Introduction, suggested by Coughlin et al. (2016b), does not give not an overly accurate estimate. To be more precise, Figure 2.3 shows the mass distribution $\mathrm{d}M/\mathrm{d}(\rho r^3)$ as a function of ρr^3 for two stellar structures: the so far studied $\gamma = 5/3$ and a more compact case $\gamma = 2$, more susceptible to fragmentation. The distribution is shown at two times: when the stream is still far before the fragmentation point ($t = 0.3\ t_{\rm frag}$, dashed line) and far after ($t = 2\ t_{\rm frag}$, solid line), where $t_{\rm frag}$ is the time at which fragmentation occurs. Figure 2.3 shows how the criterion based on the tides, ρr^3 be larger than the black hole mass $M_{\rm h} = 10^6\ M_\odot$ (indicated by the vertical dotted line in the figure), is satisfied by almost all of the stream, except for a small fraction of it ($\lesssim 10\%$) already at the earliest time. The fact that the most compact scenario shows a distinct plateau at high densities after disruption might imply that a sharper

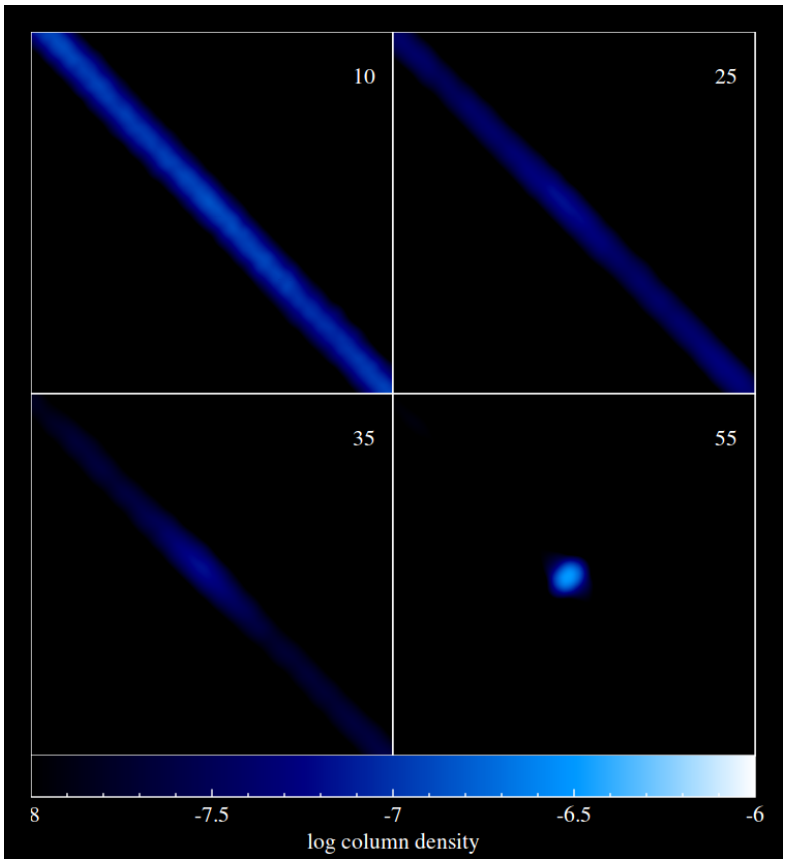

Figure 2.2: *Projected density of the stream. Each panel shows the simulation taken at different times: at* $t = 10$, 25, 35 *and* $55\ t_{\rm min}$ *from top left to bottom right.*

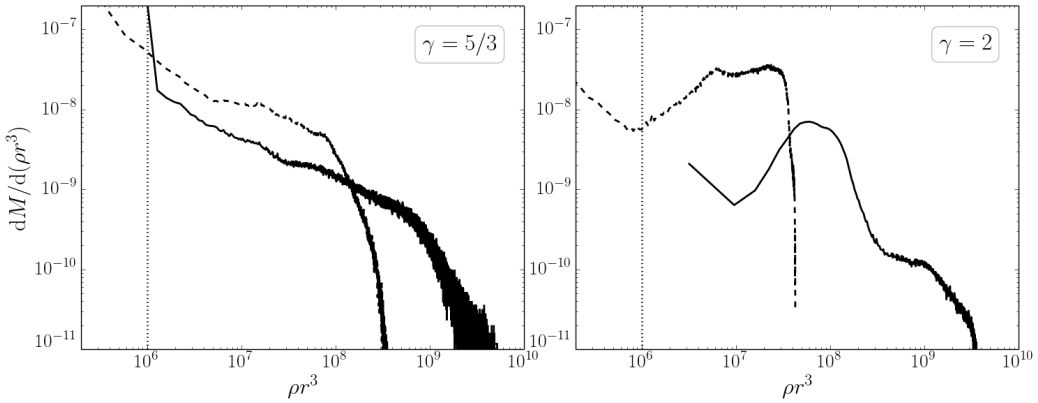

Figure 2.3: *A representation of the tidal criterion for two different stellar structures (the primary case for this work alongside a more compact one with $\gamma = 2$) showing the $\mathrm{d}M/\mathrm{d}(\rho r^3)$ as a function of ρr^3 at different times in the simulation, such as far before the fragmentation point ($t = 0.3\ t_{\mathrm{frag}}$, dashed line) and far after ($t = 2\ t_{\mathrm{frag}}$, solid line). In order for the tidal criterion to be satisfied ρr^3 must be greater then M_{h}, indicated by the vertical dashed line.*

criterion should have its critical point further up in the ρr^3 ladder, instead of setting it at the black hole mass.

As suggested by Coughlin et al. (2016b), based on simulations described in Coughlin & Nixon (2015) and Coughlin et al. (2016a), the noise due to the numerical methods affects the time at which fragmentation occurs. The aforementioned convergence test has been performed in order to prove that the fragmentation is indeed physical and not only a result of numerical features of the code. The convergence has been considered satisfied when increasing the number of SPH particles employed in the simulation, the time at which fragmentation occurs would not increase appreciably.

Figure 2.4 shows the behaviour of t_{frag} as a function of the number of SPH particle of our simulations. When the simulation is performed using a number of particles smaller than $\approx 10^6$, t_{frag} is strongly dependent on the resolution of the simulation, while above one million SPH particles it can be considered roughly constant. Note that the time of fragmentation occurs when the luminosity has already dropped by $\sim (30)^{-5/3} \sim 3 \times 10^{-3}$ from the peak. We consider our choice of using, as mentioned in the previous Section (1.5×10^6 particles), satisfactory.

2.3.2 *Time scales*

We now consider the mechanisms responsible for the fragmentation. We compare the various contributions of the forces playing an active role in our picture by

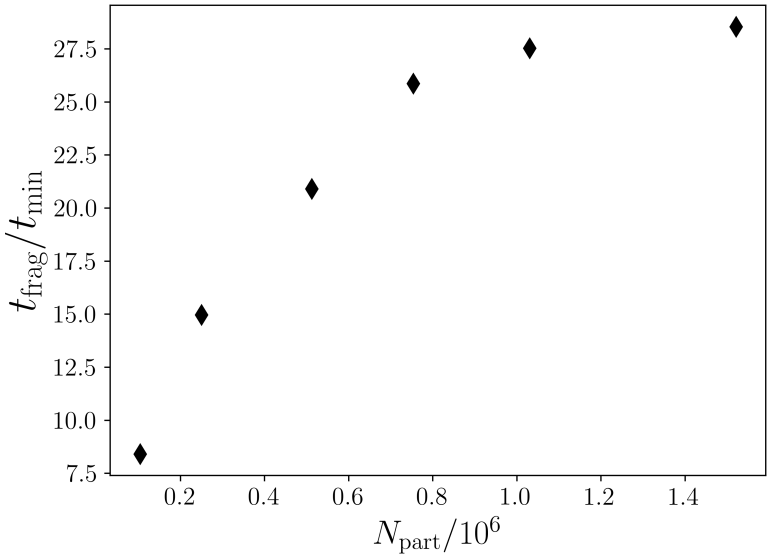

Figure 2.4: *The figure shows the time at which the fragmentation occurs as a function of the number of SPH particles used in the simulation.*

comparing their characteristic time scales.

Representing the stream as a cylindrical fluid is a good assumption for the dynamics of these events, as also pointed out by Coughlin & Nixon 2019. In their work, the authors wrote the Lagrangian describing the motion of the core of the stream considering the effects of the black hole and the core mass gravitational forces, focusing on the fallback rate temporal behaviour and the bound core fate.

In this work, we are interested in studying the *fluid* behaviour of the debris stream, its equilibrium state and its (eventual) fragmentation. This allow us to derive the temporal evolution of the stream quantities using simple physical considerations, introducing time scales related to the main forces at play and discussing their evolution with time. Four are the forces that are actively involved in determining the dynamics of a fluid stream. Apart from the self-gravity of the stream and the tidal effects of the black hole, the internal forces of the gas (i.e. its pressure) and the background stretching of the gas are also at play. Indeed, the stream is affected by a stretching in the volume along the radial direction of the black hole, due to the differential acceleration of the particles composing the stream. This phenomenon is very important because it affects *all* the quantities, introducing a time-dependency that becomes important as time passes by.

Each of these forces corresponds to a typical time scale: the stream self-gravity is linked to the free-fall time $t_{\rm ff}$, the tidal force generated by the black hole corresponds to a typical dynamical time $t_{\rm d}$, the gas pressure of the stream is

associated to the sound crossing time $t_{\rm sc}$ and finally we have a stretching time scale $t_{\rm s}$. As pointed out, we are interested in the debris stream: in the following analysis all these quantities are always referred to and computed for the part of the stream with positive energy.

The first force we consider is the stream self-gravity. This force will obviously favor the fragmentation and gravitational collapse and thus the fragmentation of the debris. The free-fall time is given by (Jeans, 1902):

$$t_{\rm ff} = \frac{1}{\sqrt{2\pi G\rho}}, \tag{2.1}$$

where ρ is the density of the stream and the 2π factor accounts for the cylindrical geometry we are working with.

The tidal forces of the black hole tend to prevent any gravitational collapse. The dynamical time is computed as

$$t_{\rm d} \simeq \frac{1}{\sqrt{G\rho_{\rm h}}}, \tag{2.2}$$

where $\rho_{\rm h} = 3M_{\rm h}/4\pi r^3$ is the "density" of the black hole over a sphere of radius r.

Pressure tends to stabilize the stream, the relative thermal time is just the sound crossing time across the transverse direction

$$t_{\rm p} = \frac{H}{c_{\rm s}}, \tag{2.3}$$

where H is the transverse size of the stream and $c_{\rm s}$ is the sound speed of the gas. The sound speed is calculated from the density, knowing the polytropic equation of state that describes the gas :

$$c_{\rm s} = \sqrt{\left.\frac{\partial p}{\partial \rho}\right|_s} = \sqrt{k\gamma\rho^{\gamma-1}}, \tag{2.4}$$

The stream width H is obtained by averaging the distance of the particles composing the stream, considered again as a cylinder, from its axis: operatively we "sliced" the stream along its length and for each slice we computed the mean distance of the particles within the slice from the cylinder axis, finally we mediated all the radii obtained along the stream. Figure 2.5 shows H as a function of the distance from the black hole normalized to the tidal radius of the original star (solid black line). The dashed black line shows the $r^{1/2}$ behaviour found by Coughlin et al. (2016b) in disagreement with the $r^{1/4}$ prediction of Kochanek (1994).

The last time scale is associated to the stream stretching along its axis. This apparent force is due to the fact that right after the stellar disruption each gas

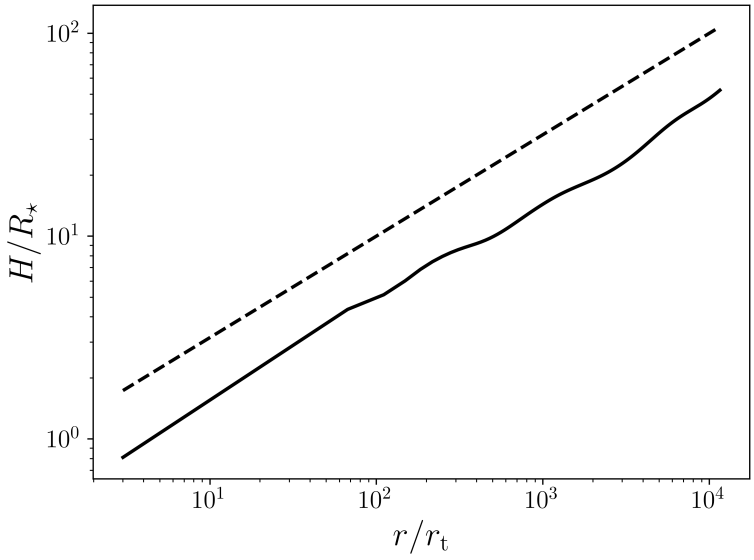

Figure 2.5: *The solid black line shows the stream width as a function of the distance from the black hole normalized to the tidal radius. The dashed black line is the $r^{1/2}$ behaviour.*

particle lies on a different orbit determined by its energy. The spread in energy of the debris is given by the change of the black hole gravitational potential across the star at the time of disruption, that is at the first pericenter passage, in the impulse approximation (Lacy et al., 1982; Rees, 1988). We suppose that the length l of the stream changes with time according to the prescription $l = l_0 a(t)$, where l_0 is the length of the stream at the initial time and $a(t)$ represents a dimensionless parameter of the stretching. This stretching introduces a proper timescale, defined in analogy with the Hubble time in Cosmology (Peebles, 1980) as

$$t_\mathrm{s} = \frac{a}{\dot{a}}, \tag{2.5}$$

where the dot indicates the time derivative. The idea to consider the expansion and the contraction of the fluid volume in analogy with Cosmology using dimensionless parameters and an appropriate coordinate system has been already used to study the Solar wind fluctuations (Grappin & Velli, 1996; Landi et al., 2014; Del Zanna et al., 2015) as well as the collapse of pre-stellar cores (Toci et al., 2018).

Figure 2.6 shows the behaviour of the four described time scales as a function of time. The solid black line represents the tidal time, the dashed one the free-fall time, the dotted line is the thermal time and dash-dotted one is the stretching time. They are all normalized to the minimum return time (the time at which the first of the stellar debris comes back to its orbital pericenter, in our case ≈ 41 days) while the time on the x-axis is normalized to the fragmentation time $t_\mathrm{frag} \approx 30\, t_\mathrm{min}$. The

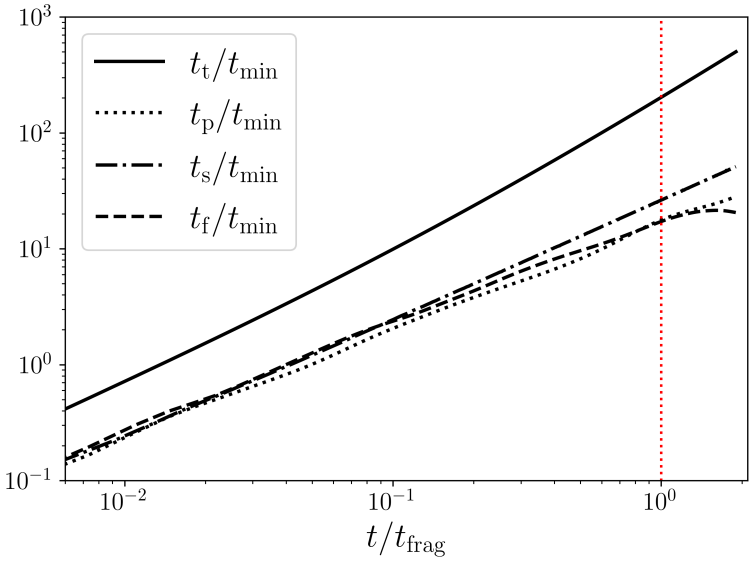

Figure 2.6: *The figure shows the four described time scales: tidal (solid black line), thermal (dotted), stretching (dashed) and free-fall (dash-dotted). All the time scales are normalized to the minimum return time ($t_{\rm min} \approx 41$ days), while the time on x-axis is normalized to the time at which fragmentation occurs $t_{\rm frag} \approx 30\ t_{\rm min}$.*

vertical dotted red line has been drawn to facilitate the comparison of the time scales at the fragmentation time.

The first consideration one can draw from figure 2.6 is that all the time scales have comparable magnitudes (within a factor 1.1), crossing several times during the stream evolution. The only exception is the tidal time that is a factor $2.5 - 12$ longer than the others, although at the beginning of the simulation, this time scale should have been the smallest one in order for the star to be tidally disrupted. This immediately shows that tidal forces are not responsible for fragmentation, where it happens.

Apart from the tidal time scale, all of the other time scales share a very similar evolution. The thermal time is the smallest one along almost the entirety, hence pressure is the most relevant force of the stream evolution, and it prevents its fragmentation. The time scales that disentangles from the others is the stretching time, that accelerates its growth after roughly $4\ t_{\rm min}$. When fragmentation occurs the stretching time is almost a factor 2 larger then both the free-fall and thermal time, although it is still a 10 smaller then the tidal time.

The second important outcome of figure 2.6 is that the fragmentation occurs right after the free-fall time becomes shorter than the thermal time. This suggests that the fragmentation is a consequence of the pressure failing in balancing the stream self-gravity rather then an overcome of the black hole tidal forces or of the

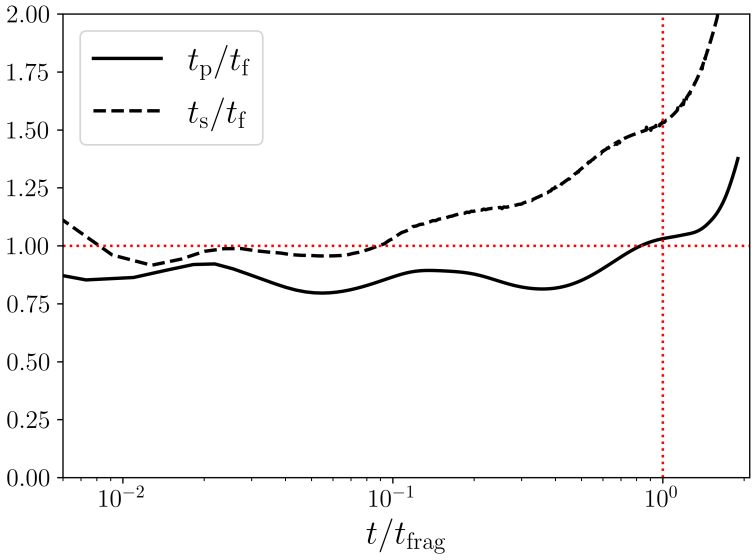

Figure 2.7: *The solid black line is the ratio between thermal and free-fall time, the dashed black line between stretching and free-fall time. In red are shown the fragmentation time (vertical line) and the level at which the two considered time scales are equal (horizontal line).*

stream stretching by the gravitational collapse. This is better shown in figure 2.7: the solid black line represents the ratio between the free-fall time and the thermal time while the dashed black line the ratio between free-fall time and stretching time. The two red dotted lines highlight the time at which fragmentation occur (the vertical one) and the line on which the two considered time scales are equals (horizontal one).

2.3.3 *Initial stellar rotation*

As explained in Section 2.1, a stream of gas debris obeying to a polytropic equation of state with $\gamma \gtrsim 5/3$ is prone to fragmentation fueled by gravitational instabilities. The results of the previous Section prove that also the $\gamma = 5/3$ case is susceptible of fragmentation.

An interesting factor that can be taken into account and could potentially slow down the fragmentation process is the stellar rotation. In this Chapter, we will focus on a configuration where the stellar initial rotation shares direction and sense with the orbital angular momentum of the star itself.

We will not treat the case where the rotation is able to prevent the stellar tidal disruption. This occurs when the stellar rotation is sufficiently fast and its axis is parallel and opposite to the stellar orbital angular momentum, or within some

tens degrees from this configuration. In this case the stream does not form or it is extremely faint (cfr. previous Chapter and Sacchi & Lodato 2019) and therefore is not relevant to the problem at hand.

If at least one component of the initial stellar rotation lies in the orbital plane there will be another force acting upon the debris stream: the centrifugal force inherited from the star. This force will add support against the collapse, counteracting to some extent the self-gravity of the stream and making it harder for it to fragment.

In the case considered here, where the rotation axis is perpendicular to the orbital plane, no additional force is added to the picture described above, the only thing that gets modified is the stellar internal structure and mass-energy distribution, that gets wider. This is due to a swelling of the rotating star with respect to the non-rotating case. A wider mass-energy distribution would cause a faster stretching of the stream, thus slowing down the fragmentation process.

To better understand this configuration and test our prediction, we performed a numerical simulation, adding an initial stellar rotation ($\alpha = 0.2$).

The simulations confirm our predictions about the role of stellar rotation aligned with the orbital angular momentum of the star: the time at which fragmentation occurs gets delayed by $\approx 15\%$. The delay is caused by the bigger stretching that a wider initial mass-energy distribution provokes.

Figure 2.8 shows the stretching parameter for the non rotating (solid black line) and rotating case (dashed black line) as a function of time (at the fragmentation time specific of each configuration). One can notice how, in the rotating case, the stretching is bigger, but only by $\approx 5\%$, this is however sufficient to produce the aforementioned amount of delay in the fragmentation time. This is due to the fact that the time scales have the same magnitude, thus a small changing in the value of one of the forces can lead to a significant difference in the evolutionary pattern of the stream.

2.4 - **Analytical estimate of fragmentation condition**

We provide here a simple analytical framework to understand the physics behind the fragmentation process, described by our numerical simulations.

The formalism to study the equilibrium and the time evolution of cylinders of gas has been developed since the sixties of the past century to describe the filaments of gas found in gaseous star-forming regions (for a review, see i.e. André et al. 2014). The standard case in the star-formation scenario is that a *contracting* cylinder increases its density while shrinking, accreting material from the parental cloud, until it becomes gravitationally unstable and fragments, thus forming smaller scale structures called cores. In the literature of this field several criteria have been found

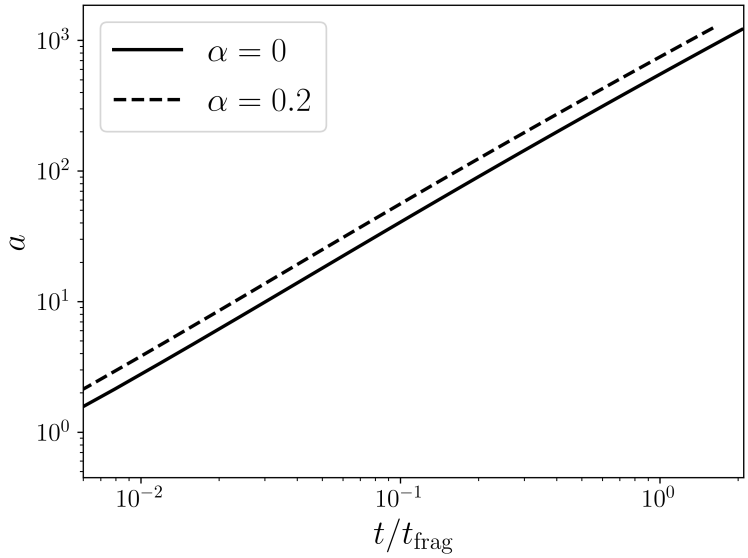

Figure 2.8: *The plot shows the stretching parameter for the non-rotating (solid black line) and rotating case (dashed black line) as a function of time (normalized to the fragmentation time).*

for the stability of polytropic cylinders of gas (see i.e, Ostriker 1964; Inutsuka & Miyama 1992). In particular, a fundamental condition that has to be satisfied in order to allow the gravitational collapse of filaments is that the linear mass-density of the filament should be larger than two times the square of the sound speed:

$$\Lambda = \frac{\mathrm{d}M}{\mathrm{d}l} \gtrsim \frac{2c_{\rm s}^2}{G} \tag{2.6}$$

where $\Lambda = \mathrm{d}M/\mathrm{d}l$ is the linear mass density computed as $\rho\pi H^2$. We can translate mathematically this picture into our case just by inverting the sign of the adopted stretching. While in the star formation case the shrinking of the filaments enhances the tendency for collapse, in our case the opposite occurs, as the filament is stretched out to lower mean densities. Thus, in this case, the effect of the stretching is to dilute the fluctuations and can in principle prevent the formation of fragments if the expansion is sufficiently fast in comparison with the free-fall time.

We consider the stream as a gas cylinder (a similar approach has already been adopted by Coughlin & Nixon 2019). Furthermore we consider the cylinder to be in hydrostatic equilibrium along its transverse section (we will discuss later the limits of this assumption. However, for an analytical analysis of the stability of a polytropic cylinder of gas see i.e Toci & Galli 2015). The transverse width of the

stream is thus:

$$H \simeq \frac{c_s^2}{\sqrt{4\pi G\rho}}. \tag{2.7}$$

Finally, we assume the cylinder to be free-falling onto the black hole (this assumption too will be discussed later on).

We use cylindrical coordinates so that the cylinder length is $l(t) = l_0 a(t)$ and its width is $H(t) = H_0 b(t)$[1], with the boundary conditions that $a(0) = b(0) = 1$.

The first step, in order to determine how all of the interesting quantities evolve, is to find a relation between the scaling factors a and b and link their time evolution to the evolution of the physical quantities of the stream. Mass conservation within the stream implies:

$$H^2 l\rho = const., \tag{2.8}$$

which, combined with Eq. 2.7, gives both the stream density as a function of a and the polytropic index γ

$$\rho \propto a^{1/(1-\gamma)}, \tag{2.9}$$

and a relation linking the scaling factors:

$$b \propto a^{(2-\gamma)/(2\gamma-2)}. \tag{2.10}$$

For the $\gamma = 5/3$ case we can compare this prediction with our simulation: figures 2.9 and 2.10 show the behaviour of the mean density of the stream and the stretching parameter b, respectively (solid black lines) and the predicted dependency (dashed lines), as functions of the scaling parameter a. The expected behaviour is strikingly fulfilled for all of the stream evolution ($b \propto a^{1/4}, \rho \propto a^{-3/2}$), prior to fragmentation.

The time evolution of all the time-scales introduced in Section 2.3 is related to the time evolution of these key quantities, all expressed as a function of the scaling factor $a(t)$. The knowledge of the time dependency of the scaling factor a would allow us to derive all of the quantities as explicit functions of the time t and the polytropic index γ. In the next Subsection we derive an analytical solution for the evolution of the debris stream and therefore for the evolution of $a(t)$.

2.4.1 *Dynamics of the debris stream*

Here, we consider the dynamics of the debris stream after disruption as composed of test particles freely falling in the radial direction in the gravitational field of the black hole. This approach is the same as the one of Coughlin et al. (2016b), who first considered the evolution of the structure of the debris stream in a semi-analytical

[1]Note that the analytic expression for the value of H_0 can be found i.e. in Ostriker 1964.

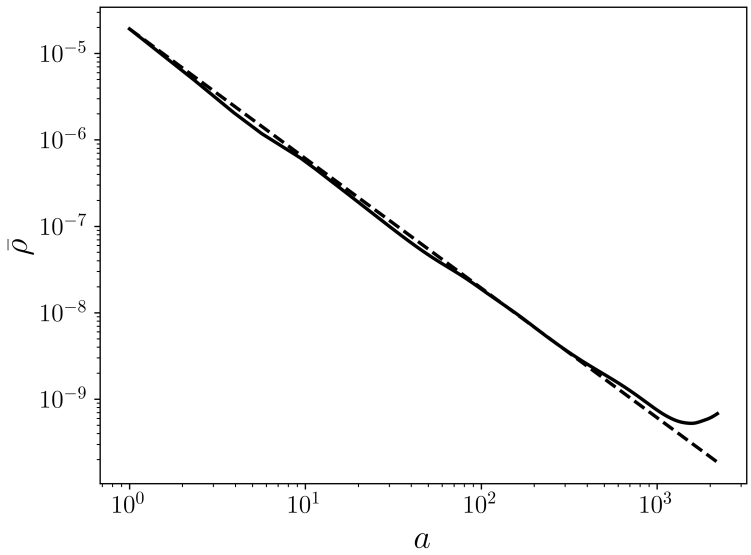

Figure 2.9: *The plot shows the mean density of the stream (solid black line) as a function of the stretching parameter a. The dashed line indicates the $a^{-3/2}$ predicted behaviour for the $\gamma = 5/3$ case covered by our simulation.*

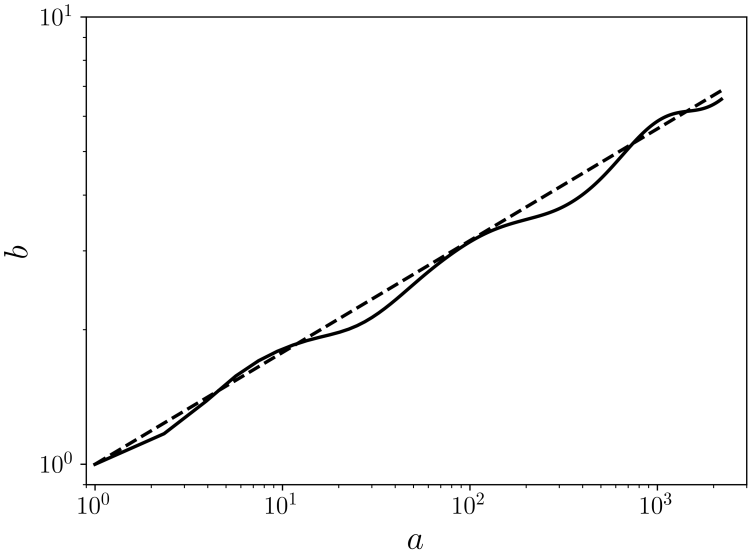

Figure 2.10: *The plot shows the stretching parameter b (solid black line) as a function of the stretching parameter a. The dashed line indicates the $a^{1/4}$ predicted behaviour for the $\gamma = 5/3$ case covered by our simulation.*

way. They adopt the same simplification of radial freely falling particles and find that this is a very good approximation for the post-disruption hydrodynamical stream. Coughlin et al. (2016b) find approximate solutions for the position and velocity of the stream elements in the limit where the particles are close to the marginally bound orbit, that corresponds to the stream center of mass. Here, as described below, we generalize the solution of Coughlin et al. (2016b) and find an exact analytical solution for the whole of the stream. We then argue that it is the deviation from the "close to marginally bound" orbits that causes fragmentation.

The equation of motion of the debris is:

$$\frac{1}{2}\left(\frac{\mathrm{d}r}{\mathrm{d}t}\right)^2 = \frac{GM_\mathrm{h}}{r} + E, \tag{2.11}$$

where bound, marginally bound, and unbound orbits are defined by $E < 0$, $E = 0$ and $E > 0$, respectively. The solutions to these equations are well known since they are the standard Friedmann equations used in Cosmology to describe a matter dominated universe in the closed, flat and open case, respectively (Friedman, 1922). For the marginally bound orbit (corresponding to a flat Universe) we have (see also Eq. 8 in Coughlin et al. 2016b)

$$R(t) = \left(\frac{9}{2}GM_\mathrm{h}\right)^{1/3} t^{2/3}, \tag{2.12}$$

for the unbound debris (corresponding to an open Universe) we have a parametric solution:

$$r(\eta) = r_0(\cosh\eta - 1), \qquad t(\eta) = t_0(\sinh\eta - \eta), \tag{2.13}$$

while for the bound debris (corresponding to a closed Universe) we have:

$$r(\eta) = r_0(1 - \cos\eta), \qquad t(\eta) = t_0(\eta - \sin\eta), \tag{2.14}$$

where $r_0 = GM/|2E|$ and $t_0 = GM/|2E|^{3/2}$ are the definition of a scale radius and a scale time, that depend on the energy of the debris E. These expressions give parametrically the exact positions of the debris elements across the whole stream (cf. the approximate positions given in Eq. 19 in Coughlin et al. 2016b)

It is instructive to approximate the above solutions for small η, which corresponds to orbits close to the marginally bound case. This is obtained by expanding the hyperbolic and the trigonometric sine and cosine as:

$$\cosh\eta - 1 \sim \frac{\eta^2}{2} + \frac{\eta^4}{24}, \qquad \sinh\eta - \eta \sim \frac{\eta^3}{3}, \tag{2.15}$$

$$1 - \cos\eta \sim \frac{\eta^2}{2} - \frac{\eta^4}{24}, \qquad \eta - \sin\eta \sim \frac{\eta^3}{3}. \tag{2.16}$$

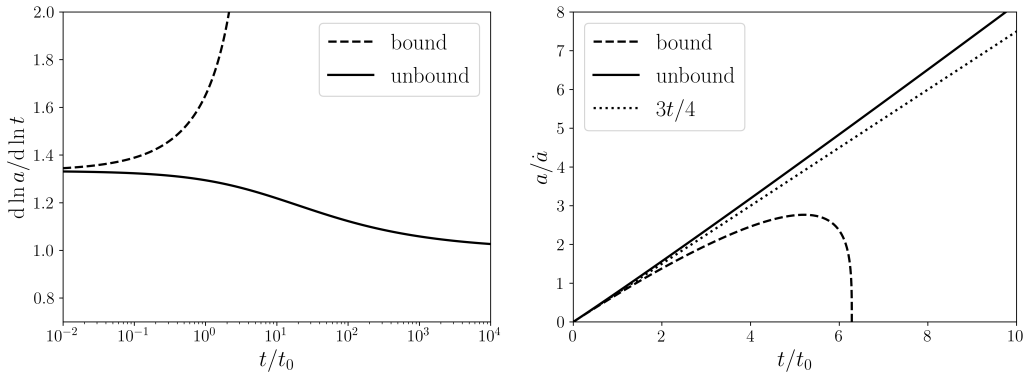

Figure 2.11: *Left: logarithmic derivative of the stretching parameter from our analytical solutions for the bound and the unbound portion of the stream as functions of time (normalized to the the scale time t_0). Right: evolution of the stretching time $a/\dot{a}$ for the bound and unbound debris, compared to the approximate value in the marginally bound case (dotted line).*

In this limit, for both bound and unbound orbits, we obtain:

$$r(t) = R(t)\left(1 + \frac{1}{3}\frac{ER(t)}{GM}\right). \tag{2.17}$$

The relative position with respect to the center of mass of the stream is then

$$l(t) = r(t) - R(t) = \frac{1}{3}\frac{E}{GM}R(t)^2 \sim t^{4/3}, \tag{2.18}$$

that implies that $a \propto t^{4/3}$ (cf. again Coughlin et al. 2016b, their Eq. 16). Actually, our exact solution allows us to compute the evolution of $a(t)$ for the whole stream. Figure 2.11 (left panel) shows the logarithmic derivative of the stretching parameter $a(t)$ for the bound (dashed line) and the unbound (solid line) portion of the stream. One can see that initially both are close to the expected value of $4/3$, while at late times (which occurs progressively earlier in physical time the farther we move away from the marginally bound orbit) the stretching of the unbound debris slows down, eventually reaching freely streaming orbits, where $a(t) \propto t$, while the bound debris are stretched faster, as the tide of the black hole increases. Similarly, one can compute the stretching timescale $t_\mathrm{s} = a/\dot{a}$, shown in Figure 2.11 (right panel), which grows faster (slower) than $3t/4$ for the unbound (bound) portion of the stream.

Coughlin et al. 2016b obtain their evolution by solving in a relatively complicated way the equation of motion of the debris, by introducing a parameter ξ, defined as:

$$\xi = \sqrt{\frac{2GM_\mathrm{h}}{r^3}}t = \frac{2}{3}\left(\frac{R}{r}\right)^{3/2}, \tag{2.19}$$

which is a measure of how far from the marginally bound orbit a stream element is. They further make the reasonable but in principle not justified assumption that the stream velocity follows a self-similar solution:

$$v_r = \sqrt{\frac{2GM_\mathrm{h}}{r}} f(\xi), \tag{2.20}$$

and finally solve numerically for f from an ordinary differential equation. They also provide an approximate solution for $f(\xi)$ in the form $f = 1/\xi - 1$, which they then use to compute the evolution of the stream far from the marginally bound orbit.

Our approach allows us to bypass all this and obtain an analytical and exact solution for $f(\xi)$, at the same time allowing us to demonstrate that the radial velocity is indeed self-similar.

Let us first consider the behaviour close to the marginally bound orbit, Eq. 2.17. The radial velocity is readily obtained:

$$v_r = \frac{\mathrm{d}r}{\mathrm{d}R}\frac{\mathrm{d}R}{\mathrm{d}t} = \sqrt{\frac{2GM_\mathrm{h}}{R}}\left(\frac{2r}{R} - 1\right) = \sqrt{\frac{2GM_\mathrm{h}}{r}}\left[2\left(\frac{r}{R}\right)^{3/2} - \left(\frac{r}{R}\right)^{1/2}\right], \tag{2.21}$$

and, recalling the definition of ξ, we obtain

$$f(\xi) = \frac{4}{3\xi} - \left(\frac{2}{3\xi}\right)^{1/3}, \tag{2.22}$$

which has the properties $f(2/3) = 1$ and $f'(2/3) = -5/2$ (cfr. Coughlin et al. 2016b). We thus see that, indeed, the *ansatz* by Coughlin et al. (2016b) that the solution would be self-similar with respect to the variable ξ is indeed correct, at least for particles close to the marginally bound orbit, as it only depends on how far does the particle lie with respect to the stream center of mass. We shall see in a moment that the self-similarity extends to the whole stream exactly.

The function in Eq. 2.22 approximates very well the full solution in the vicinity of the marginally bound orbit but fails farther from it. Actually, an exact and closed form analytical expression for $f(\xi)$ can be obtained by differentiating Eqs. 2.13 and 2.14:

$$v_r = \frac{(\mathrm{d}r/\mathrm{d}\eta)}{(\mathrm{d}t/\mathrm{d}\eta)}. \tag{2.23}$$

After some simple algebra, we can thus obtain $f(\xi)$ parametrically:

$$f = \frac{\sin\eta}{\sqrt{2(1-\cos\eta)}}, \qquad \xi = \frac{\sqrt{2}(\eta - \sin\eta)}{(1-\cos\eta)^{3/2}}, \tag{2.24}$$

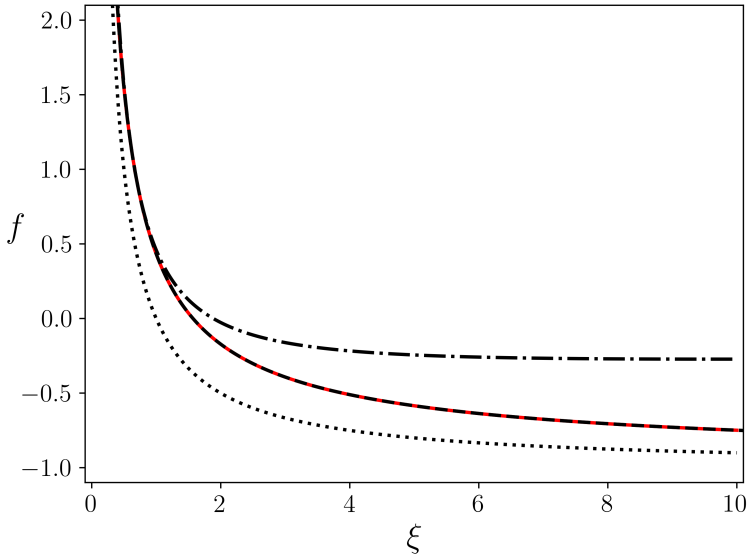

Figure 2.12: *The dashed black line shows the analytical function f superposed to the solid black line obtained solving numerically Eq. 4 by Coughlin et al. (2016b). The dotted line and the dash-dotted one show respectively the approximated solutions proposed by Coughlin et al. (2016b) and by us.*

for the bound portion of the stream ($\xi > 2/3$) and

$$f = \frac{\sinh\eta}{\sqrt{2(\cosh\eta - 1)}}, \qquad \xi = \frac{\sqrt{2}(\sinh\eta - \eta)}{(\cosh\eta - 1)^{3/2}}, \tag{2.25}$$

for the unbound portion of the stream ($\xi < 2/3$). In Figure 2.12 we plot the analytical function $f(\xi)$ as described above (dashed black line), the numerically computed function based on solving Eq. 4 in Coughlin et al. (2016b) (solid red line), and the two approximations: (i) the function $f = 1/\xi - 1$ proposed by Coughlin et al. (2016b) (dotted line) and (ii) the function we propose in Eq. 2.22 above (dash-dotted line). As we can see, Eq. 2.22 provides a better approximation (with respect to $f = 1/\xi - 1$) to the actual solution close to the marginally bound orbits, but fails to reproduce the asymptotic behaviour, especially for the bound portion of the stream ($\xi \gg 1$). On the contrary, the exact solution, Eqs. 2.24 and 2.25, does recover the numerically computed one. We also plot in Figure 2.13 the resulting radial velocity at a given time $t \approx 25\ t_{\rm min}$, where in red we show the distribution obtained from our SPH simulation and the various lines indicate the distribution obtained using our approximate solution close to the marginally bound debris (Eq. 2.22, dash-dotted line) and the one from Coughlin et al. (2016b) approximated function described above (dotted line). We do not

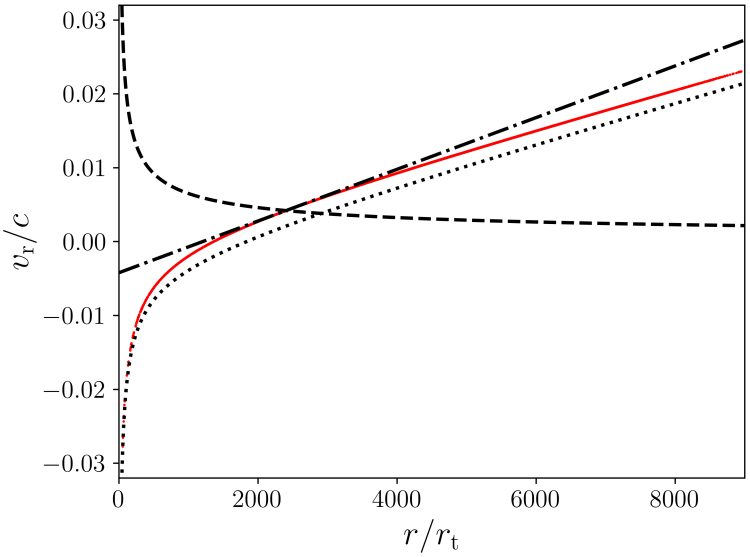

Figure 2.13: *The red line shows the velocity distribution of the stream from our SPH simulation at* $t \approx 25\, t_{\mathrm{min}}$. *The velocity distribution obtained using the approximate formula proposed by us (which applies only close to the marginally bound debris) is shown with a dash-dotted line, while the approximate solution by Coughlin et al. (2016b) is shown with a dotted line. We do not plot here our exact solution because it coincides perfectly with the simulated one. We also plot the radial velocity profile of the marginally bound material (dashed line). The intersection of this line with the simulated one indicates the location of the marginally bound debris in the stream.*

plot our exact solution because it coincides exactly with the numerical simulation. We also indicate, with a dashed line, the marginally bound orbit velocity profile. The intersection of this line with the simulation data marks the location of the marginally bound debris. Again, the general conclusion is that our exact solution is an excellent representation of the simulation data, that our approximate expression (Eq. 2.22) is a good approximation close to the marginally bound debris but fails away from it, and that the Coughlin et al. (2016b) proposed function, while not approximating the actual solution at any point, gives a fair first order description of the asymptotic regimes.

We are now in a better position to evaluate the stability of the stream. We have seen that the stretching of the orbits initially proceeds as $t^{4/3}$, but then slows down in the unbound portion of the stream and accelerates in the bound portion.

2.4.2 *Stream stability*

Now that we know the time dependency of the stream density and the scaling factors, it is straightforward to derive all of the other quantities and time-scales behaviours.

In Section 2.3 we introduced four time scales, each linked to one of the force acting on the stream. Here we will neglect the tidal time as this is much larger than the others and thus is not expected to play a role in the fragmentation process.

We have then the stretching time, the thermal one and finally the free-fall time. The first two stabilise the stream while the latter is ultimately responsible for fragmentation.

The stretching time dependence is the easiest to derive as this time scale is simply defined as $t_\mathrm{s} = a/\dot{a}$ and therefore

$$t_\mathrm{s} \propto t, \tag{2.26}$$

at least initially, bearing no dependence on the polytropic index.

We recall that the thermal time is defined as $t_\mathrm{p} = H/c_\mathrm{s} \propto 1/\sqrt{\rho}$, where we used the condition of hydrostatic balance in the transverse direction. Since $\rho \propto a^1/(1-\gamma)$ (Eq. 2.9)

$$t_\mathrm{p} \propto a^{1/2(\gamma-1)} \propto \begin{cases} t^{2/3(\gamma-1)} & t \ll 1 \\ t^{1/2(\gamma-1)} & t \to \infty \end{cases}. \tag{2.27}$$

Finally, also the free-fall time scale, defined as $t_\mathrm{ff} = 1/\sqrt{2\pi G\rho}$ is proportional to $1/\sqrt{\rho}$ and thus scales with time in the same way as the thermal time. Actually, the assumption of hydrostatic balance in the transverse direction implies that the stream is always close to marginal stability, according to the Ostriker (1964) criterion,

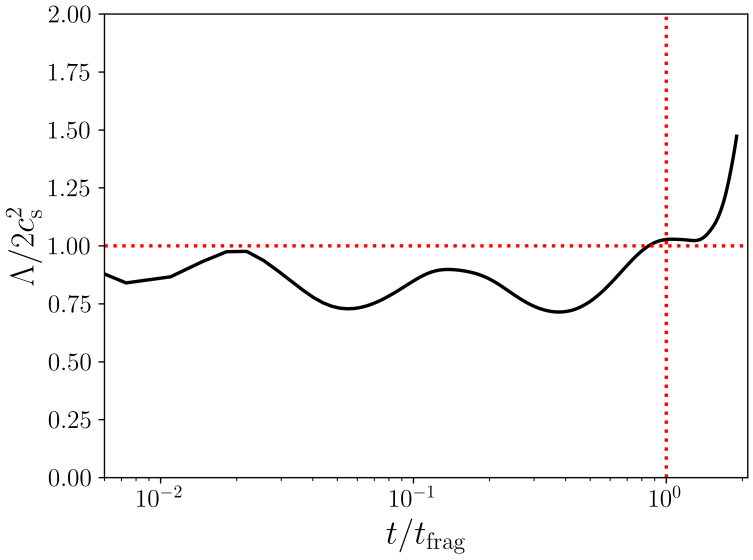

Figure 2.14: *The solid black line shows the quantity $\Lambda/2c_s^2$ that must be grater then 1 in order for a gas cylinder in hydrostatic equilibrium to become gravitationally unstable and fragment.*

$\Lambda \sim c_s^2/2G$ and thus fragmentation would ensue relatively easily. However, as long as the stream stretching occurs on the same timescale, this can act to stabilise it.

It is therefore clear why the $\gamma = 5/3$ case is the critical one: for this particular value of the polytropic index all of the relevant time scales share the very same time dependence, at least initially: $t_{\rm ff,sc,s} \propto t$, the stream stays therefore marginally stable for a long time. After some time however the time evolution of the thermal and free fall time scales slows down and they disentangle from the stretching time. This can be seen in Figure 2.6, and is due to the fact that at late times (when the stream starts to freely stream) they tend to be proportional to $t^{3/4}$ while the stretching time remains proportional to t.

In the case of more compact stars ($\gamma > 5/3$) the stream stretching along its axis is less efficient than all of the others time scales and therefore the streams fragments much faster than in the $\gamma = 5/3$ case. In all of the cases where $\gamma < 5/3$ the stretching grows faster than the other forces and is therefore able to sustain the stream and prevent its fragmentation.

Figure 2.14 shows with a solid black line the quantity described in Eq. 2.6 while the two dotted red lines highlight again the fragmentation time and the level at which the condition is satisfied. We can see that the condition is almost satisfied during all of the stream evolution. It rapidly grows above unity right before the stream collapses, hence confirming that the stream can be considered in hydrostatic

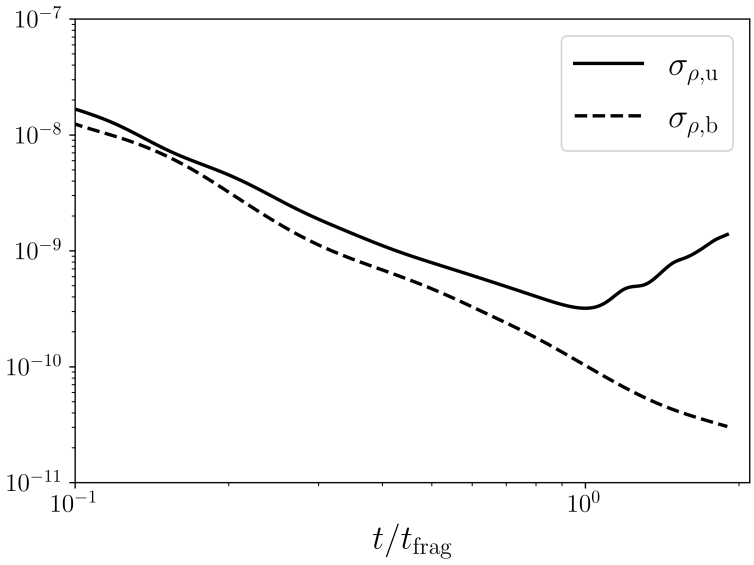

Figure 2.15: *The plot shows the density fluctuations of the unbound (solid black line) and bound (dashed black line) part of the stream as functions of the fragmentation time of the unbound material.*

equilibrium for the part of its evolution we are interested in.

All of the arguments presented above consider only the unbound part of the stream. Employing our analytical results we can however infer that in the bound part the stretching time falls rapidly below all of the other time-scale and thus should prevent the fragmentation of that portion of the stream. This is indeed what we observe in our simulations, too. Figure 2.15 shows the density fluctuations in the unbound (solid black line) and bound (dashed black line) part of the stream as a function of time. The absence of a turning point in the stream of bound material signals that little to no fragmentation is found in the bound debris before they enter the region in which they are considered to be accreted.

2.5 - **Conclusions**

The pioneering work of Coughlin & Nixon (2015), further developed by Coughlin et al. (2016a,b), studied, among other things, the gravitational stability of the debris streams forming after the disruption of a star by a SMBH. They found that a stream composed by a gas obeying a polytropic equation of state with polytropic index $\gamma \gtrsim 5/3$ is susceptible to fragmentation. This fragmentation is caused by the onset of gravitational instabilities, that are able to overcome pressure forces within the

gas and the tidal force of the black hole. The stream therefore would collapse under its self-gravity forming spheroidal blobs of gas. It is not however completely clear whether the critical $\gamma = 5/3$ is subject to fragmentation or not. In order to confirm whether also the $\gamma = 5/3$ case is affected by gravitational fragmentation, and to better understand the physic behind this process, we performed high resolution numerical simulation using a 3D SPH code.

We found that a stream of gas debris resulting from the disruption of a star, modelled as a polytropic sphere with adiabatic index $\gamma = 5/3$, is indeed prone to fragmentation. Through a convergence test we determined however that, for standard TDE parameters, fragmentation occurs only after more than 3 years since disruption, and only in the unbound part of the stream. This means that no observational effect of the fragmentation is to be expected on the light-curve of the event. In order to confirm this hypothesis however it would be necessary to observe one such event continuously for several years which is unfortunately above the possibility of current facilities.

We have also successfully described the process leading to stream fragmentation using an analytical approach that generalize the results of Coughlin et al. (2016b), assuming that the stream can be modeled as a stretching cylinder and deriving a fragmentation condition that is more accurate than the ones previously suggested in the literature. In this picture, fragmentation is driven by the stream self-gravity and is resisted by pressure and by the stream stretching along its axis. For $\gamma = 5/3$, as the stream expands, initially all the timescales associated with collapse, pressure and stretching grow with time at the same rate. However, at later times, we have demonstrated that the stretching time-scale is unable to keep up with the two others time-scales and fragmentation ensues rapidly. Conversely, for $\gamma > 5/3$, our argument predicts that the stretching time scale is always much longer than the pressure and self-gravity timescales, implying an increased tendency for collapse, as observed.

Further, our analysis predicts that the stretching time-scale should fall below all the others in the bound portion of the stream stabilizing it. This is indeed what we observe in our simulations: the bound material shows little to no fragmentation before entering the region where we consider it to be accreted.

While we were working on the present Chapter, we became aware of the recent work by Coughlin & Nixon (2020) on the general problem of the stability of a hydrostatic adiabatic self-gravitating filament. They find that the filament in unstable and propose that the very same instability is at the origin of stream fragmentation in TDE. The applicability of such analysis to TDE is not immediate, as already noted by Coughlin & Nixon (2020), since (i) a TDE stream is not hydrostatic and (ii) the stream evolves significantly due to the presence of the tidal field of the black hole, that is not included in their analysis. Here, we propose instead that the origin of the fragmentation, as discussed above, lies in the slowing

down of the stretching of the debris in the unbound portion of the stream.

3 Supersoft, luminous X-ray sources in galactic nuclei

Tidal Disruption Events (TDEs) are usually discovered at X-ray or optical wavelength through their transient nature. A characteristic spectral feature of X-ray detected TDEs is a "super-soft" X-ray emission, not observed in any other extragalactic source, with the exception of a few, rapidly variable hyper-luminous X-ray sources or supersoft AGN which are however distinguishable by their optical emission.

The goal of our work is to find interesting extragalactic supersoft sources associated with galactic centres. In this category of sources would fall overlooked TDEs, supersoft AGN and nuclear HLXs. Finding such sources would allow the study of extreme regime accretion on different black hole mass scales.

We searched for Super-Soft X-ray sources (SSS) by cross-correlating optical and X-ray catalogues, and looking for very steep spectrum (photon index $\Gamma > 3$) and high luminosity ($L_X > 10^{41}$ erg s^{-1}) in the X-ray in extragalactic near-nuclear sources.

With our blind search we retrieved about 60 sources. Among this 15 are previously known as AGN or TDEs, so demonstrating the efficiency of our selection. 36 sources, although showing steeper-than-usual spectra were considered standard AGN in according with their optical classification. The remaining 9 sources are previously unknown sources showing spectral properties consistent with the emission by a TDE (4 sources) or by extremely soft-excess dominated AGN (5 sources).

For 2 of the 4 candidate TDEs 2 points lightcurves are available (one form archival data and the other from a follow-up requested by the author). The fact that both show significant variability (by a factor > 20 in both cases) strongly favors a TDE explanation for all 4 candidates which represents the first ever tidal disruption events discovered by a spectroscopic analysis.

3.1 - **Introduction**

Supersoft X-ray sources (SSS) are objects that emit in the X-ray band with typical temperatures corresponding to X-ray energies of about 20-100 eV and observed luminosities rarely exceeding few times 10^{38} erg s^{-1}, but well above what can be produced in stellar coronae. Traditionally, SSS are mostly associated with accreting white dwarf (WD) systems where mass transfer leads to nuclear fusion on the WD surface either in the form of runaway events (as in classical novae) or in a steady manner for some systems with high mass accretion rate. Today ~ 80 novae have been observed in the X-ray band including extragalactic ones in MCs, M31 and M33 (see Della Valle & Izzo 2020 and references therein for a review). However, novae and/or steady nuclear burning WD are not the only known extragalactic SSS, and some intriguing classes of X-ray emitting objects appear to sometimes fall in this very same category. In particular, possible high-luminosity members of this class may include soft Ultra-Luminous X-ray Sources (ULX), Tidal Disruption Events (TDE), and supersoft AGN whose X-ray luminosity is almost entirely emitted below ~ 2 keV. Heavily obscured AGNs may also predominatly shine in the soft X-ray band because reprocessed/scatterd emission on large scales can easily dominate over the heavily absorbed intrinsic emission for large enough column densities.

Ultraluminous X-ray sources (ULXs) are defined as off-nuclear X-ray sources with luminosities exceeding 10^{39} erg/s. Detailed observations and modeling in recent years favour an interpretation of the ULX phenomenon in terms of super-critical accretion onto stellar mass black holes and neutron stars (e.g. Middleton et al. 2012, 2015; Bachetti et al. 2014). Unlike typical ULX which are often associated with significant emission above 1-2 keV, a sub-class of sources dubbed ultraluminous supersoft X-ray sources (or ULSs) are dominated by a thermal-like component with typical effective temperature of 50-200 eV possibly due to reprocessing in an optically thick outflow blocking most/all hard X-ray photons from view (see e.g. Urquhart & Soria 2016; Feng et al. 2016; Pinto et al. 2017). On the other hand, the most luminous examples of ULXs ($L_{\rm X} \gtrsim 10^{41}$ erg s^{-1}), known as hyperluminous X-ray sources (HLXs), are of particular interest as they can be considered bona fide intermediate mass black hole (IMBH) candidates (e.g. Farrell et al. 2009). As the thermal X-ray emission from accretion discs around IMBHs is naturally expected to dominate the soft X-ray band, accreting IMBH candidates are likely to be observed as hyperluminous ULS. Most ULX (and HLX) searches so far are biased in favour of off-nuclear sources to avoid potential confusion with Active Galactic Nuclei (AGN), see e.g. Barrows et al. (2019). However, IMBHs are expected to be found also in the nuclear regions (Chilingarian et al., 2018).

Tidal disruption events (TDEs) occur when a star wanders too close to a supermassive black hole. The tidal forces of the hole tear the star apart and destroy

it. The stellar debris get subsequently partly ejected and partly accreted onto the hole generating a bright transient. The study of TDEs is of particular interest as this kind of events offers a unique way to investigate otherwise quiescent (non-AGN) supermassive black holes (SMBHs) that lurk in the centres of most known galaxies. The rapid evolution of the electromagnetic emission from TDEs (Rees, 1988; Phinney, 1989) also offers a unique opportunity to study different SMBH accretion regimes in the same source on human timescales. The optically thick accretion disc that the stellar debris should form around the hole is predicted to emit thermal radiation with a characteristic temperature of some tens of eV; this black body radiation would have a visible tail in the X-ray band, appearing as an extremely steep power-law spectrum (Saxton et al., 2021). Indeed the first candidates of TDEs were found in the ROSAT All Sky Survey as bright transient with very soft X-ray spectra ($\Gamma \approx 3-5$) (Bade et al., 1996). Today's most efficient methods employed to identify TDEs involve the detection of bright transients followed by multi-wavelength observations focused on determining their nature. The bright transients are usually spotted serendipitously, be it in the optical or X-ray band, by the comparison between old catalogues and new observations of large sky portions. Although these methods are efficient in finding new events, it is likely that several TDEs are hidden in available catalogues and archives, being spotted by chance at, or near, their luminosity peak.

Finally, a few X-ray supersoft AGN with peculiar optical and X-ray properties have emerged in recent years. 2XMM J123103.2+110648 (Terashima et al., 2012; Ho et al., 2012) is an optically classified Seyfert 2 galaxy with supersoft X-ray spectrum and significant X-ray variability, mostly associated with a claimed ~ 3.8 hr periodicity (Lin et al., 2013). Two other very similar objects, GSN 069 (Miniutti et al., 2013, 2019) and RX J1301.9+2747 (Sun et al., 2013; Shu et al., 2017; Giustini et al., 2020), exhibit spectacular recurrent X-ray variability in the form of short-lived and very high amplitude X-ray bursts occurring every few hours and superimposed to a quiescent constant level (quasi periodic eruptions, or QPEs, see Miniutti et al. 2019; Giustini et al. 2020). In all three cases, optical spectra show Seyfert-like narrow emission lines, but no sign of broad lines which may indicate past activity and recent re-activation. QPEs have later been detected in other two sources with no sign of black hole activity in the optical by eROSITA, and then confirmed with NICER and XMM-Newton follow-up observations (Arcodia et al., 2021). All of these sources are associated with exceptional X-ray variability, no sign for X-ray absorption, supersoft X-ray spectra, and general properties pointing towards relatively low mass black holes ($10^5 - 10^6$ $M_\odot$) and high mass accretion rates. The lack of broad optical emission lines in GSN 069 and RX J1301.9+2747 may perhaps be understood if these sources were long-lived TDEs rather than AGN, and indeed there are signs that this is case at least for GSN 069 (Sun et al., 2013; Lin et al., 2017a; Shu et al., 2018; Sheng et al., 2021).

Here we present preliminary results from a search for SSS X-ray sources associated with the central region of external galaxies restricted to X-ray luminosities exceeding 10^{41} erg s^{-1}. Our search could in principle reveal a sample of new overlooked TDE, nearly nuclear supersoft HLXs, and a population of supersoft AGNs to be studied.

3.2 - **Sources selection**

Our goal is to find potentially interesting nuclear supersoft X-ray sources in X-ray archives ranging from overlooked TDE candidates to supersoft AGNs and including nuclear HLXs that might have been missed by previous searches that systematically avoided the nuclear region to minimize confusion with AGNs. We searched for extragalactic supersoft X-ray sources in the XMM-Newton archive within 5", a distance comparable with XMM spatial resolution (Webb et al., 2020), from the galactic center of their host galaxies with high enough X-ray luminosity to make an origin in stellar processes highly unlikely.

We started by taking the more than 5.5×10^5 sources of the XMM-Newton catalogue of serendipitous sources (4XMM-DR9, Webb et al. 2020) and we computed i) the signal to noise ratios in the ultrasoft 0.2-0.5 keV (SNR_1) and soft 0.5-1 keV (SNR_2) bands as well as ii) the photon index Γ_{21} for the ultrasoft to soft band and that for the soft to medium (1-2 keV) band, Γ_{32}. In order to obtain SSS with good signal to noise, we selected all the point-like objects that had a high signal to noise ratio in both the ultrasoft and soft band ($SNR_1 > 7$, $SNR_2 > 3$) together with steep photon index in the ultrasoft band ($\Gamma_{21} > 3$). As this criterion would allow for little to no absorption we also selected the sources with high signal to noise ratio and steep photon index in the sole soft band ($SNR_2 > 7$, $\Gamma_{32} > 3$), but with an additional constraint on the photon index in the ultrasoft band ($\Gamma_{21} > -1$) to avoid star-forming regions and most heavily obscured AGNs, dominated by thermal/photo-ionized plasma emission in the soft X-ray band.

Then, we retrieved redshift information for as many sources as possible by cross-matching our sample with the available galaxy catalogues in SIMBAD, the largest one being SDSS DR16 (Ahumada et al., 2019), followed by 2dFGRS (Colless et al., 2003), 6dFGS DR3 (Jones et al., 2009) and LCRS (Shectman et al., 1996). We kept all the matches with an angular distance smaller than 5 arcseconds. Finally, we required the luminosity in the full 0.2-12 keV X-ray band of the selected galaxies to be larger then 10^{41} erg/sec. This selection process resulted in 61 sources.

One of these, SDSS J123408.85+090542.4, is the brightest cluster galaxy (BCG) of the compact cluster SDSSCGA 1202 (Yoon et al., 2008); this object was

	ultra-soft	soft
signal to noise ratio	$\mathrm{SNR}_1 > 7$, $\mathrm{SNR}_2 > 3$	$\mathrm{SNR}_2 > 7$
photon index	$\Gamma_{21} > 3$	$\Gamma_{32} > 3$, $\Gamma_{21} > -1$
luminosity	$L_{\mathrm{X}} > 10^{41}$ erg/s	

Table 3.1: *The table summarize the selection criteria in the ultra-soft and soft X-ray bands, see main text for details.*

promptly eliminated from the sample as the soft X-ray emission is the result of the gas warming in the potential well of the cluster rather than due to accretion phenomena. This is also confirmed by X-ray spectral analysis which reveals that emission by an optically thin, warm gas with fixed solar abundances reproduces the data well.

Out of the remaining 60 sources, 15 are well known sources characterized by rather extreme X-ray properties in terms of soft spectral emission and variability:

- 9 TDEs or TDE candidates: 2MASX J02491731-0412521 (Esquej et al., 2007), ASASSN-15oi (Holoien et al., 2016), ASASSN-14li (Maksym et al., 2014), 2XMM J123103.2+110648 (Lin et al., 2017b), 2MASS J12013602+3003052 (Saxton et al., 2012), SDSS J150052.07+015453.8 (Lin et al., 2017a), GSN 069 (Shu et al., 2018; Miniutti et al., 2019; Sheng et al., 2021), a super-soft AGN which produced a huge X-ray burst followed by a long-term decay and also exhibits QPEs, 2MASX J19271951+6533539, a changing look AGN for which the variability is thought to be caused by a TDE (Ricci et al., 2020), 2XMM J141711.0+522541 an off-nuclear transient which could be associated with a TDE onto an IMBH (Lin et al., 2016);

- 6 extreme AGNs, exhibiting exceptional short and/or long term variability coupled with super-soft spectra: RX J1301 (Giustini et al., 2020) which is associated with QPEs, 2MASX J10343860+3938277 that exhibits a very pronounced soft excess and quasi periodic oscillations (Gierliński et al., 2008), the highly variable narrow line Seyfert galaxies 4U 0708-49 (Boller et al., 2002), 2MASX J13251937-3824524 (Boller et al., 1997) and 2MASX J14062191+2223462 (Mallick & Dewangan, 2018), and PHL 1092, an extreme variability example of a weak line, often X-ray weak narrow line quasar (Miniutti et al., 2009).

All these 15 sources fall in the categories described in the introduction and represent therefore a reassuring sanity check of the ability to obtain the type of sources we are looking for from our selection criteria. As these 15 sources have been all

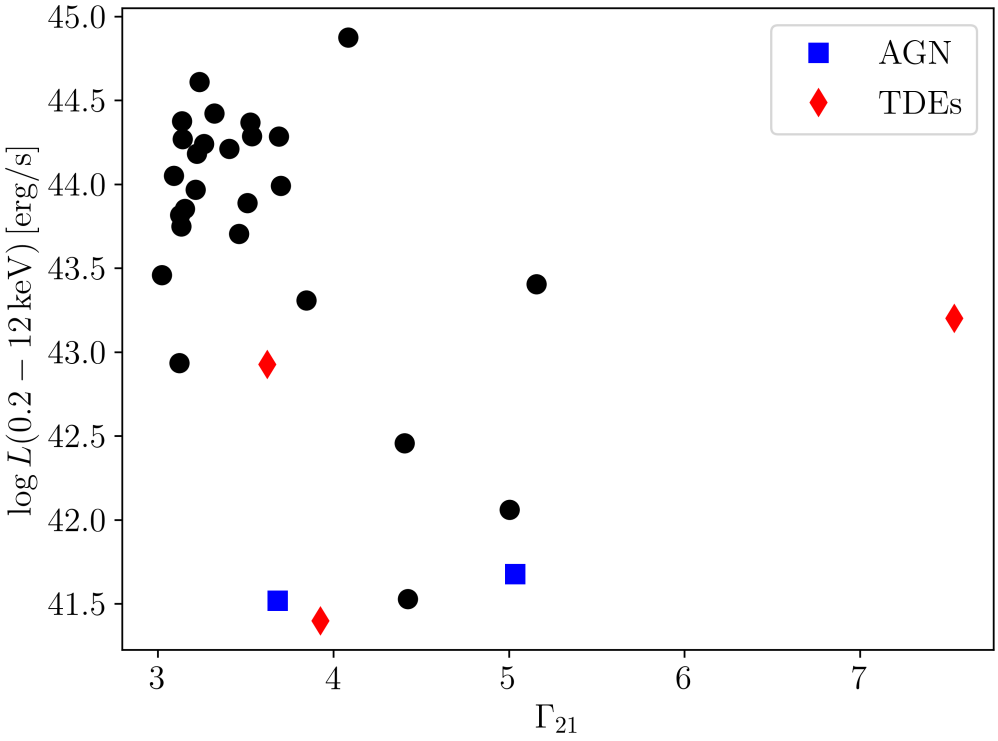

Figure 3.1: *The 31 sources brought forth by our selection in the ultrasoft band shown in the $L_X - \Gamma_{21}$ plane. Blue triangles and red diamonds show the 7 extreme AGN and 8 TDEs known in literature respectively. Uncertainties are not reported as the plot sole goal is to show the position of the sources in the plane and all quantities will be retrieved through complete spectroscopic analysis rather than photometric interpolation.*

extensively studied in the X-ray band in the past, we do not discuss them any further here.

Figures 3.1 and 3.2 show, in the $L_X - \Gamma_{21}$ and $L_X - \Gamma_{32}$ plane respectively, the 60 selected sources. Figure 3.1 shows the 31 sources selected in the ultrasoft band while Figure 3.2 the 29 retrieved from the soft band selection. The 7 extreme AGN and 8 TDEs known in literature are highlighted with blue triangles and red diamonds respectively. The black points represent the remaining 45 sources that are discussed below.

For each observation of the remaining 45 sources we retrieved the EPIC data from the XMM-Newton science archive and we reduced them following the standard procedure employing XMMSAS routines. EPIC PN data were reduced independently while MOS data were directly summed. Source and background products were extracted from circular regions centred on the source and from a concentric disjointed annulus respectively. For each observation response and ancillary files

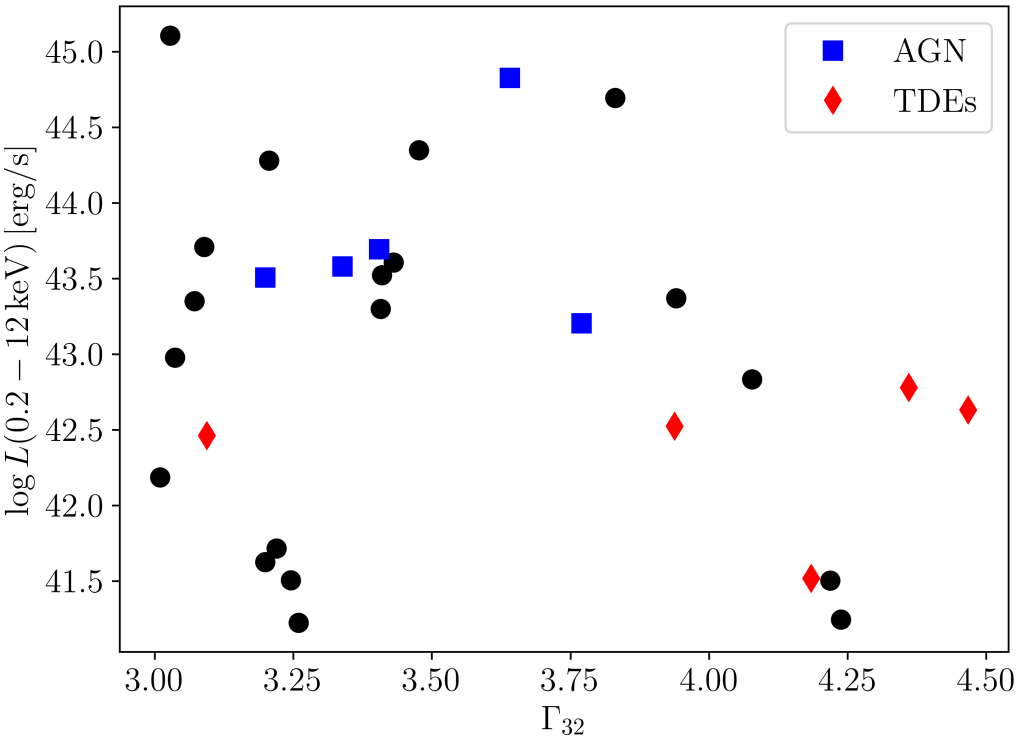

Figure 3.2: *The 29 sources brought forth by our selection in the soft band shown in the $L_X - \Gamma_{32}$ plane. Blue triangles and red diamonds show the 7 extreme AGN and 8 TDEs known in literature respectively. Uncertainties omitted as in the previous plot.*

were generated during product extraction. Data were regrouped in order to have at least one count in each channel (every further rebinning in presented spectra is purely graphical), and we employed the C-statistic for spectral fitting. We used the XSPEC package to analyse the spectra of our sources, considering data between 0.2 and 10 keV for the EPIC PN and between 0.2 and 7 keV for the MOS. We initially adopted a simple model composed by an absorbed blackbody plus powerlaw, redshifted to the sources distance (*zTbabs* $\times$ *(zBbody* + *zPowerlw)* in XSPEC) with an additional layer of absorption (*Tbabs*) with column density fixed to the Galactic value.

Of these source we identified:

- 30 sources optically classified as BLAGN (19 by Pâris et al. 2018, 4 by Véron-Cetty & Véron 2010, 3 by Pierre et al. 2016, 2 by Rakshit et al. 2017, 1 by Bär et al. 2017 and 1 by Esquej et al. 2013). Their X-ray emission, although often unusually steep, appears compatible with their optical classification and typically comprises a relatively strong soft excess with $kT \sim 100$-200 eV and a power law emission component dominating the hard energy band;

- 3 sources optically classified as Seyfert 2 galaxies. NGC 6264, classified by Véron-Cetty & Véron 2010, is a well known Compton-thick AGN hosting an H_2O megamaser (Castangia et al., 2013). 2dFGRS TGS243Z047 is classified as and heavily obscured AGN by Lacy et al. (2013). 2MASX J10181928+3722419 instead, classified by Toba et al. 2014, has its soft X-ray emission dominated by star-formation rather than nuclear activity (LaMassa et al., 2012).

- 2 sources, 2XMM J021704.5-050214 classified as an elusive AGN with star-forming activity (Menzel et al., 2016) and 2MASX J17020882+6412210, classified as a star-forming galaxy by Mickaelian et al. (2018). Their soft X-ray emission is in fact consistent with star-formation activity rather than accretion;

- 1 source, 2dFGRS TGS431Z029, classified as non-active galaxy (Lavaux & Hudson, 2011) as its optical spectrum does not show any emission line, has the distinctive X-ray emission of an obscured, possibly Compton-thick AGN.

The spectral parameters of these 36 sources are collected in Table 3.4 and they will not be further addressed.

The remaining 9 sources show peculiar X-ray spectral properties that are not immediately consistent with the their optical classification. The general properties

ID	ra	dec	redshift	label
[CRS2013] 4	336.536	17.405	0.115	D1
2XLSSd J021728.4-041346	34.368	-4.229	1.173	D2
[VV2006] J231419.8-525901	348.583	-52.984	0.156	P1
2XMM J122517.6+175726	186.324	17.957	0.805	P2
2XMM J022255.9-051352	35.733	-5.231	0.846	P3
SDSS J152717.95+164503.2	231.825	16.751	0.061	T1
2MASX J00414632-2827423	10.443	-28.462	0.074	T2
GAMA91637	212.876	0.472	0.177	T3
XXL-AAOmega J234255.95-543001.8	355.733	-54.501	0.286	T4

Table 3.2: *For the 9 sources whose X-ray spectral features are untypical for their optical classification we report here their general properties: SIMBAD identifier, ra and dec in degrees, redshift value and the label we will use hereafter to identify them.*

and identifier for these sources are collected in Table 3.2 and they will be further addressed individually in the following section.

3.3 - **Source description**

Here we describe in detail the sources whose X-ray properties do not resemble the typical AGN and/or that deviate from the expected behaviour based on optical classification. We modelled the X-ray emission of our sources using three different models:

- absorbed blackbody (*zTbabs* $\times$ *zBbody* in XSPEC);

- absorbed powerlaw (*zTbabs* $\times$ *zPowerlw* in XSPEC);

- absorbed blackbody + powerlaw (*zTbabs* $\times$ *(zBbody* + *zPowerlw)* in XSPEC);

each spectral component is redshifted to the source distance, and we added an additional layer of absorption (*Tbabs*) with column density fixed to the Galactic value to each spectral model. Figure 3.3 illustrates the model with the blackbody ($kT = 120$ keV) and powerlaw ($\Gamma = 2$) components in red and blue solid lines respectively and the resulting spectrum in solid black line.

When multiple observations were available for the same source, we fitted all observations jointly. We started by keeping all the fitted parameters linked together over different observations, freeing them one at the time and checking for any improvement of the statistics through an F-test with 5% acceptance threshold. The resulting best-fitting models and spectral parameters are reported in Table 3.3.

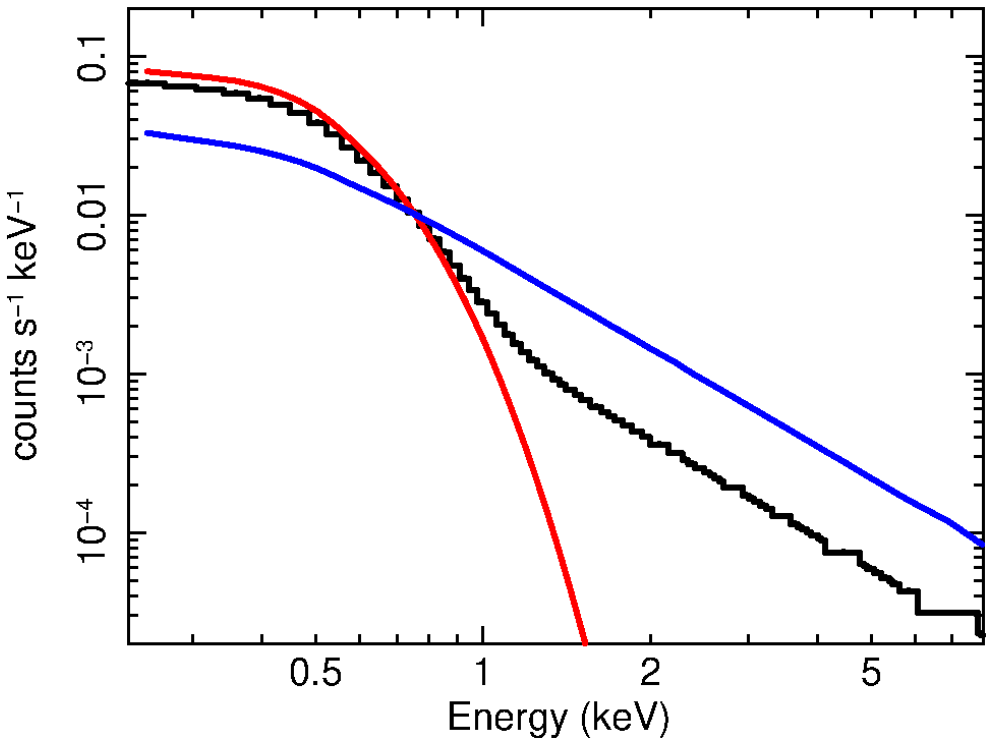

Figure 3.3: *The blackbody + powerlaw model (solid black line) with the two components highlighted in red and blue respectively. The choices of blackbody temperature ($kT = 120$ keV) and powerlaw photon index ($\Gamma = 2$) mirrors the typical value we found in our sample.*

As per X-ray light curves, we found no clear short-term variability or periodicity in our sample. As a cautionary remark, it is worth pointing out that this could be partly due the fact that the sources are generally faint, and therefore need temporal binning often larger then 1 ks in order to obtain satisfying signal to noise ratios in the single bins.

These 9 sources are divided into three groups based on their spectral properties, as detailed below.

Table 3.3: *The quantities in italic are fixed during the fit procedure, in boldface is the statistics of the best fitting model. The blackbody temperature is in keV, the extra-absorption Hydrogen column density is in* 10^{20} *atoms/cm*^{2} *units and when 0.0 is indicated, it was fixed to* 10^{-5} *atoms/cm*^{2}*. The extra-absorption columns are omitted for the blackbody and blackbody+powerlaw models as no extra-absorption was required in any source. The luminosity, expressed in erg/s, is computed over the 0.5-2 keV range and adopting the best fitting model, the luminosity of the first observation of the source labelled T4 is an upper-limit. Best-fitting results are highlighted in boldface. All quantities are reported along with their* 1σ *errors.*

lab.	date	blackbody		powerlaw			blackbody+powerlaw			$\log_{10} L$
		C/ν	kT	C/ν	$N_{\rm H}$	Γ	C/ν	kT	Γ	
D1	2010-8-20 2013-8-17 2015-5-30	**155/162**	$0.15^{+0.01}_{-0.01}$	179/162	*0.0*	$3.8^{+0.2}_{-0.2}$	159/160	$0.14^{+0.02}_{-0.02}$	$3.6^{+0.6}_{-0.7}$	$41.83^{+0.07}_{-0.07}$ $41.43^{+0.04}_{-0.04}$
D2	2007-1-8 2008-7-3 2015-2-6	281/267	$0.14^{+0.01}_{-0.01}$	**279/267**	*0.0*	$5.0^{+0.2}_{-0.2}$	278/265	*0.12*	$5.0^{+0.2}_{-0.4}$	$44.63^{+0.05}_{-0.05}$ $44.1^{+0.05}_{-0.05}$
P1	2011-5-8	104/49	$0.04^{+0.01}_{-0.01}$	106/49	*0.0*	$7.3^{+0.8}_{-0.7}$	**87/47**	$0.02^{+0.01}_{-0.01}$	$2.7^{+0.1}_{-0.1}$	$41.77^{+0.08}_{-0.09}$
P2	2004-7-7	39/51	$0.44^{+0.04}_{-0.04}$	**34/50**	$0.27^{+0.18}_{-0.15}$	$2.9^{+0.5}_{-0.4}$	-	-	-	$44.77^{+0.24}_{-0.2}$
	2010-12-8 2010-12-16 2010-12-18	375/158	$0.36^{+0.02}_{-0.02}$	292/158	*0.0*	$2.6^{+0.1}_{-0.1}$	**182/155**	$0.02^{+0.01}_{-0.01}$	$2.2^{+0.1}_{-0.1}$	$44.18^{+0.04}_{-0.04}$ $44.05^{+0.06}_{-0.05}$

Table 3.3: *Continued.*

lab.	date	blackbody		powerlaw			blackbody+powerlaw			$\log_{10} L$
		C/ν	kT	C/ν	$N_{\rm H}$	Γ	C/ν	kT	Γ	
P3	2001-7-4	**126/140**	$0.12^{+0.01}_{-0.01}$	134/140	*0.0*	$4.8^{+0.3}_{-0.3}$	164/138	$0.11^{+0.01}_{-0.01}$	$1.5^{+0.3}_{-0.3}$	$43.83^{+0.05}_{-0.05}$
	2016-7-30		$0.04^{+0.01}_{-0.01}$			$9.1^{+1.6}_{-1.6}$		$0.03^{+0.01}_{-0.01}$		
	2016-8-13		$0.24^{+0.03}_{-0.02}$			$3.0^{+0.3}_{-0.3}$				
	2017-1-4		*0.12*			*3.0*		$0.11^{+0.01}_{-0.01}$		
T1	2010-8-8	**224/234**	$0.06^{+0.01}_{-0.01}$	230/234	*0.0*	$6.1^{+0.4}_{-0.3}$	224/233	$0.06^{+0.01}_{-0.01}$	*3.0*	$41.04^{+0.09}_{-0.1}$
	2022-1-17									$39.74^{+0.14}_{-0.17}$
T3	2018-1-6	**97/95**	$0.06^{+0.01}_{-0.01}$	112/95	*0.0*	$6.3^{+0.3}_{-0.3}$	124/93	$0.06^{+0.01}_{-0.01}$	$-0.9^{+0.7}_{-1.0}$	$41.57^{+0.07}_{-0.07}$
T4	2009-10-31	-	-	-	-	-	-	-	-	*42.56*
	2012-12-3	**51/41**	$0.08^{+0.04}_{-0.03}$	70/41	*0.0*	$5.2^{+0.2}_{-0.2}$	45/39	$0.08^{+0.04}_{-0.03}$	$1.0^{+0.6}_{-0.5}$	$43.16^{+0.04}_{-0.04}$

3.3.1 *Sources with a drop in flux above 2 keV*

By visual inspection of our sources, we found 2 showing an extremely soft spectrum mainly because of a steep drop in their flux above ~ 2 keV. In order to estimate the importance of the soft excess we compared the emission in the 0.5-2 keV and 2-10 keV bands. The emission in the hard band was calculated modelling the sole data above 2 keV with a power-law with photon index fixed to 1.9 and fixed galactic absorption; this is done in order to avoid that the fit in the hard band is dominated by the extrapolation of a power law component that is constrained only by soft data. Note that this differs from the best-fitting parameters reported in Table 3.3, but it is a better choice for isolating the contribution of the two spectral components. In both cases, the emission in the hard band is so faint that only upper limits were in fact retrieved. Figure 3.4 shows the comparison between these super-soft sources and standard (in terms of X-ray properties) PG quasars (Piconcelli et al., 2005). It is clear that the sources from our sample, have much larger soft excess than typical broad line quasars or, in other words, that they are extremely hard X-ray-weak sources, completely dominated by a thermal-like component.

[CRS2013] 4 This source, labelled D1, has a photometric redshift of $z = 0.115$ from the SDSS DR8 (Aihara et al., 2011) and no optical spectral information is available. Although this source is probably associated with the outskirt of the ACO 2443 cluster (Clarke et al., 2013), its X-ray spectrum strongly deviates from thermal plasma emission (e.g. the *apec* model in XSPEC). This source has been observed in three occasions: twice by Chandra, in 2010 and 2013 and once by XMM-Newton, in 2015. Its spectrum is best fitted by a blackbody with a temperature of about 150 eV and no extra-absorption nor power law component in the hard X-ray band. The source luminosity in the 0.5-2 keV range show significant variability on years timescales, passing from 6.5 to 2.5×10^{42} erg/s from the first to the second observation, while it remains constant from the second to the third. The soft X-ray emission of D1 is at least one order of magnitude larger than in PG quasars with respect to that expected from the hard X-ray luminosity upper limit of 3×10^{40} erg/s. Its X-ray spectrum is shown in Figure 3.5.

2XLSSd J021728.4-041346 This source , labelled D2, is located at $z = 1.173$ and catalogued as AGN by SED-fitting (Melnyk et al., 2013; Liu et al., 2016), as only photometric information is available. The source has five XMM observations, the first three were taken between the 8th and the 9th of January 2007 and are here merged together. The fourth observation was taken in July 2008, and the last has been taken in February 2015. The data of all observations were fitted jointly and the best fitting model is an extremely steep powerlaw with photon index $\Gamma = 5$ (or, almost equivalently, a blackbody with a temperature of about 140 eV). The X-ray

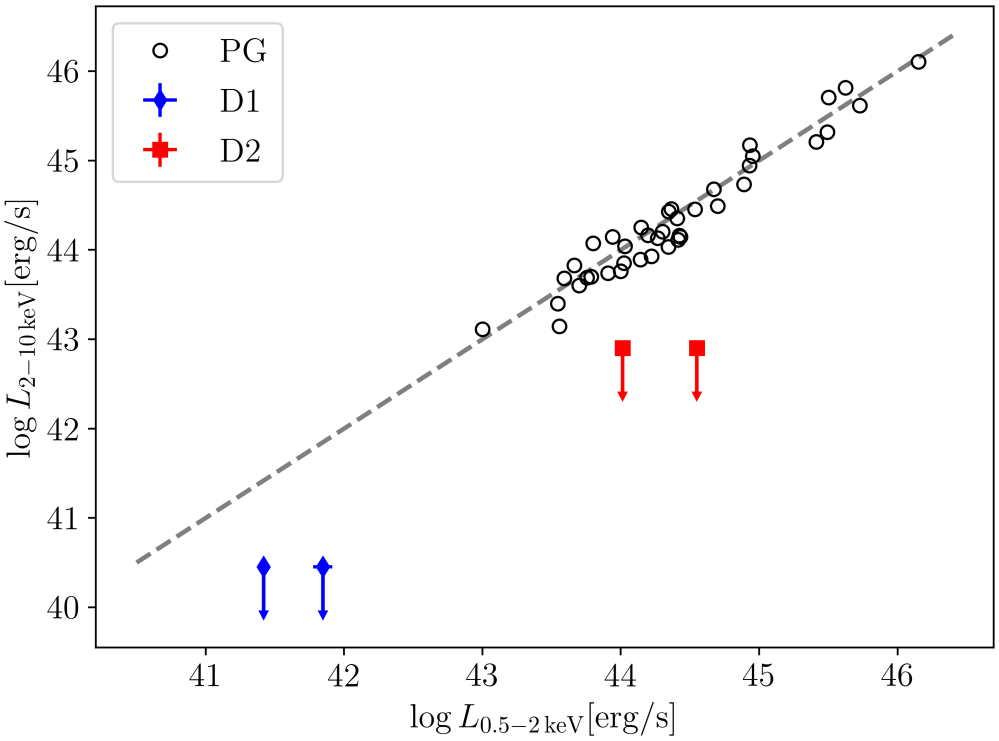

Figure 3.4: $L_{2\text{-}10\,\mathrm{keV}}$ *vs* $L_{0.5\text{-}2\,\mathrm{keV}}$ *for PG quasars population (black circles) and for our sources (colored markers). The dashed line is the bisectrix. There are only two points versus three spectra for both of our sources as data from different observations are fitted together unless statistically significant flux variations are present (see text for details). The hard band luminosities are upper limits.*

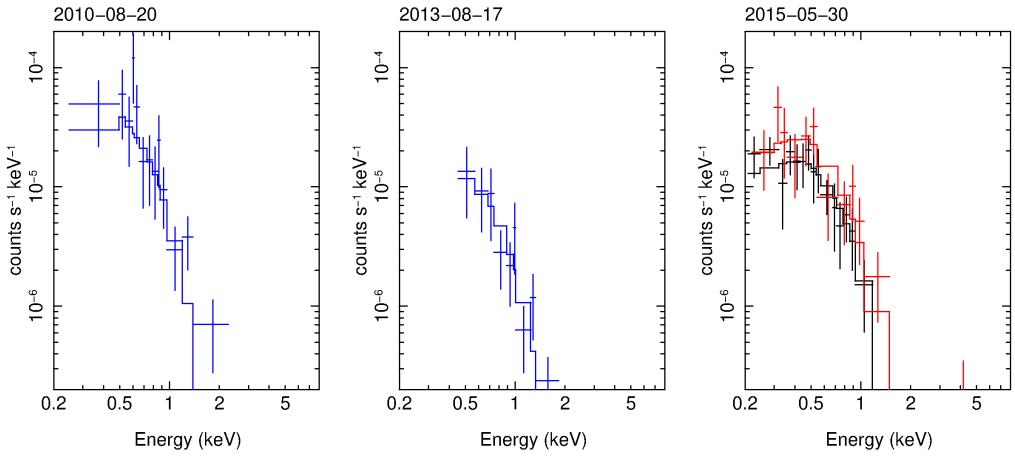

Figure 3.5: *X-ray spectrum of the source labelled D1. Blue data are from Chandra, black from the XMM-Newton EPIC-pn camera, and red from the EPIC-mos one. Solid lines show the best fitting model.*

luminosity in the 0.5-2 keV range of the source suffers a drop of almost a factor 3.5 from 4×10^{44} to 1.2×10^{44} erg/s between the first and last observation. In each observation the soft X-ray emission is more than one order of magnitude larger in comparison to the standard PG quasars given that its 2-10 keV emission lies below 8×10^{42} erg/s, as shown in Figure 3.4. The X-ray spectrum of the source is shown in Figure 3.6.

3.3.2 *Peculiar AGNs*

Three sources of our sample are optically classified as AGNs and are selected here because they exhibit a peculiar super-soft spectral component at least during one observation. As for the sources already presented, no clear short-term variability has been found in these sources.

[VV2006] J231419.8-525901 This source, labelled P1, is located at spectroscopic redshift $z = 0.15575$ (Jones et al., 2009) and classified as a Seyfert 1 galaxy (Véron-Cetty & Véron, 2006). It has been observed once by XMM-Newton and its spectrum is best fitted by a blackbody plus powerlaw model with no extra-absorption. The powerlaw is steep and mostly constrained by soft X-ray data below 2 keV, with a photon index $\Gamma > 2.6$. What makes this source really peculiar is the extremely cold blackbody of just $kT \sim 20$ eV dominating the ultrasoft X-ray band. Such a cold thermal-like component, detected in both the EPIC-pn and mos cameras, is unprecedented in the X-ray spectra of type 1 AGNs. The X-ray

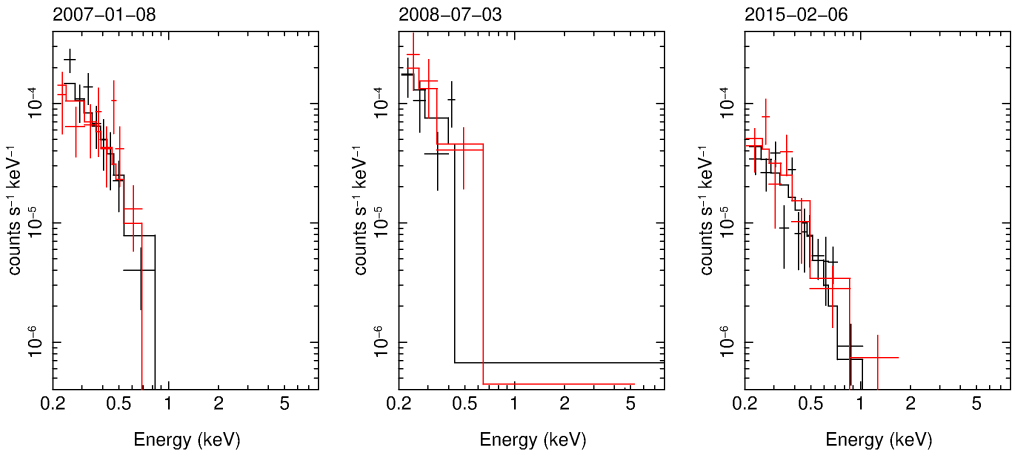

Figure 3.6: *X-ray spectrum of the source labelled D2. The color code is the same as in the previous plots. We only show the highest signal to noise observation of the three performed in July 2008.*

luminosity of P1 is about 6×10^{41} erg/s and the X-ray spectrum of the source is shown in Figure 3.7.

2XMM J122517.6+175726 This source, labelled P2, has a spectroscopic redshift $z = 0.8053$ and it is catalogued as a QSO (Pâris et al., 2014). It has been observed once in 2004 and then three times on December 2010. For the first observation we have data only from the EPIC-mos camera, while for the last three observations we have only EPIC-pn data. We analyzed the first observation separately while the last three were treated together as they were taken only few days apart from one other. On 2004, given the poor quality of the data, the source spectra is best fitted by simple model composed by a steep powerlaw ($\Gamma \sim 3$) with a drop in flux below $\sim$ 0.4 keV. We modelled this drop with extra-absorption at the source redshift which results into a column density of $2.7^{+1.8}_{-1.5} \times 10^{21}$ atoms/cm^2. The unabsorbed luminosity of the source in the first observation is about 6×10^{44} erg/s, consistent with the QSO classification. Remarkably, no extra-absorption is present during the 2010 observations, and the spectrum of the source is best fitted by a blackbody plus powerlaw model, being the temperature of the blackbody extremely low at $kT \sim 20$ eV, and the photon index of the powerlaw $\Gamma \sim 2$. The appearance of such a cold thermal-like component makes P2 a similar source to P1 in terms of spectral shape. The luminosity of the source on 2010 is about 1.5×10^{44} erg/s and show a small but statistically significant decrease between the first and last two observations. The X-ray spectrum of the 4 observations is shown in Figure 3.8.

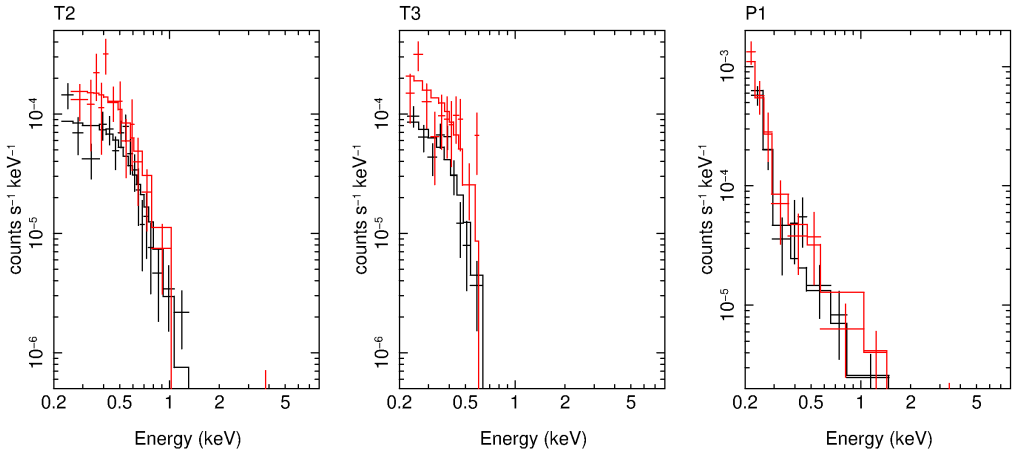

Figure 3.7: *X-ray spectrum of sources with a single observation. From left to right the spectra correspond to sources labelled T2, T3, P1. The color code is the same as in the previous plot.*

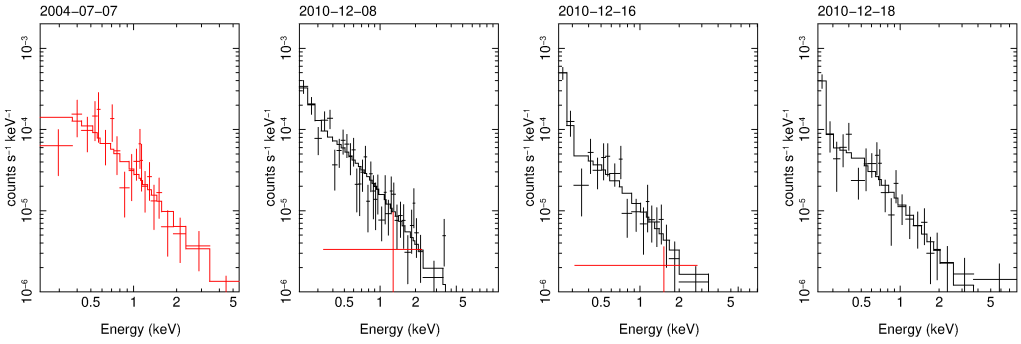

Figure 3.8: *X-ray spectrum of the source labelled P2. The color code is the same as in the previous plots.*

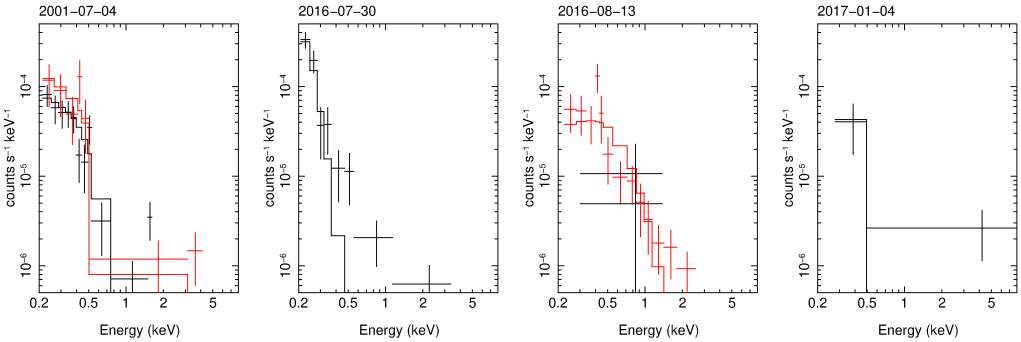

Figure 3.9: *X-ray spectrum of the source labelled P3. The color code is the same as in the previous plots.*

2XMM J022255.9-051352 This source, labelled P3, is catalogued as a Seyfert 1 galaxy (Véron-Cetty & Véron, 2010) and has a spectroscopic redshift $z = 0.846478$. The source was observed on four different occasions (once in 2001, two times in 2016 and one final time in 2017, although in this last observation the quality of the data is extremely poor) and its X-ray spectrum shows strong spectral variability associated with roughly constant luminosity. The best fitting model for this source is a blackbody with no extra-absorption. During the first 2016 observation, the spectrum is dominated by a cold blackbody emission with $kT \sim 40$ eV, while during the second (2 weeks later) the temperature is a much higher $kT \sim 240$ eV. In 2001 and 2017 (this last observation having much lower signal to noise), the blackbody temperature is instead $kT \sim 120$ eV. The X-ray spectrum of the source is shown in Figure 3.9.

3.3.3 *Candidate TDEs*

Four sources are consistent with being TDE candidates, although our tentative classification cannot be considered as unique. For two sources (T2 and T3) we only have a single XMM-Newton observation which prevents to study any long-term variation. However, their optical classification as inactive or star-forming galaxies associated with their supersoft X-ray spectral shape and relatively high luminosity make them promising TDE candidates. For two other sources instead (T1 and T4) we have multiple observations available. T4 is undetected during one first observations, and exhibits high luminosity and typical TDE spectral shape about 3 years later. Although these properties are fully consistent with an overlooked TDE, the source is classified as AGN in the optical, which may instead call for a AGN variability event. For T1 we have one archival observation and we asked for a new one. Ten years later its luminosity dropped by a factor ≈ 20 which, coupled with its spectral shape, strongly suggest a TDE nature for this transient.

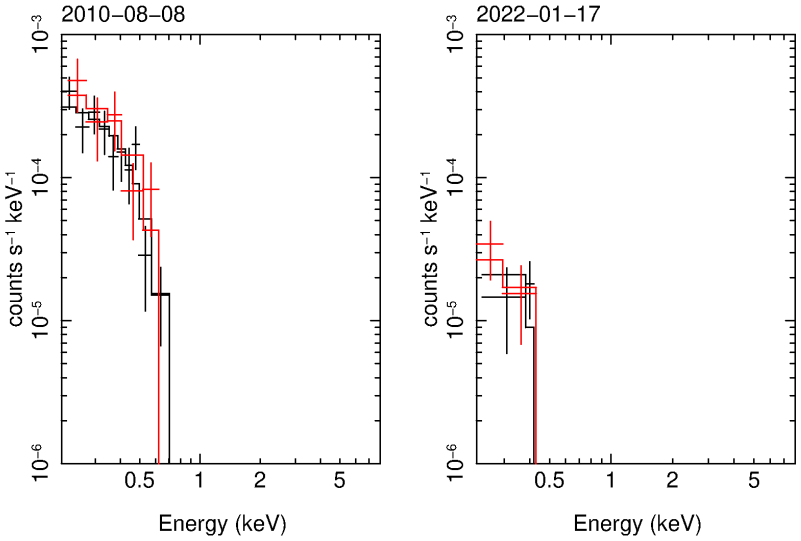

Figure 3.10: *X-ray spectrum of the source labelled T1. The color code is the same as in the previous plots.*

SDSS J152717.95+164503.2 This source, labelled T1, has a spectroscopic redshift $z = 0.0606$ coming from the SDSS DR9 (Ahn et al., 2012) and it is catalogued as a non-active, star-forming galaxy with a star-formation rate of $\log \mathrm{SFR} = -0.1192\, M_\odot/\mathrm{year}$ (Toba et al., 2014; Duarte Puertas et al., 2017). It has been observed in August 2010 and its X-ray spectrum is well modelled by a cold blackbody with $kT \sim 60$ eV and no extra-absorption. We compared this model with a thermal plasma model (*apec*) in order to be sure that the X-ray is not due to star-formation. The comparison has been done with the standard F-test, we found out that the blackbody model the data significantly better (F-test < 3 ‰). On 2010 the X-ray luminosity between 0.5 and 2 keV of the source is 10^{41} erg/s. We asked for a new observation with *XMM-Newton* and the sources was re-observed in January 2022 (Proposal ID: 088474, PI: A. Sacchi). After 12 years the spectral shape of the source is unchanged, strongly suggesting that we are still observing the source rather than the host galaxy emission, and its X-ray luminosity dropped by a factor ≈ 20. Its spectrum is shown in Figure 3.10.

2MASX J00414632-2827423 This source, labelled T2, is located at a spectroscopic redshift $z = 0.0744$ (Colless et al., 2001) and identified as a non-active galaxy (Paturel et al., 2003). It has one XMM-Newton observation in which the spectrum is well modelled by a blackbody with $kT = 0.11 \pm 0.01$ keV and its X-ray luminosity is about 2×10^{41} erg/s. Although the source is located in the far outskirt of the Sculptor cluster its X-ray emission appears to be associated with accretion

phenomena rather than with the diffuse cluster emission. In order to test this, we tried modelling the X-ray spectrum of the source with a thermal plasma emission model, but we found that a blackbody can fit significantly better the emission of this source (F-test < 2 ‰). The X-ray spectrum of the source is shown in Figure 3.7.

GAMA 91637 This source, labelled T3, has a spectroscopic redshift $z = 0.1775$ from the GAMA survey(Driver et al., 2011) and it is catalogued as a non-active galaxy (Liske et al., 2015). It has been observed only once by XMM-Newton and its X-ray spectrum is best fitted by a cold blackbody with no extra-absorption and $kT \sim 60$ eV. Again, we tested the blackbody model versus the thermal plasma model and found out that the former describes the data significantly better than the latter (F-test < 1 ‰). The X-ray luminosity for this source is $\sim 4 \times 10^{41}$ erg/s, and its X-ray spectrum is shown in Figure 3.7.

XXL-AAOmega J234255.95-543001.8 This source, labelled T4, has a spectroscopic redshift $z = 0.28633$ and it is catalogued as AGN due to the presence of broad emission lines in its optical spectrum (Pierre et al., 2016; Lidman et al., 2016). It falls in the field of view of XMM-Newton on two occasions, three years apart from one other, in October 2009 and December 2012. During the first observation the source was not detected and the upper-limit to its luminosity is $\sim 4 \times 10^{42}$ erg/s. Three years later the luminosity is almost an order of magnitude larger, $\sim 1.5 \times 10^{43}$ erg/s, and the X-ray spectrum of the source is well modelled by a blackbody with a temperature $kT \sim 80$ eV and no extra-absorption. These appear to be X-ray properties that are consistent with a TDE detected near the peak possibly occurring in a pre-existing faint AGN, or with an extreme variability event from an AGN. Follow-up observations of T4 may be used to obtain insights on its nature although after more than 10 years, in the standard TDE scenario its luminosity would have already dropped below the observational capabilities of today instruments for a standard duration observation. The X-ray spectrum of the source is shown in Figure 3.11.

3.4 - **Discussion**

We presented a sample of supersoft, luminous X-ray sources that are associated with the central regions of galaxies with the main goal of identifying a series of potentially interesting objects ranging from overlooked X-ray TDEs to supersoft AGN that often exhibit peculiar spectral and variability properties. Starting from the more than 5.5×10^5 sources of the latest XMM-Newton catalogue, we obtained a final sample of 60 sources sharing similar spectral features and X-ray luminosities

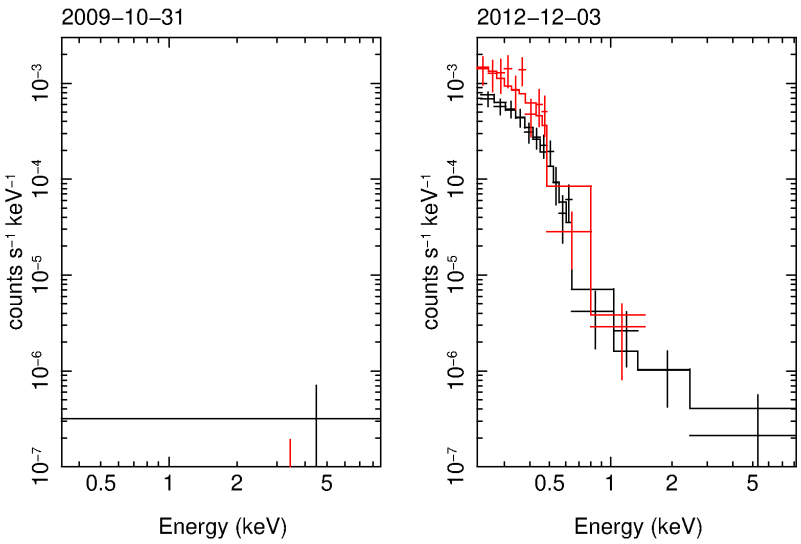

Figure 3.11: *X-ray spectrum of the source labelled T4. The color code is the same as in the previous plots. On the left the 2009 observation, which as one can see is a non-detection and the plot is shown only for comparison reasons.*

well above 10^{41} erg/s. Out of these 60 sources, 15 turned out to be well known TDEs, TDE candidates, or AGNs with extreme spectral/variability properties, confirming that our selection criteria indeed reveal the correct population of X-ray sources. By performing a complete X-ray spectral analysis of the remaining 45 sources, we identified 36 sources that are either standard type 1 AGNs (although somewhat softer-than-usual in the X-ray, or sources such as obscured AGNs and/or star-forming galaxies where the soft X-ray emission is dominated by extended emission. One source, 2dFGRS TGS431Z029 is somewhat peculiar as it exhibits an X-ray spectrum consistent with an heavily obscured AGN despite being classified as a non-active galaxy due to the lack of optical emission lines. The remaining 9 sources have spectral properties that most significantly deviate from the expected behavior based on optical classification and/or do not resemble those of standard AGNs. We focus our discussion on these 9 sources.

The X-ray spectrum of two sources (D1 and D2) is best described by a black-body model with temperature of 140-150 eV (or a steep power law with $\Gamma \sim 5$), rather typical of AGN soft excesses. However, their hard X-ray emission above 2 keV is much fainter than in standard AGNs as only upper limits could be derived on the 2-10 keV luminosity, making D1 and D2 two examples of hard X-ray weak sources (or extreme soft excess ones). Long-term variability suggests that their soft X-ray spectrum is not dominated by very extended emission nor star-formation and that the lack of hard X-ray is unlikely to be the signature of Compton-thick AGNs.

On the other hand, no short-term variability was found in the X-ray during any of the observations.

Although only photometric information is available for both D1 and D2, the latter is classified as AGN by SED-fitting, and its X-ray luminosity of a few times 10^{44} erg/s (about 2 orders of magnitude higher than in D1) is consistent with that classification, although such X-ray luminosity is also consistent with the early stages of TDEs evolution. As AGN, the X-ray spectrum of D2 is reminiscent of Narrow Line Seyfert 1 galaxies, often characterized by a prominent soft X-ray excess, and could then represent a particularly extreme version of standard BH accretion, most likely associated with high accretion rate. The same plausible interpretation applies to D1 as well. The possibility that D1 (and/or D2) is a TDE observed by chance relatively close to its X-ray peak appears unlikely because of the persistent X-ray emission with only limited dimming over the course of several years (about 5 and 8 years respectively), as well as because the inferred temperature of the best-fitting blackbody models is significantly higher than in most other X-ray TDEs. However, some cases of extremely long-lived TDE candidates characterized by higher-than-standard blackbody temperature exist (e.g. Lin et al. 2017b), so that a TDE origin for D1 (and/or D2) cannot be firmly ruled out. On the other hand, the X-ray spectrum of D1 is very similar to that of ULSs (cfr. with Figure 2 of Kaaret et al. 2017) where the dominant soft X-ray emission can be understood in terms of optically thick outflows blocking the hard X-ray and reprocessing them into a soft thermal component. The X-ray luminosity in excess of 10^{42} erg/s is much higher than that of typical ULSs and could suggest accretion onto an IMBH. Interestingly, the most convincing IMBH candidate to date, ESO 243-49 HLX-1 (Farrell et al., 2009), is both soft and bright enough to satisfy our search criteria, but was not selected here because of its off-center nature.

Three further sources are classified as peculiar AGNs (P1, P2, and P3). They are all spectroscopically classified as AGNs (2 Seyfert 1 galaxies, and 1 QSO), and what makes them special is the presence of at least one epoch in which an extremely soft X-ray component is observed in the spectrum. When modelled as a simple blackbody, we derive temperatures as low as 20 eV in P1 and P2, and 40 eV in P3 for this cold component. It should be pointed out that the cold component is only detected by the EPIC-pn camera in P2 and P3 as the MOS data were not available at that particular epoch. This could in principle signal that the very soft emission is in fact associated with calibration uncertainties of the EPIC-pn. However, both EPIC cameras are consistent with each other in the case of the only observation of P1 where a rather clear ~ 20 eV thermal component is present together with a steep power law.

P2 is the only source in our sample where cold X-ray absorption is detected (in excess of the Galactic one). This is, however, limited to one observation only. The cold component appears 6 years later and is associated with a completely

unabsorbed X-ray spectra, suggesting the possibility that it may have been present always, but masked by the absorption during the first observation. On the other hand, the cold component in P3 is transiently seen in one observation of a source that appears to vary wildly spectrally as the best-fitting temperature of simple blackbody models is seen to vary by more than a factor of 2 in about 15 years.

Finally, 4 sources out of the 9 selected have properties that make them plausible TDE candidates, although this tentative classification is far from being secure (or unique). Three of them (T1, T2, and T3) are spectroscopically classified as non-active galaxies and, in their available XMM-Newton observations, they exhibit a soft, thermal-like X-ray spectrum that is typical of X-ray TDEs observed close to their peak. When modeled as a blackbody, we derive temperatures of 60 to 110 eV, with luminosities in the range of 10^{41} erg/s to a few 10^{41} erg/s, rather typical for TDEs. The addition of a hard power law component did not improve the spectral description in any case. This is consistent with TDE X-ray spectral properties, especially during the early stages (Saxton et al., 2021). As only one observation is available for T2 and T3 (we also checked for archival observations of other instruments such as *Swift* and *ROSAT* but only upper limits above some 10^{43} erg/s were available), long-term variability cannot be used to support the TDE classification, but the non-active nature of the host galaxies coupled with the the relatively high X-ray luminosities and spectral shape is highly suggestive. As already discussed for D1, these two sources may be instead associated with the very high luminosity end of the ULS population. If so, they would be potential IMBH candidates that escaped detection so far because searches for ULXs have always concentrated on off-center sources to avoid confusion with AGNs.

For the source we labelled T1 we asked for a follow-up observation in order to confirm its nature. We obtained it and in January 2022 it has been observed for ≈ 45 ks. In its second observation while its spectrum kept roughly the same shape, its luminosity decreased by a factor ≈ 20. This strongly supports the hypothesis of a TDE nature for this source although the modest decrease is not completely in accord with a "standard" TDE and would rather place this source amongst the long-lived TDEs (Lin et al., 2017a).

The fourth source that we suggest as a possible TDE candidate (T4) is classified as AGN, due to the presence of broad emission lines in the optical spectrum. T4 has been observed twice by XMM-Newton. It was not detected during the first pointing while it exhibits a rather typical TDE X-ray spectrum in the second one performed about 3 years later. When detected, the X-ray spectrum is best modelled by a blackbody with temperature of 80 eV and a rather high luminosity exceeding 10^{43} erg/s in the soft 0.5-2 keV band. Based on the optical classification and X-ray properties, the most appealing interpretation for the behaviour of T4 is that of a TDE occurring in a pre-existing AGN. On the other hand, as the upper limit during the first observation is not tight, we cannot firmly exclude that T4 is an AGN with

very weak 2-10 keV emission (if any) and highly variable, particularly cold soft X-ray excess.

The presence in our initial sample, comprising 60 sources, of 9 well known TDEs or strong TDE candidates supports our ability of detecting them quite efficiently. In fact, this is the lower limit of our efficiency: our algorithm selected 3 more TDEs, OGLE16aaa (Zhang et al., 2016), 3XMM J152130.7+074916 (Lin et al., 2015) and 2XMMi J1847 (Lin et al., 2011), which satisfy our criterion but unfortunately are not associated with their host galaxy redshift in optical catalogs; other 2 TDEs instead, [GHC2009] D23H-1 (Gezari et al., 2009) and PS1-13jw (Kankare et al., 2017), were not selected because their X-ray signal to noise ratio is below the chosen threshold.

Assuming that the 4 sources discussed above (T1-T4) are indeed associated with TDEs, we can attempt a rough estimate of the TDE rate and check its consistency with other results in the literature obtained with different methods. From our data, we retrieve (see next section for details) a rate of $(2.4 \pm 0.2) \times 10^{-5}$ gal^{-1} yr^{-1} which falls below the typical value of 10^{-4} gal^{-1} yr^{-1} obtained by theoretical arguments (see Stone et al. 2020 for a recent review on the subject). Our estimate is nonetheless fully consistent with the TDE rates deduced from X-ray data, which span a $12 - 0.9 \times 10^{-5}$ gal^{-1} yr^{-1} range (Donley et al., 2002; Esquej et al., 2008; Khabibullin et al., 2014).

3.5 - **Calculation of TDE rate**

In order to give an estimate of the rate of TDEs based on the 4 we found with our methods, we firstly need to estimate in how many galaxies we would have been able to identify one if it occurred. To do so we started by retrieving the list of XMM-Newton pointings, along with the duration of each observation. Then we cross-matched the list with the four aforementioned galaxy catalogs paying attention not to double-count the galaxies that were included in more than one catalog. We selected all of the galaxies within a radius of 14 arcmin from the XMM pointing in order to account for the XMM field of view.

For each galaxy we then computed the minimum observable flux. We did so by taking the exposure time, decreasing it by a 30% in order to account for the background flaring, computing the correspondent 7σ sensitivity (adapting the 5σ sensitivity from Watson et al. 2001) and finally multiplying for the vignetting factor taken from Fig. 13 of the "XMM-Newton Users Handbook", Issue 2.17, 2019 (ESA: XMM-Newton SOC). Finally for each galaxy we converted the minimum observable flux in a luminosity threshold ($L_{\rm th}$).

As in looking for super-soft hyper-luminous sources we selected only sources with luminosity higher than a chosen threshold (10^{41} erg/s) we now face a double

problem: as the lightcurves of TDEs decrease with time, if the luminosity threshold of a galaxy is larger then 10^{41} erg/s, we would catch a TDE exploding in it only in the fraction of its lifetime its luminosity is larger then the galaxy luminosity threshold; furthermore, after enough time passed we would not be able to catch it in any galaxies at all. Each galaxy was then counted, weighted with weight w computed as follows:

$$\begin{cases} w = 1 & \text{if } L_{\text{th}} < 10^{41}\,\text{erg/s} \\ w = \left(\frac{L_{\text{th}}}{10^{41}\,\text{erg/s}}\right)^{1/k} & \text{if } L_{\text{th}} > 10^{41}\,\text{erg/s} \end{cases} . \tag{3.1}$$

The last expression equals the fraction of time it takes a TDE with lightcurve slope k to decrees from its peak luminosity to L_{th} with respect to decreasing to 10^{41} erg/s. Assuming a classical $-5/3$ value for the value of the lightcurve slope, the number of galaxies in which we would have observed a TDE is 55498. Given that we could not keep under control every source of uncertainty, we approximate this number to 55000 and assume a conservative error of 10% on said value.

Finally we need to assume a value for the visibility window of TDEs i.e. the amount of time a TDE has luminosity larger than our search threshold of 10^{41} erg/s; in this case we chose a 6 years period. This choice also roughly corresponds to the amount of time a TDE at $z = 0.1$, with luminosity peak of 10^{44} erg/s, following a $t^{-5/3}$ light-curve with a characteristic time of one month, would remain detectable by XMM-Newton with a 7σ sensitivity. This gives us a rate of $(1.2 \pm 0.2) \times 10^{-5}$ TDEs per galaxy per year. This rate refers only to TDEs presenting a supersoft X-ray emission (thermal TDEs), we can correct for this effect by dividing our estimated rate by the fraction of thermal TDEs in the XMM-Newton catalog which amounts to roughly $1/2$ retrieving a final estimate for the TDEs rate of $(2.4 \pm 0.2) \times 10^{-5}$ gal^{-1} yr^{-1}.

3.6 - **Conclusions**

In this Chapter we described the selection and properties of a sample of X-ray super-soft ($\Gamma > 3$), hyper-luminous ($L > 10^{41}$ erg/s) X-ray sources in the nuclear region of external galaxies by cross-matching the latest releases of XMM-Newton and optical catalogs of galaxies.

Our work resulted in the selection of 60 sources, 15 of which turned out to be known examples of the type of sources we are searching for in our study: TDEs, TDE candidates or super-soft AGNs with often extreme X-ray properties. Of the remaining 45 sources, 36 were considered standard AGN and/or star-forming regions based on their X-ray spectral properties, while 9 have been selected as further examples of potentially interesting super-soft and X-ray luminous nuclear sources.

We discuss their X-ray properties in some detail, showing that while some sources may be examples of exceptionally soft-excess dominated (but otherwise standard) AGNs, others may be instead associated to overlooked TDEs that have not being followed-up or to super-soft ULXs that, given the high observed X-ray luminosities, may be associated with nuclear IMBHs. From the 4 TDE candidates that we tentatively identify, we derive a rough TDE rate estimate of $\sim 2.4 \times 10^{-5}$ TDEs per galaxy per year, consistent with other estimates from X-ray data.

We encourage multi-wavelength studies and follow-up observations of these sources that will help clarifying their nature.

Table 3.4: *Spectral parameters of the source we found to be "standard" AGN. The model employed is an absorbed blackbody+powerlaw (*zTbabs $\times$ (zBbody + zPowerlw) *in XSPEC). Quantities in italic are fixed during the fitting procedure. The luminosity is computed between 0.5 and 2 keV.*

ID (SIMBAD)	date	C/ν	$N_{\rm H}$ (10^{22} atoms/cm^2)	T (keV)	Γ	$\log_{10} L$ (erg/s)
NGC 6264	2005-8-12	9/10	*0.0*	$0.14^{+0.03}_{-0.02}$	-	$41.41^{+0.2}_{-0.29}$
	2010-8-26	213/190	*0.0*	$0.14^{+0.01}_{-0.01}$	$2.4^{+0.3}_{-0.3}$	$41.19^{+0.08}_{-0.07}$
	2012-2-19	73/81	*0.0*	$0.15^{+0.02}_{-0.02}$	*3.0*	$40.97^{+0.06}_{-0.06}$
2dFGRS TGS431Z029	2003-09-06	17/31	*0.0*	$0.17^{+0.06}_{-0.05}$	*-2*	$40.58^{+0.24}_{-0.24}$
	2012-05-14	60/79	*0.0*	$0.16^{+0.02}_{-0.02}$	$-1.0^{+0.9}_{-1.1}$	$40.31^{+0.08}_{-0.09}$
	2013-11-25	136/118	*0.0*	$0.16^{+0.01}_{-0.01}$	$-2.2^{+0.5}_{-0.6}$	$40.39^{+0.05}_{-0.05}$
	2016-05-20	141/129	*0.0*	$0.11^{+0.02}_{-0.01}$	*-2.0*	$40.14^{+0.09}_{-0.1}$
	2017-05-20	137/121	*0.0*	$0.14^{+0.01}_{-0.01}$	$-1.9^{+0.6}_{-0.7}$	$40.28^{+0.06}_{-0.06}$
	2017-11-25	195/129	*0.0*	$0.14^{+0.01}_{-0.01}$	*-2.0*	$40.31^{+0.05}_{-0.05}$
	2019-11-22	126/124	*0.0*	$0.16^{+0.01}_{-0.01}$	*-2.0*	$40.44^{+0.05}_{-0.05}$
2MASX J10181928+3722419	2007-5-18	123/80	*0.0*	$0.11^{+0.01}_{-0.01}$	$0.9^{+0.5}_{-0.5}$	$40.84^{+0.06}_{-0.06}$
2dFGRS TGS243Z047	2018-07-28	103/81	*0.0*	$0.19^{+0.03}_{-0.03}$	$-0.5^{+0.9}_{-1.5}$	$41.15^{+0.07}_{-0.08}$
	2018-08-12	150/119	*0.0*	$0.16^{+0.01}_{-0.01}$	$-0.7^{+0.5}_{-0.5}$	$41.21^{+0.04}_{-0.04}$
	2018-08-20	105/125	*0.0*	$0.12^{+0.02}_{-0.02}$	$0.8^{+0.6}_{-0.5}$	$41.17^{+0.06}_{-0.07}$
	2019-02-09	77/77	*0.0*	$0.15^{+0.01}_{-0.01}$	*-2.0*	$41.16^{+0.07}_{-0.07}$

Table 3.4: *Continued.*

ID (SIMBAD)	date	C/ν	$N_{\rm H}$ (10^{22} atoms/cm^2)	T (keV)	Γ	$\log_{10} L$ (erg/s)
2MASX J17020882+6412210	2000-10-31	21/29	*0.0*	*0.12*	$3.1^{+0.4}_{-0.4}$	$40.98^{+0.54}_{-0.16}$
	2002-5-31	76/77	*0.0*	$0.18^{+0.05}_{-0.05}$	-	$41.32^{+0.13}_{-0.19}$
	2007-11-14	31/24	*0.0*	$0.41^{+0.15}_{-0.15}$	-	$41.29^{+0.14}_{-0.14}$
	2013-5-19	27/26	*0.0*	$0.24^{+0.06}_{-0.05}$	-	$41.22^{+0.42}_{-0.12}$
	2013-7-9	81/50	*0.0*	$0.16^{+0.02}_{-0.02}$	$-0.2^{+0.7}_{-0.7}$	$40.82^{+0.08}_{-0.08}$
	2013-8-4	30/31	$0.22^{+0.44}_{-0.22}$	$0.11^{+0.06}_{-0.04}$	-	$41.51^{+0.43}_{-0.63}$
3XMM J172037.1+574855	2009-8-28	147/122	*0.0*	$0.13^{+0.01}_{-0.01}$	$0.6^{+0.3}_{-0.3}$	$41.95^{+0.04}_{-0.04}$
	2015-3-28	103/81	*0.0*	$0.12^{+0.01}_{-0.01}$	$-0.1^{+0.3}_{-0.3}$	$42.08^{+0.03}_{-0.03}$
	2015-6-15	326/207	$0.02^{+0.02}_{-0.02}$	$0.09^{+0.0}_{-0.0}$	$0.5^{+0.1}_{-0.1}$	$42.45^{+0.05}_{-0.04}$
	2015-9-3	210/128	*0.0*	$0.1^{+0.0}_{-0.0}$	$0.6^{+0.1}_{-0.1}$	$42.48^{+0.01}_{-0.01}$
2E 2922	2011-1-22	240/165	*0.0*	$0.11^{+0.0}_{-0.0}$	$2.1^{+0.2}_{-0.2}$	$43.12^{+0.01}_{-0.01}$
3XLSSJ232605.5-540559	2008-4-17	164/169	*0.0*	$0.13^{+0.01}_{-0.01}$	$2.8^{+0.1}_{-0.1}$	$43.8^{+0.01}_{-0.01}$
	2012-11-25	106/89	*0.0*	$0.11^{+0.01}_{-0.01}$	$1.9^{+0.5}_{-0.4}$	$42.93^{+0.03}_{-0.04}$
2XMM J033742.8-252209	2001-8-18	108/117	*0.0*	$0.14^{+0.01}_{-0.01}$	$-0.1^{+0.4}_{-0.4}$	$42.33^{+0.05}_{-0.05}$
[VV2010c] J010006.9-001535	2014-7-4	26/36	*0.0*	$0.09^{+0.01}_{-0.01}$	$1.1^{+0.3}_{-0.3}$	$42.69^{+0.06}_{-0.06}$
SDSS J141308.12+515210.5	2017-5-11	56/63	*0.0*	*0.12*	$2.3^{+0.5}_{-0.7}$	$43.16^{+0.04}_{-0.04}$
3XLSS J231800.4-534901	2009-12-5	83/62	*0.0*	$0.19^{+0.02}_{-0.02}$	$1.4^{+1.2}_{-0.8}$	$43.45^{+0.05}_{-0.05}$
	2012-10-27	159/119	*0.0*	$0.1^{+0.02}_{-0.02}$	$2.2^{+0.2}_{-0.2}$	$43.36^{+0.03}_{-0.03}$
2XMM J021938.5-032507	2007-1-11	28/38	$0.5^{+0.5}_{-0.3}$	$0.05^{+0.01}_{-0.01}$	$2.8^{+1.1}_{-0.7}$	$45.06^{+1.6}_{-0.94}$
	2009-1-3	31/31	$0.9^{+0.9}_{-0.3}$	$0.05^{+0.02}_{-0.01}$	$2.8^{+2.2}_{-1.3}$	$45.3^{+2.5}_{-1.3}$
RX J1119.7+5951	2007-5-20	37/35	*0.0*	$0.13^{+0.02}_{-0.02}$	$1.5^{+1.0}_{-0.9}$	$44.26^{+0.06}_{-0.06}$
	2017-8-12	38/33	*0.0*	$0.01^{+0.01}_{-0.01}$	$2.7^{+0.2}_{-0.2}$	$43.94^{+0.07}_{-0.07}$
2XMM J021704.5-050214	2000-7-31	95/109	*0.0*	$0.2^{+0.04}_{-0.03}$	$3.1^{+3.2}_{-1.6}$	$43.19^{+0.05}_{-0.06}$

Table 3.4: *Continued.*

ID (SIMBAD)	date	C/ν	$N_{\rm H}$ (10^{22} atoms/cm^2)	T (keV)	Γ	$\log_{10} L$ (erg/s)
	2000-8-2	83/114	*0.0*	*0.12*	$2.4^{+0.4}_{-0.3}$	$43.22^{+0.04}_{-0.05}$
	2002-8-12	197/157	*0.0*	$0.17^{+0.01}_{-0.01}$	$2.2^{+0.2}_{-0.2}$	$43.81^{+0.02}_{-0.02}$
	2015-7-5	22/31	*0.0*	*0.12*	$2.1^{+0.5}_{-0.4}$	$42.99^{+0.18}_{-0.18}$
	2015-9-18	41/57	*0.0*	$0.43^{+0.09}_{-0.06}$	$1.7^{+0.9}_{-1.7}$	$42.84^{+0.1}_{-0.09}$
2XMM J120650.1+442353	2003-6-11	71/70	*0.0*	$0.11^{+0.02}_{-0.02}$	$1.0^{+0.3}_{-0.3}$	$42.86^{+0.1}_{-0.11}$
	2001-7-27	109/92	*0.0*	$0.08^{+0.02}_{-0.02}$	$1.4^{+0.3}_{-0.3}$	$42.99^{+0.07}_{-0.08}$
	2002-1-13	103/96	*0.0*	$0.1^{+0.02}_{-0.02}$	$2.4^{+0.4}_{-0.4}$	$43.26^{+0.04}_{-0.04}$
	2002-1-14	78/90	*0.0*	$0.08^{+0.01}_{-0.01}$	$0.8^{+0.7}_{-0.6}$	$42.84^{+0.05}_{-0.06}$
	2002-1-16	131/129	*0.0*	$0.11^{+0.01}_{-0.01}$	$1.7^{+0.3}_{-0.3}$	$43.38^{+0.03}_{-0.03}$
	2002-1-17	16/36	*0.0*	$0.06^{+0.02}_{-0.01}$	$1.3^{+0.6}_{-0.6}$	$42.93^{+0.14}_{-0.16}$
2XMM J033227.1-280124	2002-1-23	110/85	*0.0*	$0.22^{+0.02}_{-0.02}$	-	$42.94^{+0.07}_{-0.08}$
	2004-11-17	257/173	*0.0*	$0.59^{+0.04}_{-0.05}$	-	$43.37^{+0.05}_{-0.05}$
	2009-1-12	103/89	*0.0*	$0.11^{+0.02}_{-0.02}$	$2.0^{+0.4}_{-0.3}$	$42.98^{+0.03}_{-0.03}$
	2010-1-26	139/154	*0.0*	$0.09^{+0.02}_{-0.02}$	$1.7^{+0.3}_{-0.3}$	$42.82^{+0.04}_{-0.05}$
	2018-8-12	95/80	*0.0*	$0.04^{+0.02}_{-0.02}$	$1.9^{+0.3}_{-0.3}$	$42.91^{+0.07}_{-0.08}$
	2019-8-6	39/37	*0.0*	$0.12^{+0.04}_{-0.03}$	$0.3^{+1.0}_{-2.7}$	$42.66^{+0.12}_{-0.15}$

Table 3.4: *Continued.*

ID (SIMBAD)	date	C/ν	$N_{\rm H}$ (10^{22} atoms/cm^2)	T (keV)	Γ	$\log_{10} L$ (erg/s)
3XMM J022131.9-053853	2003-7-24	5/5	*0.0*	$0.08^{+0.02}_{-0.02}$	$0.4^{+1.6}_{-2.1}$	$44.24^{+0.13}_{-0.14}$
	2006-7-6	51/50	*0.0*	$0.11^{+0.01}_{-0.01}$	$0.9^{+0.4}_{-0.5}$	$44.03^{+0.06}_{-0.06}$
	2006-7-14	35/33	*0.0*	$0.09^{+0.02}_{-0.01}$	$0.6^{+0.6}_{-0.5}$	$43.83^{+0.19}_{-0.23}$
	2009-1-1	86/55	*0.0*	$0.15^{+0.01}_{-0.01}$	$2.2^{+0.6}_{-0.6}$	$44.02^{+0.05}_{-0.05}$
	2016-1-8	8/13	*0.0*	$0.15^{+0.03}_{-0.03}$	-	$43.88^{+0.08}_{-0.09}$
SDSS J022041.63-032700.4	2002-8-15	68/74	$0.1^{+0.31}_{-0.1}$	$0.15^{+0.04}_{-0.05}$	$2.1^{+0.6}_{-0.5}$	$43.47^{+0.05}_{-0.06}$
3XMM J115546.6+232446	2000-6-23	4/4	*0.0*	*0.12*	-	$44.09^{+0.19}_{-0.22}$
	2000-12-6	33/31	*0.0*	*0.12*	$2.1^{+0.7}_{-0.6}$	$43.77^{+0.08}_{-0.1}$
	2004-3-6	134/109	*0.0*	$0.12^{+0.04}_{-0.04}$	$1.9^{+0.2}_{-0.2}$	$43.46^{+0.06}_{-0.06}$
	2007-7-10	1/1	*0.0*	*0.12*	-	$43.88^{+0.26}_{-0.37}$
	2007-11-26	75/76	*0.0*	$0.11^{+0.01}_{-0.01}$	$2.0^{+0.3}_{-0.3}$	$43.8^{+0.02}_{-0.02}$
	2007-12-12	174/151	*0.0*	$0.11^{+0.01}_{-0.01}$	$2.2^{+0.3}_{-0.2}$	$43.65^{+0.02}_{-0.02}$
	2008-12-5	256/214	*0.0*	$0.1^{+0.01}_{-0.01}$	$2.4^{+0.1}_{-0.1}$	$44.31^{+0.01}_{-0.01}$
	2008-12-7	232/193	*0.0*	$0.1^{+0.01}_{-0.01}$	$2.3^{+0.1}_{-0.1}$	$44.03^{+0.02}_{-0.02}$
[VV2000] J110838.3+255522	2017-5-30	135/113	*0.0*	$0.12^{+0.01}_{-0.01}$	$1.0^{+0.3}_{-0.3}$	$44.29^{+0.02}_{-0.02}$
[VV2006] J120644.1+495337	2017-11-21	122/96	$0.49^{+0.24}_{-0.23}$	$0.08^{+0.02}_{-0.01}$	$2.3^{+0.3}_{-0.3}$	$44.56^{+0.02}_{-0.02}$
2SLAQ J011935.29-002033.5	2014-7-20	22/33	*0.0*	$0.12^{+0.02}_{-0.01}$	$1.9^{+0.7}_{-0.7}$	$44.12^{+0.07}_{-0.08}$
SDSS J125749.86+473958.9	2007-5-24	178/91	*0.0*	$0.11^{+0.02}_{-0.02}$	$1.9^{+0.5}_{-0.4}$	$43.49^{+0.07}_{-0.07}$
	2007-5-26	45/51	*0.0*	$0.14^{+0.01}_{-0.01}$	$1.9^{+2.6}_{-1.5}$	$43.72^{+0.08}_{-0.09}$
	2008-12-18	45/43	*0.0*	$0.11^{+0.03}_{-0.02}$	$1.6^{+0.8}_{-0.8}$	$43.18^{+0.14}_{-0.16}$
[VV2006] J090840.2+394415	2006-10-31	141/101	*0.0*	$0.1^{+0.02}_{-0.01}$	$1.1^{+0.3}_{-0.3}$	$43.32^{+0.1}_{-0.12}$
SDSS J022048.82-040819.5	2003-1-25	20/26	*0.0*	*0.12*	$3.2^{+1.2}_{-0.9}$	$44.08^{+0.21}_{-0.26}$
	2016-7-5	54/72	*0.0*	$0.03^{+0.11}_{-0.01}$	$2.6^{+0.2}_{-0.1}$	$43.77^{+0.07}_{-0.07}$

Table 3.4: *Continued.*

ID (SIMBAD)	date	C/ν	$N_{\rm H}$ (10^{22} atoms/cm^2)	T (keV)	Γ	$\log_{10} L$ (erg/s)
	2016-7-7	27/29	*0.0*	$0.18^{+0.07}_{-0.05}$	-	$43.78^{+0.13}_{-0.14}$
LAMOST J094241.69+464033.1	2010-4-17	148/150	*0.0*	$0.11^{+0.02}_{-0.02}$	$2.1^{+0.4}_{-0.4}$	$44.28^{+0.05}_{-0.05}$
[VV2006] J033226.5-274036	2001-7-27	262/155	*0.0*	$0.06^{+0.02}_{-0.02}$	$2.7^{+0.1}_{-0.1}$	$44.57^{+0.02}_{-0.02}$
	2002-1-13	204/149	*0.0*	$0.13^{+0.01}_{-0.01}$	$2.2^{+0.1}_{-0.1}$	$44.5^{+0.02}_{-0.02}$
	2002-1-23	357/166	*0.0*	$0.11^{+0.01}_{-0.02}$	$2.5^{+0.1}_{-0.1}$	$44.6^{+0.01}_{-0.01}$
	2010-1-26	232/199	*0.0*	$0.16^{+0.01}_{-0.01}$	$2.0^{+0.2}_{-0.2}$	$44.23^{+0.02}_{-0.02}$
2XMM J032159.8-370509	2001-4-17	112/95	*0.0*	$0.58^{+0.16}_{-0.07}$	-	$44.44^{+0.08}_{-0.08}$
	2005-8-11	138/191	$0.46^{+0.2}_{-0.24}$	$0.08^{+0.02}_{-0.01}$	$2.8^{+0.3}_{-0.3}$	$45.56^{+0.55}_{-0.61}$
	2007-8-19	128/141	*0.0*	$0.1^{+0.01}_{-0.01}$	$1.5^{+0.3}_{-0.3}$	$44.1^{+0.06}_{-0.06}$
	2009-6-25	139/152	*0.0*	$0.15^{+0.11}_{-0.06}$	$1.2^{+0.5}_{-0.5}$	$42.77^{+0.16}_{-0.2}$
	2019-4-20	15/15	*0.0*	-	$1.3^{+1.1}_{-1.0}$	$43.61^{+0.61}_{-0.64}$
3XMM J161212.5+540936	2002-9-12	109/79	*0.0*	$0.23^{+0.03}_{-0.04}$	$1.3^{+0.5}_{-0.5}$	$44.73^{+0.05}_{-0.05}$
	2002-9-14	93/72	*0.0*	$0.14^{+0.04}_{-0.04}$	$1.9^{+0.3}_{-0.3}$	$44.69^{+0.06}_{-0.06}$
	2002-9-18	92/110	*0.0*	$0.07^{+0.05}_{-0.04}$	$1.8^{+0.1}_{-0.2}$	$44.53^{+0.06}_{-0.06}$
	2005-12-7	32/26	*0.0*	$1.08^{+0.16}_{-0.13}$	-	$44.5^{+0.17}_{-0.17}$
	2006-3-8	44/38	*0.0*	$0.68^{+0.17}_{-0.1}$	-	$44.83^{+0.15}_{-0.15}$

Table 3.4: *Continued.*

ID (SIMBAD)	date	C/ν	$N_{\rm H}$ (10^{22} atoms/cm^2)	T (keV)	Γ	$\log_{10} L$ (erg/s)
2XMM J090927.7+542128	2001-4-29	137/111	*0.0*	$0.13^{+0.07}_{-0.06}$	$2.0^{+0.2}_{-0.2}$	$44.05^{+0.08}_{-0.08}$
	2005-3-28	56/55	*0.0*	$0.13^{+0.01}_{-0.01}$	$1.9^{+0.4}_{-0.4}$	$44.15^{+0.06}_{-0.06}$
[VV2006] J133944.5-001452	2005-1-12	28/42	*0.0*	$0.05^{+0.03}_{-0.02}$	$2.4^{+0.5}_{-0.6}$	$45.14^{+0.22}_{-0.22}$
	2005-7-17	62/60	*0.0*	$0.17^{+0.01}_{-0.01}$	$1.2^{+0.3}_{-0.2}$	$44.77^{+0.07}_{-0.07}$
[VV2006] J124049.1-015524	2006-1-7	65/74	*0.0*	$0.09^{+0.03}_{-0.03}$	$3.3^{+0.5}_{-0.6}$	$44.56^{+0.05}_{-0.05}$
	2017-12-14	43/54	*0.0*	*0.12*	$2.1^{+0.7}_{-0.7}$	$43.9^{+0.18}_{-0.22}$
2XMM J120947.8+393042	2000-12-22	102/73	*0.0*	$0.12^{+0.01}_{-0.01}$	$1.7^{+0.3}_{-0.3}$	$44.23^{+0.12}_{-0.11}$
XXL-AAOmega J231814.50-544112.3	2007-10-27	74/86	*0.0*	$0.39^{+0.07}_{-0.06}$	$1.4^{+0.5}_{-0.6}$	$44.18^{+0.08}_{-0.09}$
	2009-12-5	26/37	*0.0*	$0.42^{+0.15}_{-0.1}$	-	$44.23^{+0.19}_{-0.26}$
	2012-12-7	42/49	*0.0*	$0.83^{+0.13}_{-0.12}$	-	$43.82^{+0.11}_{-0.11}$
3XMM J022208.0-042734	2002-1-31	201/95	*0.0*	$0.85^{+0.07}_{-0.07}$	-	$44.49^{+0.09}_{-0.09}$
	2002-8-14	26/37	*0.0*	*0.12*	$2.2^{+0.2}_{-0.2}$	$45.02^{+0.11}_{-0.11}$
	2016-7-7	63/89	*0.0*	$0.15^{+0.06}_{-0.05}$	$1.7^{+0.2}_{-0.2}$	$44.6^{+0.07}_{-0.07}$
	2016-7-29	137/119	$0.19^{+0.44}_{-0.19}$	$0.08^{+0.04}_{-0.03}$	$2.2^{+0.3}_{-0.2}$	$44.74^{+0.04}_{-0.04}$

4 eROSITA cosmological quasars

Quasars are extremely powerful and stable sources which allows to extend the knowledge of the Hubble diagram up to redshift $z > 7$. Although these sources are not straight forward standard candles, they can nonetheless be standardized thanks to the non-linear relation which holds between their UV/optical and X-ray luminosities.

In this Chapter we aim to enlarge the sample of cosmological quasars. In previous works we obtained excellent results with a sample of ≈2500 sources. Here we more than double the dimension of the sample increasing our statistics at all redshift. This allows also to study possible dependencies of the relation of crucial aspects such as the X-ray photon index and the instruments employed.

We improved our statistics by adopting as parent sample the cross-match of the latest release of the XMM-Newton and Chandra X-ray catalogs with the MILLIQUAS (Million Quasars catalog) as well as the AGN catalog of the early data release of eROSITA.

Through our greatly improved statistics (by a factor 2 with respect to previous works) we once more confirm the non-evolution of the parameters of the relation with the redshift as well as its independence on the X-ray photon index and the chosen X-ray instruments.

This is furthermore proved by the fact that our cosmographic fits are in sticking agreement with the ones obtained in previous works.

4.1 - Introduction

Quasars are extremely powerful and stable astrophysical sources known up to $z = 7.5$ (Mortlock et al., 2011; Bañados et al., 2017; Wang et al., 2021), this would in principle make perfect standard candles of them. Indeed there have been several attempts in this direction, however, unfortunately they all have failed (to date). This is because the suggested methods either rely on precise distance measurements but are applicable to too few objects (Wang et al., 2013; La Franca et al., 2014) or have high statistic sample but are affected by too dispersed distance

measurements (Baldwin, 1977).

At present, more than half a million of QSOs have been spectroscopically identified by the Sloan Digital Sky Survey (Lyke et al., 2020). For about 15,000 such sources, an X-ray (mostly serendipitous) observation is also available in the *XMM-Newton* and/or *Chandra* archives.

Employing these data, starting from 2015 our group has proven how quasars, although they can not (yet) be used as standard candles, they are "standardizable" candles (Risaliti & Lusso, 2015; Lusso & Risaliti, 2016, 2017; Risaliti & Lusso, 2019; Lusso et al., 2020; Bisogni et al., 2021). This is due to the well known non-linear relation between their UV and X-ray luminosity (Tananbaum et al., 1979; Lusso et al., 2010).

The non linearity of the relation allows us to derive quasar distances from their X-ray and UV flux densities, and to build a Hubble diagram of quasars up to $z \sim 7$ (Risaliti & Lusso, 2019; Lusso et al., 2020) pushing our knowledge way further than the $z \approx 2$ limit of today's Supernovae Ia (Scolnic et al., 2018). In the disc-corona framework, the UV emission of quasars comes from an accretion disc, where the gravitational energy of the accreting gas is converted into radiation (Shakura & Sunyaev, 1973), while the X-ray emission comes from the inverse Compton scattering of a fraction of the UV photons by a "corona" of hot plasma (Haardt & Maraschi, 1993). Since the X-ray emission is persistent, and the X-ray corona would cool down rapidly as a consequence of the inverse-Compton process, it is obvious that a physical process continuously transferring energy from the disc to the corona must be present in quasars. The observed non-linear $L_{\rm X} - L_{\rm UV}$ relation, which can be expressed as $\log L_{\rm X} \propto L_{\rm UV}^{\gamma}$ with $\gamma \approx 0.6$, is a consequence of such mechanism. To date several attempts to reproduce the underlying mechanism through a physically-motivated model have been performed (Haardt & Maraschi, 1991, 1993; Haardt et al., 1994; Nicastro, 2000; Merloni, 2003; Lusso & Risaliti, 2017; Arcodia et al., 2019), unfortunately with a disappointing lack of success.

The method developed by our group is however based on the sole assumption that the observed dispersion of the luminosities relation is entirely due to observational issues (dust and gas absorption, variability, geometry of the source, etc.) and therefore that there exist a physical mechanism which entwines the UV and X-ray emissions of AGN, but does not need to know more of its nature. Our previous works indeed demonstrate how well motivated said assumption is, reducing the dispersion of the relation from the historical value of 0.8 dex (Tananbaum et al., 1979), to 0.4 dex (Lusso & Risaliti, 2016) to 0.20-0.22 dex (Lusso et al., 2020) and finally reaching 0.09 dex (Sacchi et al. 2022; submitted).

In previous works (Risaliti & Lusso, 2019; Lusso et al., 2020) we have proven how an $\approx$ 2500 sources sample of selected QSOs allows to build an Hubble diagram which turned out to have a $> 4\sigma$ tension with the standard flat ΛCDM model ($H_0 = 70$ km/s/Mpc, $\Omega_{\rm M} = 0.3$, $\Omega_{\Lambda} = 1 - \Omega_{\rm M}$). In order to improve these

results we either need to tight the relation by decreasing the observed dispersion or to enlarge our sample.

The latest compilation of our samples of QSOs (Lusso et al., 2020; Bisogni et al., 2021) was based on the latest releases (at that time) of the Sloan Digital Sky Survey (DR14, Pâris et al. 2018), the Chandra X-ray Catalogue (CXC2.0 Evans et al. 2010) and the 4XMM Data Release 9 (Webb et al., 2020). With respect to that compilations, this work has two main improvements, apart from adopting the recently published, updated versions of said catalogs: we included data from the early data release (Brunner et al., 2021) of eROSITA (extended ROentgen Survey with an Imaging Telescope Array; Predehl et al. 2021) and we added the photometric redshift data from the MILLIQUAS (Million Quasar Catalog V7.2, Flesch 2021) catalog. eROSITA Final Equatorial-Depth Survey (eFEDS) AGN Catalogue (Liu et al., 2021) counts 21,952 unique sources spanning from $z \approx 0.004$ up to $z = 8$. The MILLIQUAS is a compendium of several other catalogs (including the SDSS-DR16Q catalog, Lyke et al. 2020) amounting to 1,573,824 QSOs complete of their coordinates, redshift (spectroscopic where available, photometric otherwise), object class and X-rays/radio identifier where available.

Thanks to all these improvements we accomplish two goals: firstly we enlarge our final sample by a factor 2, going from 2500 to more than 5000 sources, secondly this new sample allows us to study the dependence of the relation on two crucial aspects of our method such as the X-ray photon index and the instruments employed to obtain the X-ray data.

This Chapter is organized as follow: in Section 4.2 we present our sample and we briefly resume the cleaning procedure adopted; in Section 4.3 we analyse the observed relation between fluxes, employed as proxies of the luminosities; in Section 4.4 we illustrate the improvements linked to the usage of the eROSITA data; in Sections 4.5 and 4.6 we show a detailed study on the role of the X-ray photon index and full spectroscopic analysis in our method and their effects on the relation; in Section 4.7 we build an Hubble diagram with our QSO sample and compare our cosmographic fit with our previous works and finally we draw our conclusions.

4.2 - **Data set and cleaning procedure**

Our final clean sample is composed of 3 major subsamples:

- **MQ-4XMM**: the bulk of it is originates from the cross-match of the latest releases of the MILLIQUAS (Million Quasar Catalog V7.2, Flesch 2021) and the 4XMM-DR10 (4th release XMM-Newton Serendipitous Source Catalogue, Webb et al. 2020). The 4XMM-DR10 amounts to 575,158

	MQ-4XMM	MQ-CSC2	eROSITA
parent sample	62,491	25,654	21,952
final sample	3589	1249	1008

Table 4.1: *Number of sources in our parent and final subsamples.*

unique sources (849,991 detections); their cross-match, within 3 arcseconds, amounts to 93,855 unique sources but we further reduced our sample to the 62,491 sources for which the SDSS *ugriz* magnitudes were available. The redshift of these sources span from $z = 0.001$ up to $z \approx 6.5$. This final clean subsample alone amounts to ≈2600 sources;

- **MQ-CSC2**: the second largest subsample comes from the cross-match of the latest releases of the MILLIQUAS and the latest release of the Chandra catalog (Evans et al., 2010). The CSC2.0 amounts to 317,167 unique sources (928,280 detections); their cross-match, within 3 arcseconds, amounts to 40,878 unique sources which reduce to 25,654 once we ask for the SDSS *ugriz* magnitudes to be available for our sources for this subsample too. The redshift windows spanned by this subsample is similar to the one of the previous subsample. The final clean sample amounts to ≈1250 sources;

- **eROSITA**: the third contributor by dimension is the eROSITA Final Equatorial-Depth Survey (eFEDS) AGN Catalogue (Liu et al., 2021) which amount to 21,952 unique sources spanning from $z \approx 0.004$ up to $z = 8$. We employed both the X-rays complete analysis available in Liu et al. (2021) as well as the multiwavelength data presented in Salvato et al. (2021) and the final clean subsample amounts to ≈1000 sources.

From the first two subsamples, originating from the Milliquas catalog, we eliminated all sources with photometric z smaller than 0.7. This because their redshifts are rounded to $0.1z$ (Flesch, 2021) and below $z = 0.7$ this approximation do not allow their usage for cosmological studies.

Table 4.1 resumes the number of sources in our parent and final subsamples and Figure 4.1 shows the redshift stacked distribution of our final clean subsamples.

To these we added 159 sources from the Chandra-COSMOS legacy sample described in Bisogni et al. (2021), 13 sources with $z < 0.1$ and 29 sources with $z > 4$ for which pointed observations are available and have been fully described in Lusso et al. (2020).

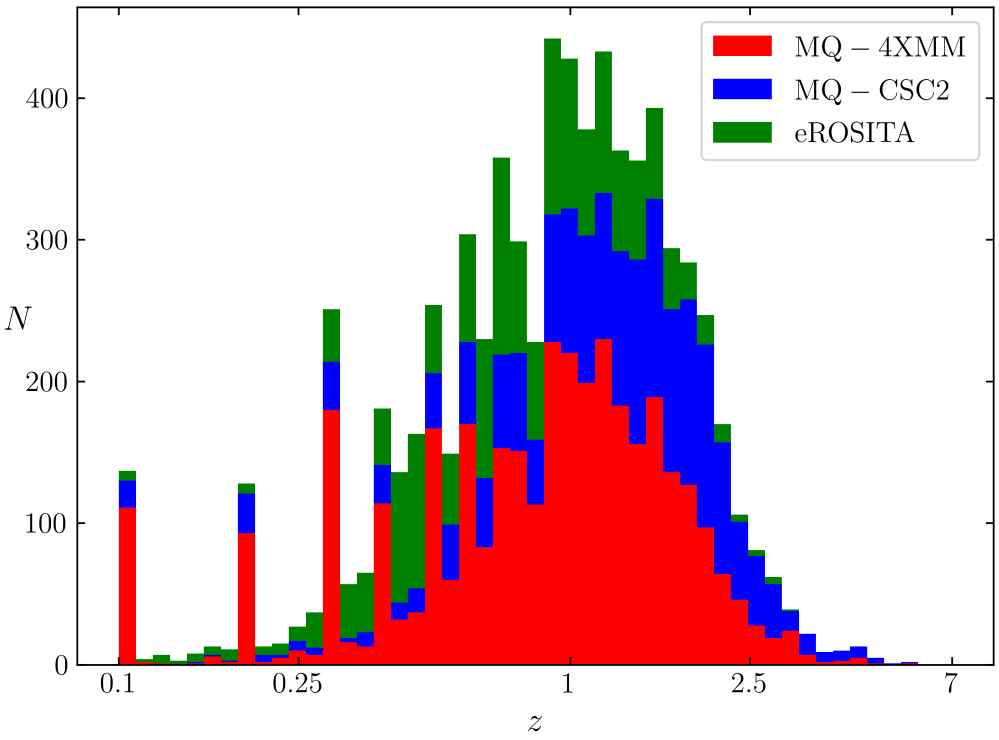

Figure 4.1: *Stacked redshift distribution of our clean final sample.*

4.2.1 *2500 Å and 2 keV flux computation*

As broadly discussed in previous works (Risaliti & Lusso, 2019; Lusso et al., 2020; Bisogni et al., 2021) we adopt the 2500 Å and 2 keV monochromatic flux as proxies of the accretion disc and corona emission respectively.

For the MQ-4XMM and MQ-CSC2 subsamples, the 2500 Å rest frame flux is obtained by an automatized procedure which interpolates or extrapolates the rest frame photometric SED of each source, employing the 5 SDSS *ugriz* magnitudes. This procedure have been broadly tested in our previous works (see Lusso et al. 2020 for a detailed explanation of the method) and it has proven to be able to retrieve 2500 Å monochromatic fluxes in excellent agreement with the ones one can obtain from a complete spectroscopic analysis. For the eROSITA subsample we adopted the multiwavelength spectroscopy provided by Salvato et al. (2021) which relies on the fact the for all sources of the eROSITA AGN parent sample, HSC (Aihara et al., 2018) and/or KIDS (Kuijken et al., 2019) data are available.

For the MQ-4XMM subsample the unabsorbed monochromatic 2 keV flux is obtained from the photometry in the soft (0.5-2 keV) and hard (2-12 keV) band through the pivot-points method we developed and abundantly tested in our previous works (see Risaliti & Lusso 2019 and Lusso et al. 2020 for details). For the MQ-CSC2 subsample the unabsorbed monochromatic 2 keV flux is retrieved through automated spectroscopic analysis of the X-ray spectra obtained from the CSC2.0 catalog (Evans et al., 2010). Again this procedure has been deeply illustrated in a previous work (Bisogni et al., 2021) and its robustness has been broadly proven therein.

Finally for the eROSITA subsample the unabsorbed monochromatic 2 keV flux is directly provided by the eROSITA AGN catalog, the value adopted is the one obtained with the best fitting model as described in Liu et al. (2021).

4.2.2 *Sample cleaning*

In cleaning our sample we followed the approach developed in our previous works (Risaliti & Lusso, 2015, 2019) and detailed in Lusso et al. (2020) and Bisogni et al. (2021): mainly we removed from our sample all sources with bad quality observations (e.g. when the source falls on bad pixels of the detector) and the ones showing dust-absorption or host-galaxy contamination in the UV band, photoelectric absorption in the X-ray band and/or radio-loudness. Finally we removed from our sample all the source affected by Eddington bias. Here we will not go into the details of the method but we will provide a general description indicating where slightly different approaches have been adopted.

X-ray cleaning

The quality of X-ray data heavily affects the over all results of all our method as they are usually affected by heavier uncertainties with respect to optical/UV data, therefore we maintained the particularly strict criterions developed and described in our previous works for this band.

For the MQ-4XMM subsample we started by considering only observations with over all good quality (OBS_CLASS ≤ 3), low level of spurious detection (SUM_FLAG < 3), and available EPIC data (EP_TIME > 0). We further excluded sources with signal to noise ratio below 1 in either the soft or hard band. As photoelectric absorption is naturally heavier in the soft band and a too steep spectrum could be due to observational issues, and selected sources with an X-ray photon index $\Gamma_{\rm X} - \delta\Gamma_{\rm X} \geq 1.7$ and $\Gamma_{\rm X} + \delta\Gamma_{\rm X} \leq 2.8$ up to redshift $z = 4$, where $\delta\Gamma_{\rm X}$ is the 1σ error on the photon index. Above redshift $z = 4$ we relaxed our criterion requiring sources with $\Gamma_{\rm X} \geq 1.7$ as the uncertainties at higher redshift would eliminate the vast majority of our sources.

For the MQ-CSC2 subsamples we proceeded in a similar way, excluding sources with a signal to noise ratio smaller than 1 in the soft band and an off-axis angle larger than 10 arcmin. We addressed the issue of photoelectric absorption in the same way we did for the MQ-4XMM subsample using as $\Gamma_{\rm X}$ the photon index retrieved by the vary same spectroscopic analysis from which we obtained the 2 keV monochromatic flux.

For the eROSITA subsample we addressed both issues, the one of X-ray data quality and photoelectric absorption, at the same time by exploiting the classification provided by Liu et al. (2021): we selected only unobscured sources (NHclass=2). By doing so we single handedly excluded sources with data quality so poor that no information on the absorption could be retrieved (NHclass=1) and sources with mildly- and well-measured absorption (NHclass=3,4), see Liu et al. (2021) for a detailed description on how the class were attributed.

Optical/UV cleaning

As both the presence of dust along the line of sight and/or the contamination by host-galaxy could affect the measure of the 2500 Å monochromatic flux, we cleaned our sample of reddened sources. We computed the slope of the rest frame photometric SED between 1450 and 3000 Å (Γ_2) and eliminated from our sample all the sources with $|\Gamma_2 - 0.40| > 1.1$. The photometric SED were retrieved from the SDSS, HSC and/or KIDS magnitudes for the MQ-4XMM and MQ-CSC2 subsamples and for the eROSITA subsample respectively. This choice slightly differs from the one adopted in previous works where along with the Γ_2 also the slope Γ_1, between 0.3 and 1 μm was computed and then employed to eliminate all

sources outside a circle, in the $\Gamma_1 - \Gamma_2$ plane of radius 1.1 centred in $(0.85, 0.40)$, which corresponded to a reddending $E(B-V) \lesssim 0.1$. The reasons behind this choice are that the color affects the cleaning procedure in a lighter way with respect to other criteria such as the Eddington bias or the photoelectric absorption. Secondly, doing so allows us to neglect the infrared data analysis needed in order to correctly estimate the Γ_1 slope which falls fully in the NIR/MIR regime starting from low redshift. Thirdly the criterion we adopted, which considers only the Γ_2, still corresponds to a reddening $E(B-V) \lesssim 0.1$ given that for the SED of quasars a reddening affects more prominently the slope Γ_2 rather than the Γ_1.

Radio-loud and BAL

It is well known that radio emission from radio-loud QSOs can affect the estimate of the 2 keV monochromatic flux enlarging it with respect to radio-quiet AGN (Zamorani et al., 1981; Wilkes & Elvis, 1987). Symmetrically Broad Absorption Line (BAL) objects are equally known to be X-ray obscured with respect to non-BAL AGN (Green et al., 1995; Gallagher et al., 1999; Brandt et al., 2000).

It is therefore important to eliminate both types of sources as an enhanced X-ray emission would result in a flatter estimation of the luminosity relation while including in our sample X-ray obscured objects would lead to artificially steeper estimates for the slope on the relation and both effects would compromising our method.

For the eROSITA subsample we therefore cross-matched (with a standard 3 arcsec maximum distance) our sample with the FIRST catalog and the SDSS DR16Q catalog (Lyke et al., 2020) and eliminated all sources with radio-loudness parameter R ($= F_{6\,\mathrm{cm}}/F_{2500\,\text{Å}}$) larger than 10, as done in our previous works and defined by Shen et al. (2011), and balnicity index BI_CIV > 0 (Weymann et al., 1991; Pâris et al., 2018).

For the MQ-4XMM and MQ-CSC2 subsamples we adopted the same method described above in order to eliminate BAL objects, while for radio-loud sources we employed a more conservative choice which nonetheless does not affect our statistic significantly: we eliminated all objects which in the Milliquas catalog had a flag signaling a radio counterpart.

Eddington bias

As QSOs are variable X-ray sources, an object whose average flux is comparable with the observation sensitivity limit will be caught only when on positive fluctuation. This introduces a bias in the sample (Eddington bias) and need to be corrected by eliminating these borderline sources.
In order to do so we need to compare the observation limit flux f_{lim} with the

expected 2 keV flux $f_{\rm exp}$ of the source, which is computed starting from the 2500 Å monochromatic flux obtained by SED interpolation through the assuming a value of 0.6 for the slope of the $L_{\rm X} - L_{\rm UV}$ relation (Lusso & Risaliti, 2016).

The observation limit flux is obtained from the exposure time and off-axis angle of each observation. For the MQ-4XMM and MQ-CSC2 subsamples the procedure thanks to which we obtained $f_{\rm lim}$ has been abundantly illustrated in Lusso et al. (2020) and Bisogni et al. (2021) respectively. To briefly summarize it, for the MQ-4XMM subsample one needs to take the background- and vignetting-corrected exposure time and then can straightforwardly compute the sensibility of the instrument for each observation and source following Watson et al. (2001). For the MQ-CSC2 one estimates the flux limit by computing the background flux in each observation. The conversion between background and limit fluxes is performed by fixing the choice of desired signal to noise ratio and doing some algebra (see Section 3.2.2 of Bisogni et al. 2021 for a detailed description, with all the formulas we omitted, of the calculation). For the eROSITA subsample, similarly to what we did for the MQ-4XMM subsample, we employed the vignetting-corrected exposure time provided by the eFEDS catalog (Brunner et al., 2021) to compute the flux limit following the indications on the matter of the eROSITA Science Book (Merloni et al., 2012).

We accept in our final sample only sources satisfying the condition $\log f_{\rm exp} > \log f_{\rm lim} + k\delta$, where δ is the observed dispersion of the sample and k is a multiplicative factor. The product $k\delta$ is taken as equal to 0.9 for the MQ-4XMM subsample, equal to 0.6 for the MQ-CSC2 subsample while for the eROSITA subsample the prescription $k\delta = 0$ was employed, meaning that we simply asked for the expected flux to be larger than the observable limit.

All these values were retrieved by inspecting the behaviour of the relation slope, intrinsic dispersion and sample dimension as functions of the $k\delta$ choice. As $k\delta$ grows the expected behaviour for the slope is to increase as well and then to saturate around the standard value of 0.6. The dispersion on the other hand should decrease up to the point of saturation of the slope and than it should start to grow. The number of sources employed needs to be checked in order to be sure to work with a statistically significant sample. The expected behaviour can be motivated as follow: as $k\delta$ grows one is eliminating more and more source caught in a positive fluctuation of their X-ray emission. These sources flatten the slope of the relation because, with their larger than "standard" X-ray emission, they can be found in the upper-left region of the $L_{\rm X} - L_{\rm UV}$ diagram. So eliminating these undesired sources the slope flattens and the dispersion decreases. This up to the point where all "bad" sources are eliminated. At this point the slope stops to flatten and the dispersion start to grow to the fact that the sources one is eliminating from this point on are "good" ones (for a detailed description of this procedure see Section 7.3 of Lusso et al. 2020 and for the computation of the slope and intrinsic dispersion for our

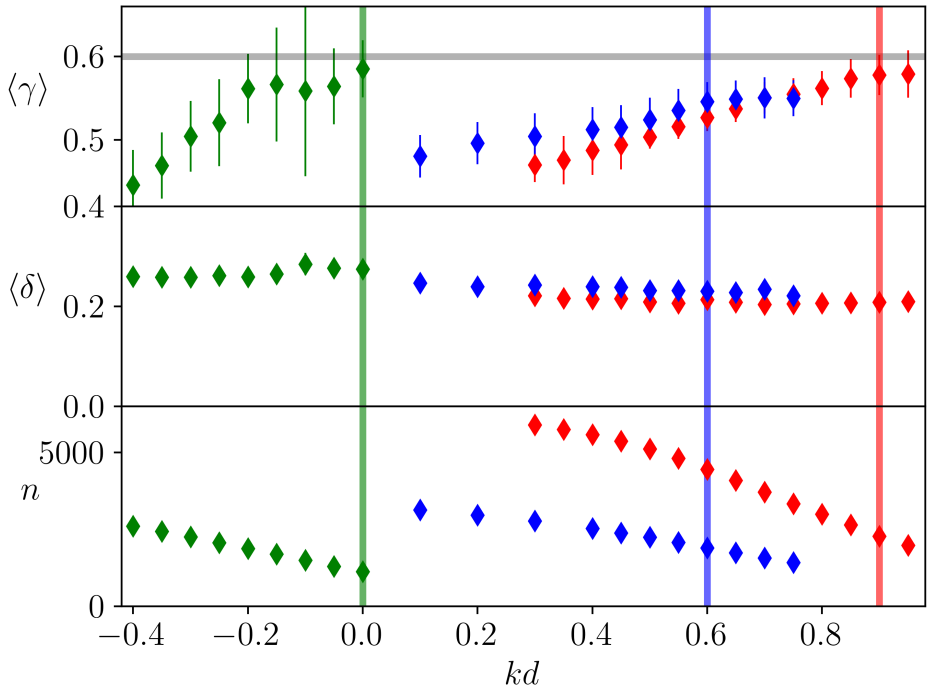

Figure 4.2: *From top to bottom the slope and intrinsic dispersion of the relation and the number of sources composing the samples as functions of $k\delta$ values. The colors are the same employed in previous plots indicating different subsamples (red for MQ-4XMM, blue for MQ-CSC2, green for eROSITA). The grey solid line is the "standard"* 0.6 *value for the slope while the colored vertical lines indicates the choices of $k\delta$ for each subsamples, see main text for details.*

subsamples see next Section).

Figure 4.2 shows in three panels the slope, intrinsic dispersion and dimension of the subsamples (red data points fo the MQ-4XMM subsample, red and green for the MQ-CSC2 and eROSITA subsamples respectively) and the vertical lines show the choices of $k\delta$. As one can notice for the eROSITA subsample the saturation occurs even before $k\delta$ gets positive so a value of 0 has been chosen in this case.

4.3 - **Analysis of the fluxes relation**

As in previous works we proceed checking for trends in the fluxes relation with the redshift in a cosmology-independent way. We first divided the sample in narrow redshift bins, from $z = 0.7$ up to $z = 5$; the width of the bins varies in order to both

be sure to have enough statistics in each bin and that the dispersion in distances within each bin is smaller than the one of the luminosity relation. This allows us to use the UV and X-rays fluxes, normalised the to $10^{-27.4}$ and $10^{-31.5}$ erg/s/cm^2/Hz, respectively, as proxies of the correspondent luminosities, hence getting ridden of the dependence on the chosen cosmology.

If we choose a parametrization $\log F_{\rm X} = \hat{\beta} + \gamma \log F_{\rm UV}$, we expect a constant value of γ in all redshift bins, and a redshift evolution of the normalization $\hat{\beta}$; note the difference between the β appearing in the luminosity relation, which does not evolve with redshift, and the $\hat{\beta}$ of the flux relation, which encodes the information on the expansion of Universe. Above $z = 4$ not enough statistics is available to well fit the relation.

We fitted the fluxes relation in each bin with the Python package emcee (Foreman-Mackey et al., 2013), a pure-Python implementation of Goodman & Weare's affine invariant Markov chain Monte Carlo (MCMC) ensemble sampler.

Figure 4.3 shows the best-fit parameters γ, $\hat{\beta}$ and δ (slope, intercept and dispersion respectively) of the fluxes relation, along with their uncertainties. The fits of the relation in all the redshift bins are shown in figure 4.4.

Data show no clear trend with the redshift for the slope of the relation or the dispersion while the intercept mimic the Hubble diagram although not exactly given that, because of the fixed normalization, in each bin the slope and intercept covariance is different; it actually mirrors it given that, as redshift grows, the intercept of the relation between fluxes needs to decrease by definition.

This result confirms once more the ones obtained in previous works (Risaliti & Lusso, 2015; Lusso & Risaliti, 2016; Lusso et al., 2020): the slope of the relation does not evolve with redshift and this allows the standardization of quasars for cosmological usage.

For completeness the fluxes-fluxes plots for the relation fitting in each redshift bin are shown in figure 4.4.

4.4 - **eROSITA**

One most important improvement with respect to previous samples of cosmological QSOs is the contribution of eROSITA. eROSITA (extended ROentgen Survey with an Imaging Telescope Array; Predehl et al. 2021) is the primary instrument of the Russian-German "Spektrum-Roentgen-Gamma" (SGR) mission, successfully launched on July 2019. eROSITA has an on-axis sensitivity at 1 keV comparable with the one of XMM-Newton but coupled with a wider field of view and better spectral resolution (Predehl et al., 2021).

The eROSITA Final Equatorial Depth Survey (eFEDS), while being relatively shallow (the entire observation took approximately 100 hours) covers an area of

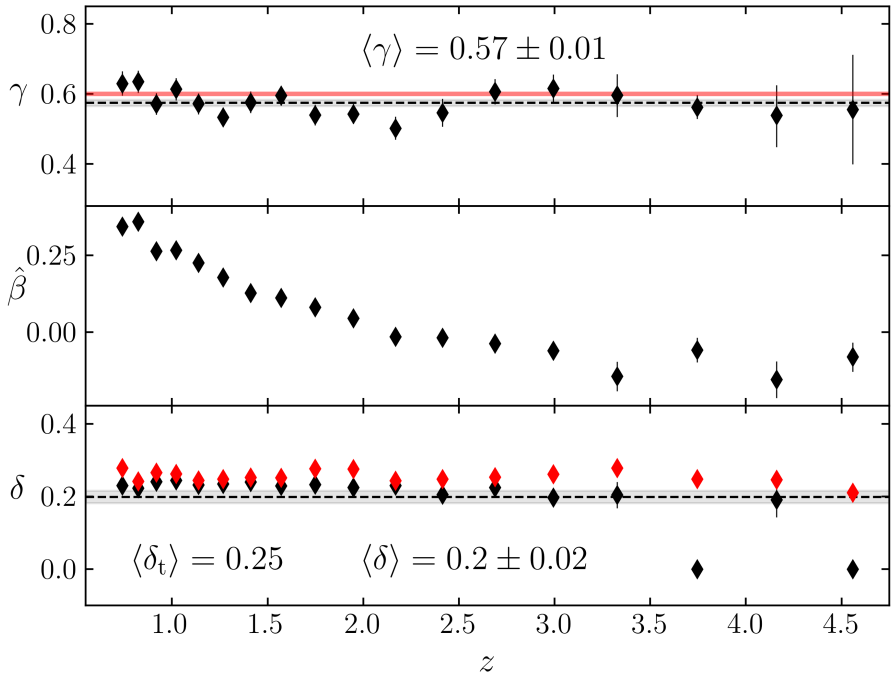

Figure 4.3: *Redshift evolution of the slope γ, the intercept $\hat{\beta}$ and the dispersion δ of the fluxes relation. The dashed lines show the means while the shaded region the 1σ uncertainties. The red line indicates the standard 0.6 value for the slope.*

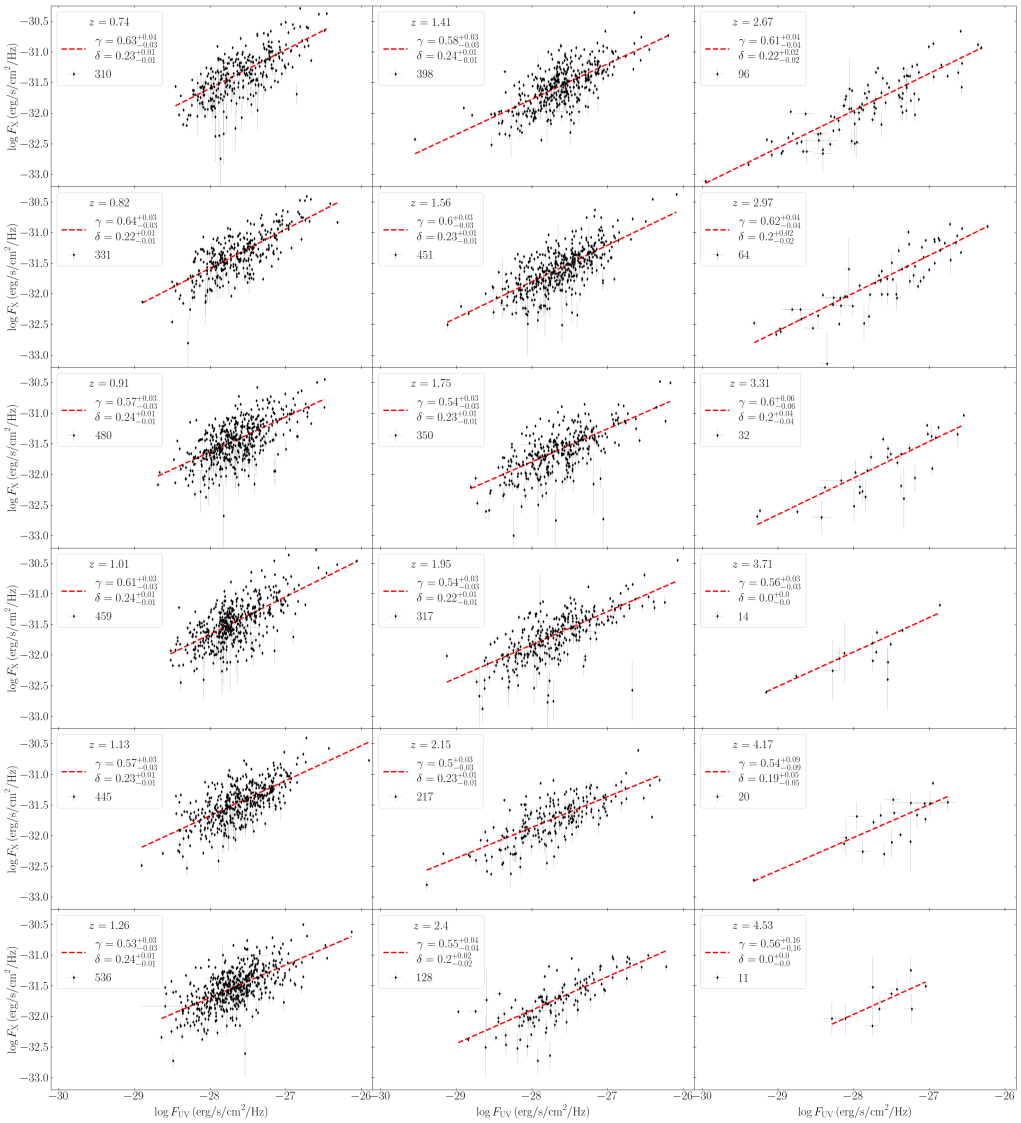

Figure 4.4: *X-ray−UV plots for each redshfit bins of the entire sample. The legend of each plot reports the central redshift value, the parameters of the fit (slope and intrinsic dispersion) and the number of sources in the bin. The best fit is represented by the red dashed line.*

140 deg^2, making it the larger with respect to XMM or Chandra surveys (see Brunner et al. 2021 for a comparison). Furthermore the covered area overlaps with several others optical/NIR surveys, providing rich multiwavelength information for all observed sources (Salvato et al., 2021).

The eROSITA AGN catalog (Liu et al., 2021) collects 21,952 unique sources spanning from $z \approx 0.004$ up to $z = 8$. For the vast majority of the sources in the catalog, along with the X-ray, optical data are available from the HSC Wide area Survey (Aihara et al., 2018) and the KIDS-VIKING (Kuijken et al., 2019). This is fundamental for our goal of obtaining good estimates of the QSOs 2500 Å and 2 keV emission. the final clean sample of eROSITA QSOs amounts to ≈ 1800 objects on a redshift range extending up to $z \approx 3$. This does not improves dramatically our statistic as shown in Figure 4.1, however the importance of these sources is that they prove the "standardizability" of QSOs as standard candles does not depend on the observatory employed in obtaining the X-ray data as already stated in our previous work where we demonstrated the very same concept by analysing Chandra data (Bisogni et al., 2021).

To further prove this we studied the possible evolution of the parameters of the luminosity relation using only eROSITA data. We followed the very same procedure described in the previous Section but employing the sole eROSITA subsample. Figure 4.5, is the analogous of Figure 4.3 and it shows, from top to bottom, the dependence of the slope γ, intercept $\hat{\beta}$ and dispersion δ on the redshift. As one can see there is no evolution for the slope and its mean value (shown as a black dashed line with a shaded grey area indicating the 1σ region) is compatible with the canonical 0.6 (solid red line). The fluxes intercept $\hat{\beta}$ mirrors once again the Hubble diagram, its evolution is flipped. The bottom panel shows the intrinsic $\delta_{\rm i}$ and total $\delta_{\rm t}$ (black and red data points). The mean values are comparable with the ones obtained for most recent compilation of samples of cosmological QSOs (Lusso et al., 2020; Bisogni et al., 2021).

As stated above, adding eROSITA data to our sample is not needed in order to enlarge our statistic which is already satisfactory with XMM and Chandra alone, but further confirms the robustness of our method and its independence on the instruments employed.

This will be true even when eROSITA will release its 4-year survey as firmly assessed by Lusso (2020). As eROSITA QSOs will have a redshift distribution heavily skewed towards the $z < 2$ region, they will there greatly enhance the available statistic. However the true power of the Hubble diagram one can build with QSOs lies in the $z > 2.5$ where one can discriminate between different cosmographic models (Risaliti & Lusso, 2019; Bargiacchi et al., 2021). Hence the eROSITA contribution, even after the 4 years release, will not improve dramatically the power of the QSO Hubble diagram which in the $z < 2$ region is already satisfactorily populated.

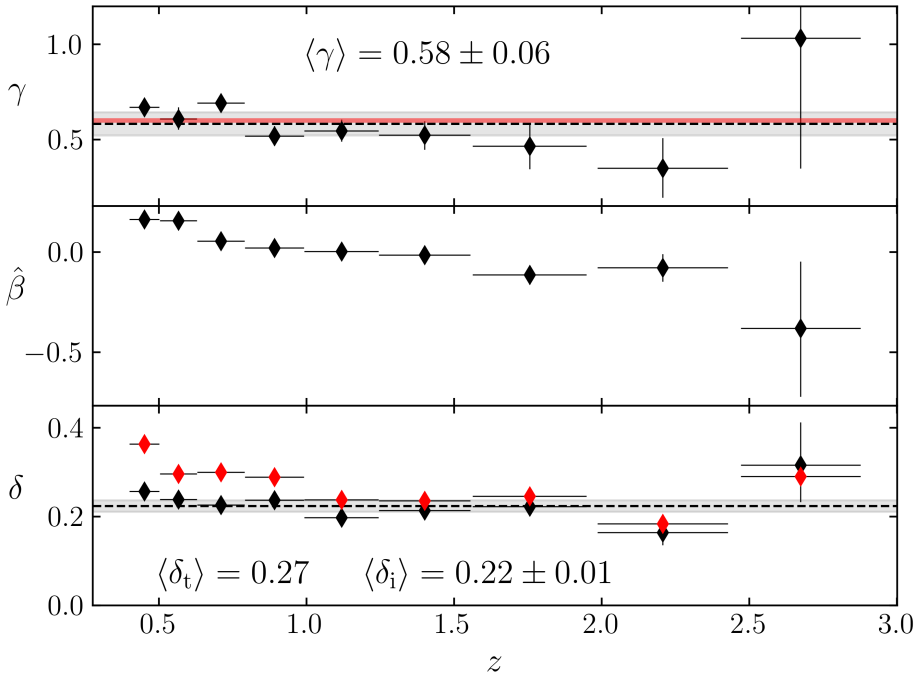

Figure 4.5: *Redshift evolution of the slope γ, the intercept $\hat{\beta}$ and the dispersion δ (intrinsic in black and total in red) of the fluxes relation for the eROSITA subsample. The dashed lines show the means while the shaded region the 1σ uncertainties. The red line indicates the standard 0.6 value for the slope.*

4.5 - **X-ray photon index**

The great improvement in the statistic of our sample, going from the ≈2400 sources of the latest compilation to the more than 5000 of the current one, allows us to better investigate the role of the X-ray photon index on the property of the luminosities relation.

We already investigated the optimal threshold in order to cut out all possible photoelectric absorption, now our goal is to understand whether and eventually how the luminosities relation in quasars is affected by the steepness of the X-ray spectrum of the source.

In order to do so we divided our final clean sample, composed of more than 5000 sources coming from three different instruments, in four photon index slices as follow:

- $\Gamma_X < 2$,
- $2 < \Gamma_X < 2.2$,
- $2.2 < \Gamma_X < 2.4$,
- $\Gamma_X > 2.4$,

this choice ensures on the one hand the possibility to fully investigate any effect of the photon index selection given the narrowness of the slices, on the other hand it guarantees that in each slice there are enough sources in order for any kind of found dependence to be statistically significant.

For the MQ-4XMM and MQ-CSC2 subsamples we employed the X-ray photon index we derived from the photometric or spectroscopic analysis in order to clean our sample. For the eROSITA subsample we employed the X-ray photon index provided by the AGN catalog computed with the single-powerlaw model (model 1, Gamma_BF in Liu et al. 2021).

We than proceeded with the very same analysis of the relation we operated for the full sample for the sources in each slice: we fitted in narrow redshift bins the relation using fluxes as proxies of the luminosities.

Figure 4.6 shows the results. The three panels show once more the slope, intercept and intrinsic dispersion of the fluxes relation. The colors and markers indicates the different slice: black diamonds, blue squares, magenta triangles and red circles from flatter to steeper. For comparison a grey horizontal line show the indicative $\gamma = 0.6$ value for the slope.

No clear effect of the X-ray photon index on either of the relation parameters is present except for the intercept $\hat{\beta}$ but this is due to the correlation between fluxes and photon indexes which we did not corrected for modifying the fluxes normalization. This is in perfect agreement with our previous results and further

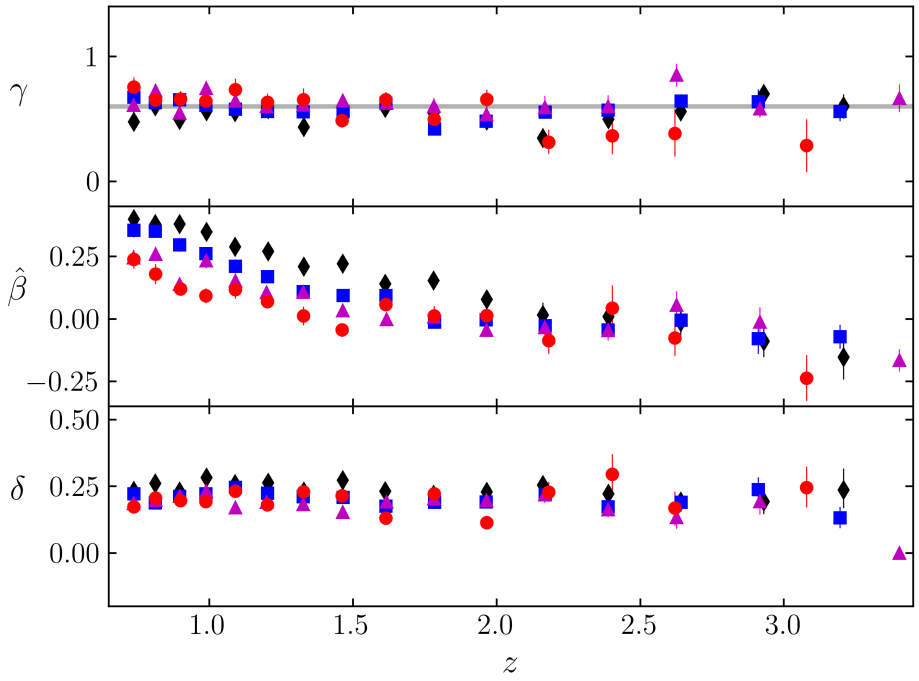

Figure 4.6: *Relation analysis on the redshift, from top to bottom the slope, intercept and intrinsic dispersion. The different colors and markers indicates the different X-ray photon index slices:* $\Gamma_X < 2$ *(black diamonds),* $2 < \Gamma_X < 2.2$ *(blue squares),* $2.2 < \Gamma_X < 2.4$ *(magenta triangles) and* $\Gamma_X > 2.4$ *(red circles).*

confirms the robustness of our method and its efficiency in eliminating all absorbed or otherwise biased source.

4.6 - **X-ray spectroscopy**

The overall goodness of our results and method heavily relies on the quality of X-ray data as these are usually affected by a larger uncertainty with respect to optical/UV data. The natural strategy to improve the quality of our X-ray data would be to use spectroscopic X-ray data rather than photometry derived ones. This equals to perform a complete X-ray spectroscopic analysis for all the sources in the MQ-4XMM subsample, as the ones from the MQ-CSC2 and eROSITA subsample have already undergone a spectroscopic analysis, however the sole MQ-4XMM subsample consist in roughly half of our final sample.

We are currently working on this task, and, as shown in a recently submit-

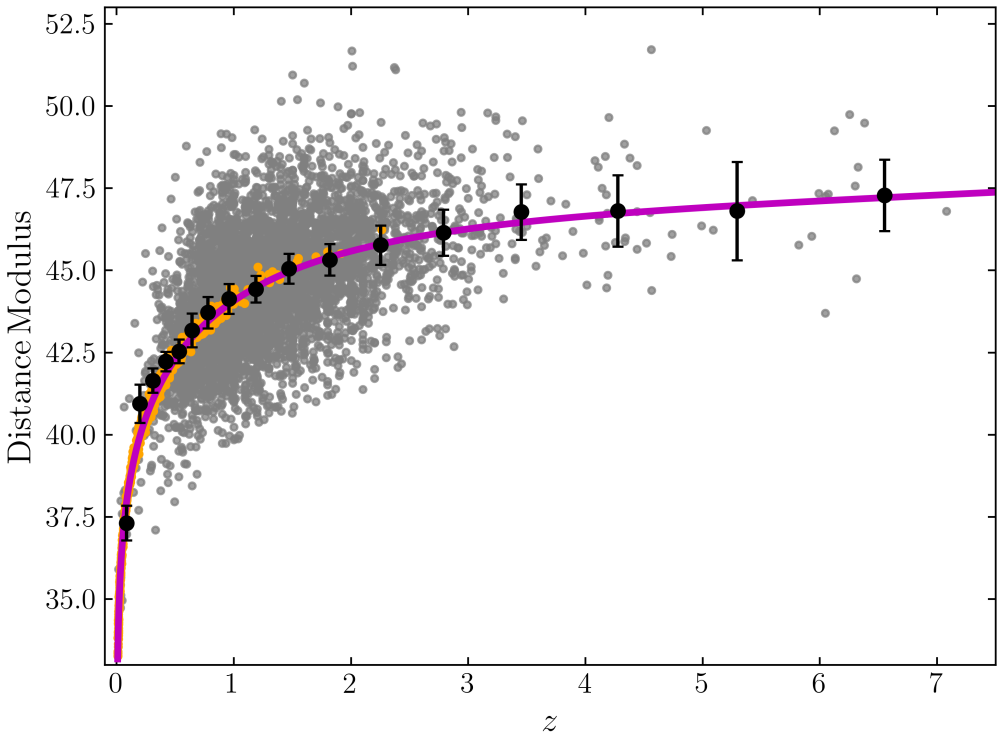

Figure 4.7: *Hubble diagram (top panel) for the clean quasar sample (grey points) and supernovae Ia (Pantheon Scolnic et al. 2018, orange points). The magenta solid line represents a fifth order cosmographic fit of the data (Bargiacchi et al., 2021), whilst the black points are averages (along with their uncertainties) of the distance modulus in narrow (logarithmic) redshift intervals, overplotted only for graphical purposes.*

ted work of ours (Sacchi et al. 2022; submitted) the usage of spectroscopically retrieved fluxes allows to significantly reduce the dispersion of the relation, further confirming that the currently observed dispersion is entirely attributable to observational effects which will be further investigated in future works.

4.7 - **Hubble diagram**

Figure 4.7 shows the Hubble diagram built with our new sample (the grey dots indicates individual sources while the black ones the mean value of the distance modulus in corresponding redshift bins) with a fifth order cosmographic fit (see Bargiacchi et al. 2021 for details on the fit) represented by a magenta solid line.

The distance modulus has been retrieved in the standard way and the QSO data were calibrated using the distance ladder through supernovae Ia (Scolnic et al.,

2018), shown as orange dots in the plot, as the distance modulus for QSOs is not absolute (see Section 9 of Lusso et al. 2020). All fitted parameters are in striking agreement with what we retrieved in previous compilation of the cosmological sample (Lusso et al., 2020; Bargiacchi et al., 2021). As a further sanity check that our conspicuous sample enlargement did not worse the quality of our data even if we added sources from different instruments, photometric redshifts and we slightly modified our color selection Figure 4.8 shows the bi-dimensional spaces for a_3 and a_4, two free parameters of the cosmographic fit. The colored contour and the blue dashed levels represents our sample and the Lusso et al. (2020) sample. As stated above the results of the new and Lusso et al. (2020) sample are in excellent agreement with our sample reaching further away from the flat-ΛCDM model as a consequence of our sample enlargement.

To give a taste of the possible cosmological application of the new sample in Figure 4.8 the black square and solid black line show respectively the flat-ΛCDM prediction for $\Omega_{\rm M} = 0.3$ and for varying values of $\Omega_{\rm M}$. As one can see the distance of our cosmographic fit with respect to the flat-ΛCDM model is well over 5σ.

Given all the addition we did to previous compilation of the QSOs sample we want to further check the legitimacy of our work by inspecting the behaviour of each subsample individually. We do so by studying the residuals of the Hubble diagram with respect to the cosmographic fit and in particular their distribution: our results are presented in Figure 4.9. The bottom panel shows the residuals (grey dots) as function of the redshift. Black dots indicates the mean value in narrow redshift bins and the magenta line highlights the 0 level. The two top panels show the distribution of the residuals for different subsamples of origin and different redshift origin. As one can see no significant evolution of the residuals with redshift is present and furthermore the distribution of each subsample is very well centred on 0 as highlighted by their means (solid colored lines plotted on top of the distributions).

Finally, in order to check the effect of the X-ray photon index on our sample, we divided our data in two subsamples: $\Gamma_{\rm X} \leq 2.2$ and $\Gamma_{\rm X} > 2.2$. Figure 4.10 shows the very same bi-dimensional space presented in Figure 4.8, this time the black dashed contours indicates the behaviour of our full sample, the blue and red contours instead represent the $\Gamma_{\rm X} \leq 2.2$ and $\Gamma_{\rm X} > 2.2$ subsamples respectively. As it is clear from the plot all contours nicely overlap further confirming that all our selection procedures have been performed correctly.

4.8 - **Conclusions**

With respect to previous compilations of samples of cosmological quasars we almost tripled the dimension of our final clean sample. We did so by adopting the

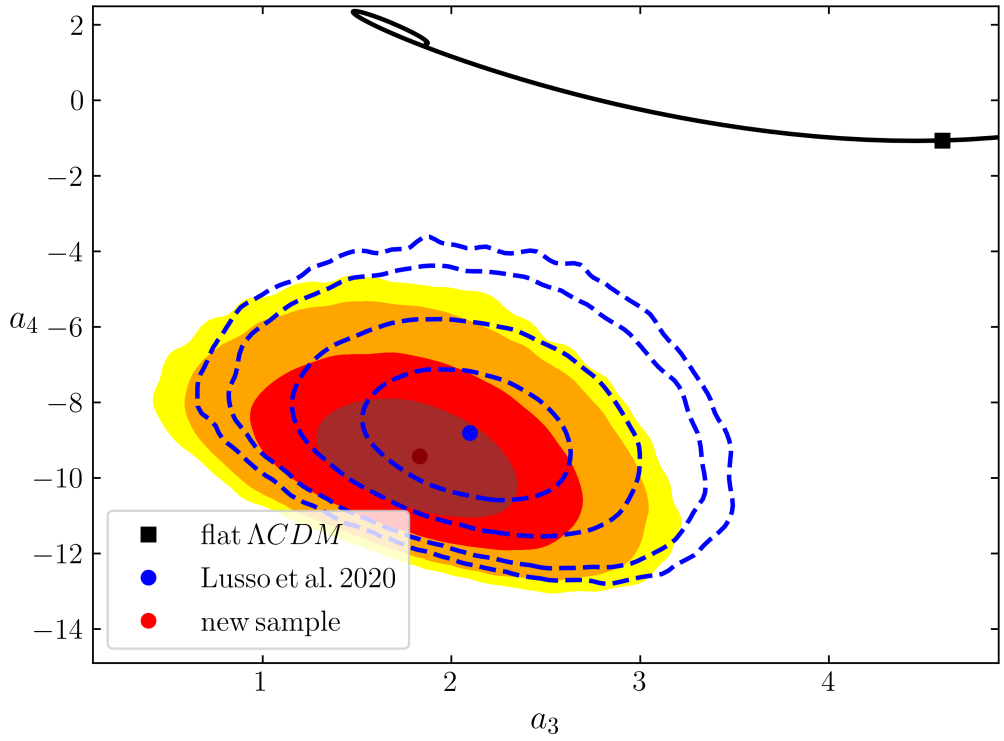

Figure 4.8: *Bi-dimensional space for the cosmographic free parameters a_3, a_4. The contour plot in red shades show the confidence levels at 1, 2, 3 and 4 σ for the best-fit on the real set of data (quasars+SNe) of our new sample. The blue dashed contours show the same confidence levels for the sample of QSOs presented in Lusso et al. (2020). The black square corresponds to the prediction of the corresponding flat-ΛCDM model from the expansion in $z = 0$ and the black line the results one would obtain varying the value of $\Omega_{\rm M}$.*

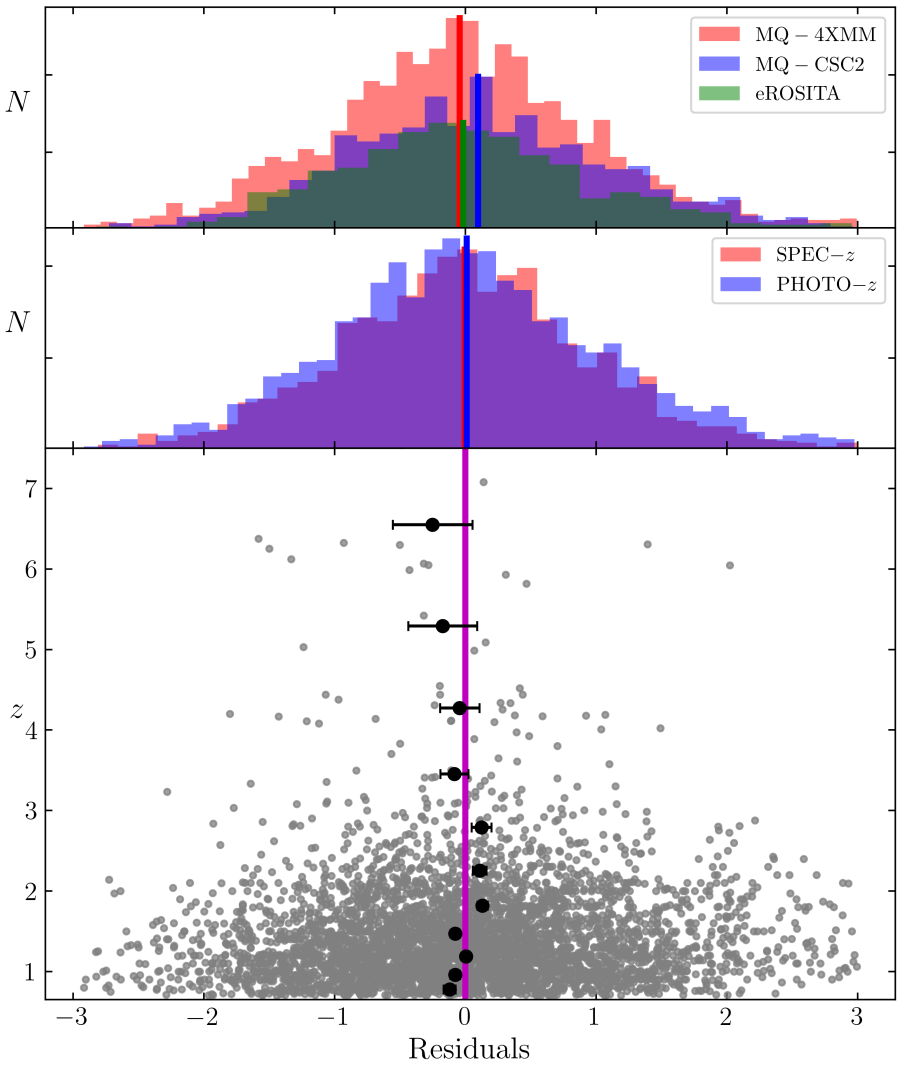

Figure 4.9: *Distribution of the Hubble diagram residuals. the colors employed are the same of previous plots. The magenta solid line indicates the* 0 *value. For the distribution on the right panels the horizontal colored lines indicates the means of the distribution.*

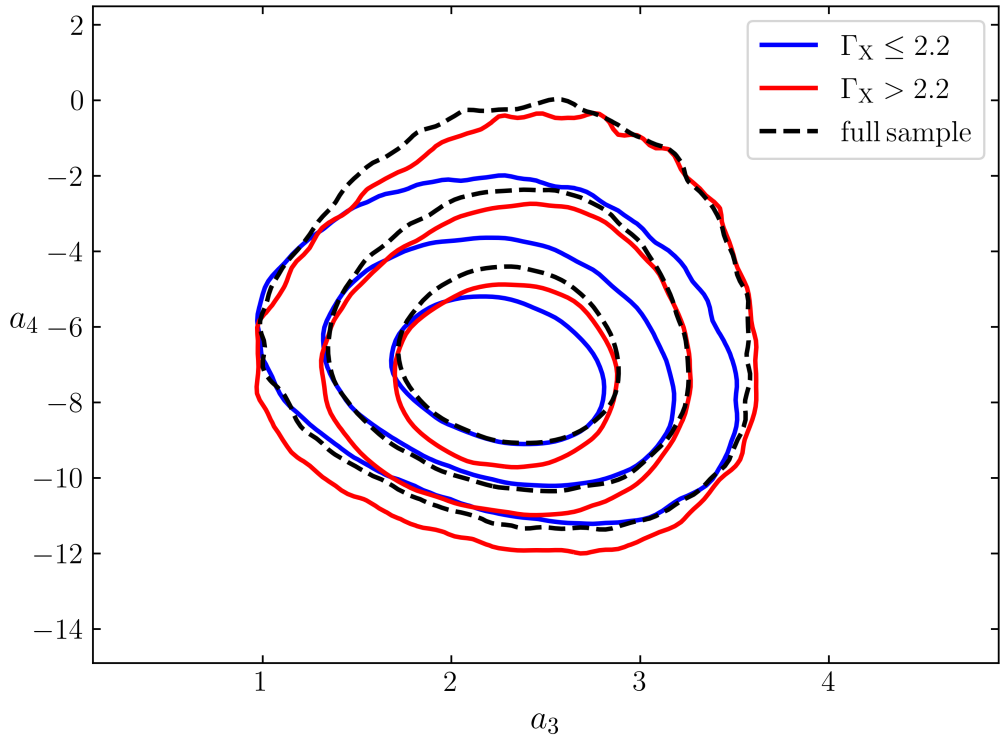

Figure 4.10: *Bi-dimensional space for the cosmographic free parameters* a_3, a_4. *The contours in blue and red show respectively the levels at 1, 2 and 3* σ *for the* $\Gamma_X \leq 2.2$ *and* $\Gamma_X > 2.2$ *subsamples. The black dashed contours show the same confidence levels for the full sample.*

latest compilation of the *XMM-Newton* and *Chandra* X-ray catalogs, by including sources with photometric redshift from the MILLIQAUS, by enforcing a less restrictive optical color selection and by adding, for the very first time, quasars observed by eROSITA and presented in the eFEDS AGN catalog. Thanks to all this improvements we built a final clean sample of more than 5000 quasars.

We than checked the sanity and robustness of our method by studying the behaviour of luminosities relation and the Hubble diagram with respect to different variables: the choice of the instrument employed in retrieving the X-ray data, the X-ray photon index, the origin of the redshift.

All this investigation proved that our sample is well built. The slope of the relation does not evolve with the redshift, the parameters of the cosmographic model used to perform the fit of the Hubble diagram are in striking agreement with the ones obtained in previous works and finally the distribution of the residuals of the Hubble diagram are perfectly symmetrical.

5 Quasars as high-redshift standard candles

The Hubble diagram is one of the fundamental observational tools in cosmology. Extending it to high redshifts is a powerful way to test possible deviations from the "concordance" flat-ΛCDM model. In the past few years we have employed quasars as high-redshift standard candles, populating the Hubble diagram up to $z \sim 7$, and finding a strong deviation from the concordance model. Such a result has obvious far-reaching implications for cosmology, and hinges upon the accuracy and reliability of the non-linear X-ray to UV luminosity relation, used to determine quasar distances. Here we present a new study for a sample of quasars at $z > 2.5$, with high-quality X-ray and UV observations, for which we performed a complete one-by-one spectral analysis. We find that not only the X-ray to UV correlation still holds at these redshifts, but its intrinsic dispersion is as low as 0.12 dex (previous works reached 0.20-0.22 dex). For a sample of quasars at $z \sim 3$ with particularly high-quality observations the dispersion further drops to 0.09 dex, a value entirely accountable for by intrinsic variability and source geometry effects. Using this sample alone, we obtain a measurement of the luminosity distance at $z \sim 3$ with 15% uncertainty, and in a 4σ tension with the concordance model.

5.1 - Introduction

As already stated in the Introduction of the previous Chapter, a comprehensive model capable of explaining the interplay between accretion disc and corona in quasars is not yet available. The analysis of the $L_{\rm X} - L_{\rm UV}$ relation relies then uniquely on observational evidence. For this reason, it is fundamental to further investigate the relation with the main goals of (1) ruling out possible redshift-related systematic effects in the determination of distances, and (2) reducing the observed dispersion, in order to improve its effectiveness as cosmological probe. We will show that these two goals are not independent: in fact, reducing the observed dispersion is an effective way to rule out major systematic effects.

The state of the art in the study of the X-ray to UV relation in quasars is presented in Lusso et al. (2020) and Bisogni et al. (2021). The two samples

analyzed in these works mainly consist of sources with serendipitous *XMM-Newton* or *Chandra* X-ray observations and SDSS optical/UV spectra. The flux densities are estimated from the photometric data points in both the optical/UV and X-ray bands in the former work while in the latter the X-ray flux densities were obtained through automated spectroscopic analysis. In both works the X-ray to UV luminosity relation is analyzed by splitting the sample in narrow redshift intervals employing the same procedure described in Section 4.3 of the previous Chapter. The main results of these studies are that *a)* the relation holds in the whole $z \sim 0.5$-7.5 redshift range, with an average intrinsic dispersion of $0.20 - 0.22$ dex; *b)* the measured values of γ do not show any hint of evolution, and are consistent with a constant value of ~ 0.6; *c)* the inferred Hubble diagram of quasars is in a $> 4\sigma$ tension with the standard flat ΛCDM model (Risaliti & Lusso, 2019; Lusso et al., 2020; Bargiacchi et al., 2021).

Here we present the most detailed study to date of the X-ray to UV relation for a sample of 130 high-redshift ($2.5 < z < 5$) quasars. The two aims described above were pursued in the most direct way: we performed a complete UV and X-ray spectroscopic analysis of all the sources in the sample, in order to improve the accuracy of flux measurements. The sample covers an optimal redshift interval to test possible deviations of the Hubble diagram from the standard cosmological model, and its size balances the need for a high enough statistics and the feasibility of a complete spectroscopic analysis.

5.2 - **Sources and flux analysis**

5.2.1 *Sample selection*

The 130 quasar sample analysed here is drawn from three main catalogues. *SDSS-XMM* The bulk of our sample is composed by 81 quasars from the cross-match between the SDSS DR16 Quasar catalog (Flesch, 2021) and the *XMM-Newton* Serendipitous Source Catalogue Data Release 10 (Webb et al., 2020). The sample selection follows the procedure described in Lusso et al. (2020), and consists of the following filters:

- removal of all the known Broad Absorption Line (BAL) and Radio-Loud objects;
- removal of all sources with an X-ray spectroscopic photon index $\Gamma - \delta\Gamma < 1.7$ and $\Gamma + \delta\Gamma > 2.5$;
- removal of all sources with optical/UV colors outside the region defining "normal", blue quasars without significant dust absorption. The threshold are the same as in Lusso et al. (2020);

- removal of all the sources with an expected X-ray flux close to the detection limit of its observation. Sources with an intrinsic flux close to the observable limit will be detected, because of their variability, only if they are caught in a positive flux fluctuation. As less luminous quasars show more significant variability, this would affect the slope of the $L_{\rm X} - L_{\rm UV}$ relation. Again, the threshold is the one adopted in Lusso et al. (2020).

Fifteen quasars in this group described above have pointed *XMM-Newton* observations and compose the *XMM-pointed* subsample. These sources have been extensively described in the dedicated paper Nardini et al. (2019). The SDSS-XMM subsample hence amounts to 66 sources.
SDSS-Chandra 16 quasars come from the cross-match of the Sloan Digital Sky Survey quasar catalog Data Release 14 (Pâris et al., 2018) and the Chandra Source Catalog 2.0 (Evans et al., 2010). The selection is analogous to the one described above for *XMM-Newton* sources, and is fully described in Bisogni et al. (2021).
COSMOS 33 quasars come form the Chandra-COSMOS Legacy Survey (Civano et al., 2016). The sample selection, UV and X-rays fluxes are fully described in Bisogni et al. (2021).

5.2.2 *Flux and luminosities measurement*

The sources from the COSMOS and XMM-pointed subsamples have been fully described in published works (Marchesi et al., 2016; Nardini et al., 2019; Bisogni et al., 2021). We did not repeat the analysis of either the X-ray spectrum or the optical one, and we adopted the reported values.

For all the other 82 sources (66+16 from the SDSS-XMM and SDSS-Chandra subsamples), we performed a complete analysis of the SDSS optical (rest-frame UV) spectra and of the *XMM-Newton/Chandra* X-ray spectra.

For the X-ray measurements, we followed the standard procedure described in the user manuals of the two observatories, and we analyzed the spectra using the XSPEC code (Arnaud, 1996). We assumed a power-law model with Galactic photoelectric absorption. In Supplementary Figure 5.1 we show the spectra and best fit models for the golden sample sources not yet published (12 sources).

The optical SDSS spectra have been analyzed with the IDL package QSFit (Calderone et al., 2017). Using this software we modeled the features of each quasar spectrum, by assuming the continuum to be a power-law, the emission lines have a gaussians shape and the host galaxies as elliptical. The strength of this code relies in the fact that the spectrum properties are all fitted simultaneously, which avoids the fitted parameters to depends on local features of the spectrum. For each object, we derived the continuum and emission-line properties. The 2500

Å wavelength is out of range because of the redshift of these objects. Therefore, to derive the monochromatic flux at 2500 Å, we extrapolated from the continuum shape, which is assumed to be a single powerlaw and whose slope is one of the fitted parameters. In Figure 5.2 we show the resulting plots of the fit procedure described above for the golden sample sources not yet published.

Luminosity values are computed assuming a standard flat ΛCDM cosmology with $\Omega_{\rm m} = 0.3$ and $H_0 = 70$ km/s/Mpc.

5.2.3 *X-ray cross-calibration*

As the X-ray fluxes of both the *SDSS-XMM* and *SDSS-Chandra* subsamples have been obtained by spectroscopic analysis, no cross-calibration is needed in order to compare them. In principle, the *COSMOS* subsample would instead require such a calibration, as we derived the 2 keV flux densities from the soft- and hard-band fluxes available in the published catalog (Marchesi et al., 2016). Yet, we decided not to apply it.

This choice is based on two main reasons. On the one hand, we tried to estimate the parameters of cross-calibration fitting the *COSMOS* X-ray fluxes vs. the *XMM* ones for the sources appearing in both parent samples with a linear model, $\log F_{\rm XMM} + 31.5 = a(\log F_{\rm COSMOS} + 31.5) + b$. Over ≈ 1500 observations, we retrieved values of $a = 0.89$ and $b = 0.10$, which do not affect significantly our estimates of the slope, dispersion, and offset of the relation. On the other hand, the factors to be taken into account when attempting a precise cross-calibration are too many (e.g., the evolution of the *Chandra* observatory effective area over the years, the off-axis angle and duration of each observation, the intrinsic shape and variability of the source spectra) to be reliably addressed with our sample statistics.

5.2.4 *Regression analysis*

The best fit of the $\log L_{\rm X} - \log L_{\rm UV}$ relation has been performed using the Python package EMCEE (Foreman-Mackey et al., 2013), which is an implementation of Goodman & Weare's Affine Invariant Markov chain Monte Carlo (MCMC) Ensemble sampler. The UV and X-ray monochromatic luminosities were normalized to $10^{31.5}$ and $10^{27.5}$ erg s^{-1} Hz^{-1}, respectively, prior to the regression fit. For the full sample, we employed a sigma-clipping set to 2.7σ, and this choice eliminated 7 outliers.

5.3 - **Discussion**

All the 130 quasars selected at $z > 2.5$ have homogeneous UV and X-ray spectral properties, and high-quality X-ray observations. The latter requirement is key to

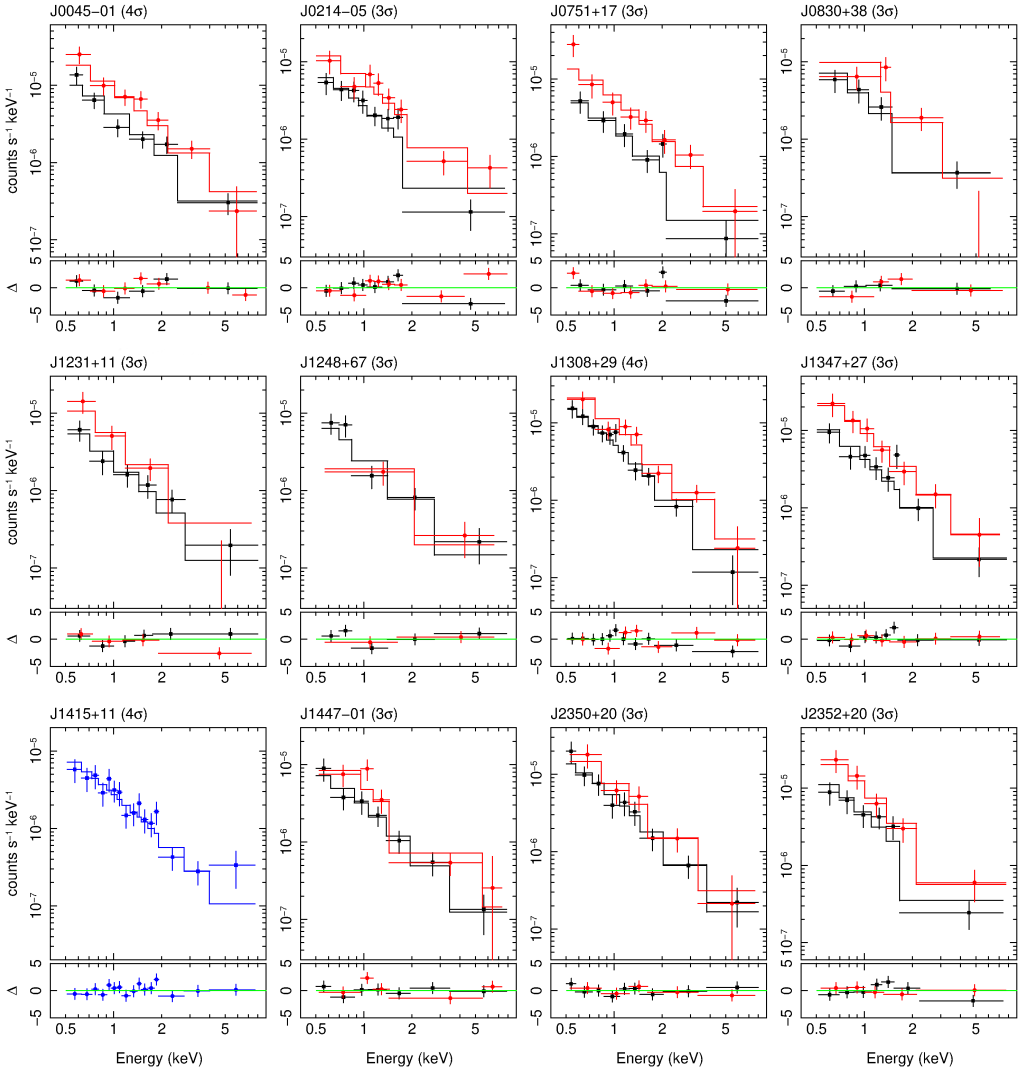

Figure 5.1: *X-ray spectra and best fit models for the 12 sources in the* $z = 3.0$-3.3 *sample with no previous analysis in the literature.*

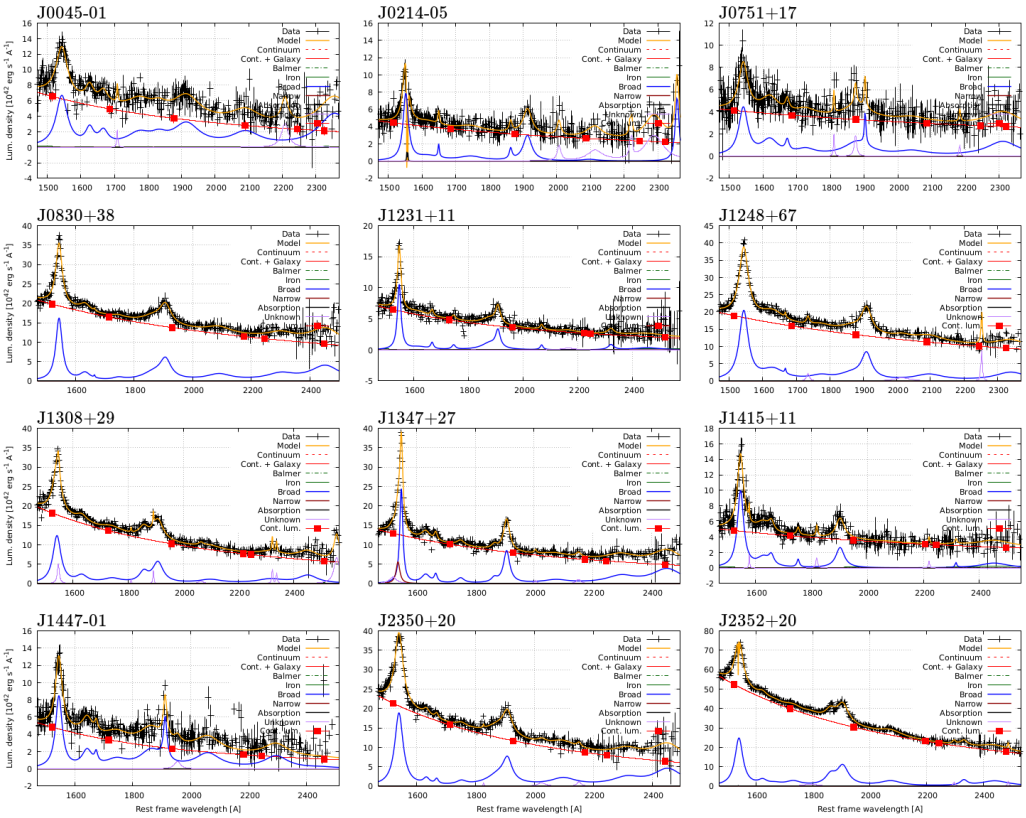

Figure 5.2: *Same as the previous figure for the SDSS optical (rest-frame UV) spectra.*

determine the overall accuracy of the distance estimates, as for all the sources in the sample the rest-frame UV data provide higher-quality flux measurements than the X-ray ones.

The results of the analysis are shown in Figure 5.3. The intrinsic dispersion δ of the $L_{\rm X} - L_{\rm UV}$ relation (i.e., the dispersion not accounted for by the statistical errors) is as low as 0.12 dex over more than three orders of magnitude in UV luminosity. This is a significant improvement with respect to the previous results ($\delta = 0.21$ Lusso et al. 2020). The best-fit slope $\gamma = 0.60 \pm 0.02$ is fully consistent with the values found at lower redshift (Lusso et al., 2020; Bisogni et al., 2021), further confirming the stability of the relation with redshift.

We note that the conversion of observed fluxes to luminosities requires a distance–redshift law. As a consequence, the relation as plotted in Figure 5.3 cannot be used to test cosmological models. However, this is not a critical issue for our purposes: here we only want to examine the relation, and the effects of using even very different cosmological models are almost entirely subsumed in the normalization parameter.

In order to obtain an even cleaner result, and to test cosmological models, we repeated our analysis for a "golden" subsample of 30 sources[1] in the narrow redshift range $z = 3.0$-3.3. This is the interval containing the group of 15 sources for which we have obtained high-quality *XMM-Newton* pointed observations (Nardini et al., 2019), which compose the *XMM-pointed* subsample. The X-ray to UV relation for this sample is shown in Figure 5.4. Here the redshift interval is narrow enough to allow the analysis of the relation using the observed fluxes as proxies of luminosities. The intrinsic dispersion is now only 0.09 dex. Considering the unaccounted dispersion due to variability (of the order of at least 0.05 dex, Paolillo et al. 2017 at these redshifts) and of the inclination of the disc (assuming that the X-ray emission is isotropic, while the UV emission is disc-like), we conclude that the relation has very little, if any, intrinsic dispersion: quasars are indeed standardizable candles.

The complete X-ray and UV spectroscopic analysis for this sample allowed us to check for possible systematic effects in the spectra, a physical redshift evolution of their intrinsic properties and/or the consequence of dust/gas absorption. The results are shown in Figure 5.5, where we overplot the rest-frame stacked X-ray and UV spectra of the *SDSS-XMM* and *SDSS-Chandra* quasars, normalized to their integral flux in the observed band (see Section 3 in Lusso et al. 2015 in for details on the stacking procedure). The stacked X-ray spectrum, with a slope $\Gamma = 1.89 \pm 0.01$, shows no deviation from the $\Gamma = 1.9$ power-law model representing the average X-ray emission of quasars (Reeves & Turner, 2000; Risaliti et al., 2009; Scott et al.,

[1]We note that no source in the "golden" sample is removed by the sigma-clipping, as no outlier is present.

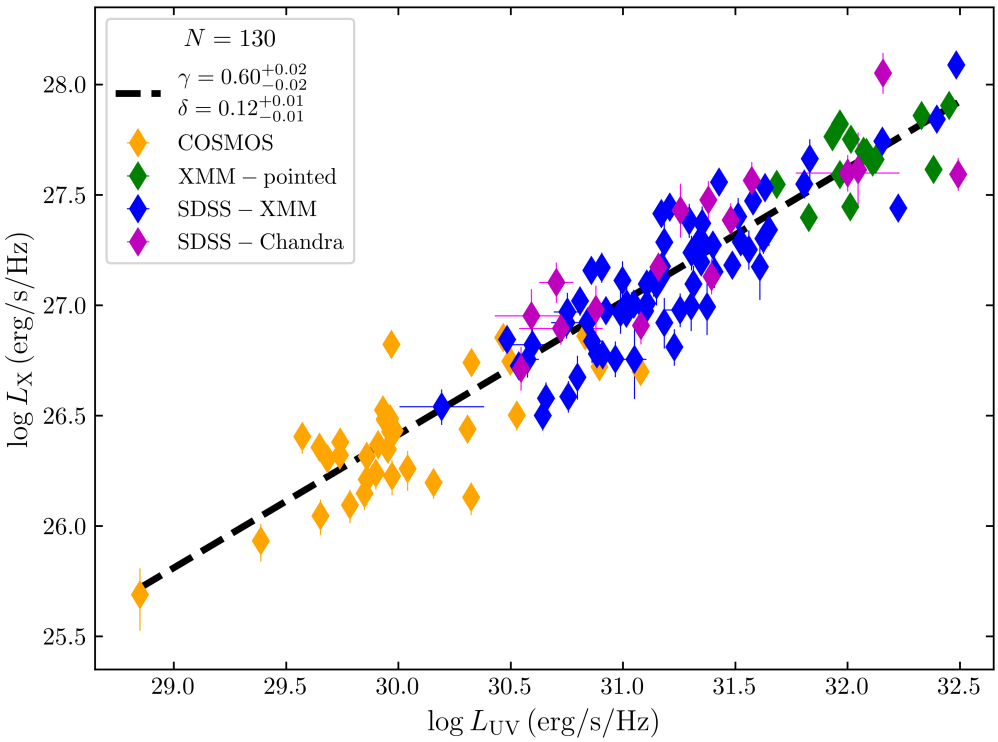

Figure 5.3: $\log L_X$ *vs* $\log L_{UV}$ *for the full* $z > 2.5$ *sample presented. Colors refer to the different subsamples, as indicated in the legend. The* γ *and* δ *symbols represent the slope and the intrinsic dispersion of the best fit relation, respectively.*

2011). Analogously in the UV, the absence of deviations amongst the individual spectra, and with respect to the average quasar spectrum of Vanden Berk et al. (2001), demonstrates that there is no systematic effect in the UV measurements. Since the latter composite spectrum is obtained from a sample of quasars in a wide redshift interval ($z = 0.044$-4.789, with a median of $z \approx 1.25$), we also demonstrate that there is no spectral evolution with redshift between local quasars (used to calibrate the relation) and those at $z \sim 3$.

5.4 - **Applications to cosmology**

The final application of the work presented here is a direct test of the flat ΛCDM model, under the physical assumption of no redshift evolution of the normalization β above $z = 1.5$ (we remind that the non-evolution of β at $z < 1.5$, and the non-evolution of the slope γ at any redshift, are observationally proven). The result in Figure 5.4 alone is not sufficient as a cosmological probe, due to the lack of

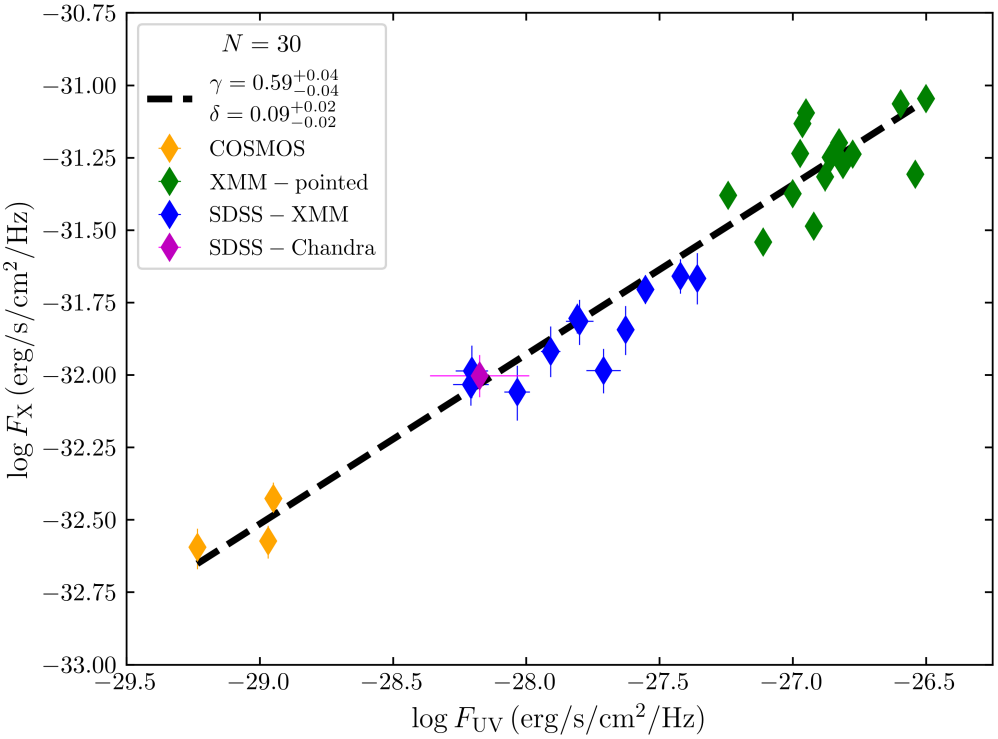

Figure 5.4: $\log F_{\rm X}$ *vs* $\log F_{\rm UV}$ *for the* $3.0 < z < 3.3$ *"golden" sample. Colors refer to the different subsamples. The green points are the group of pointed* XMM-Newton *observations.*

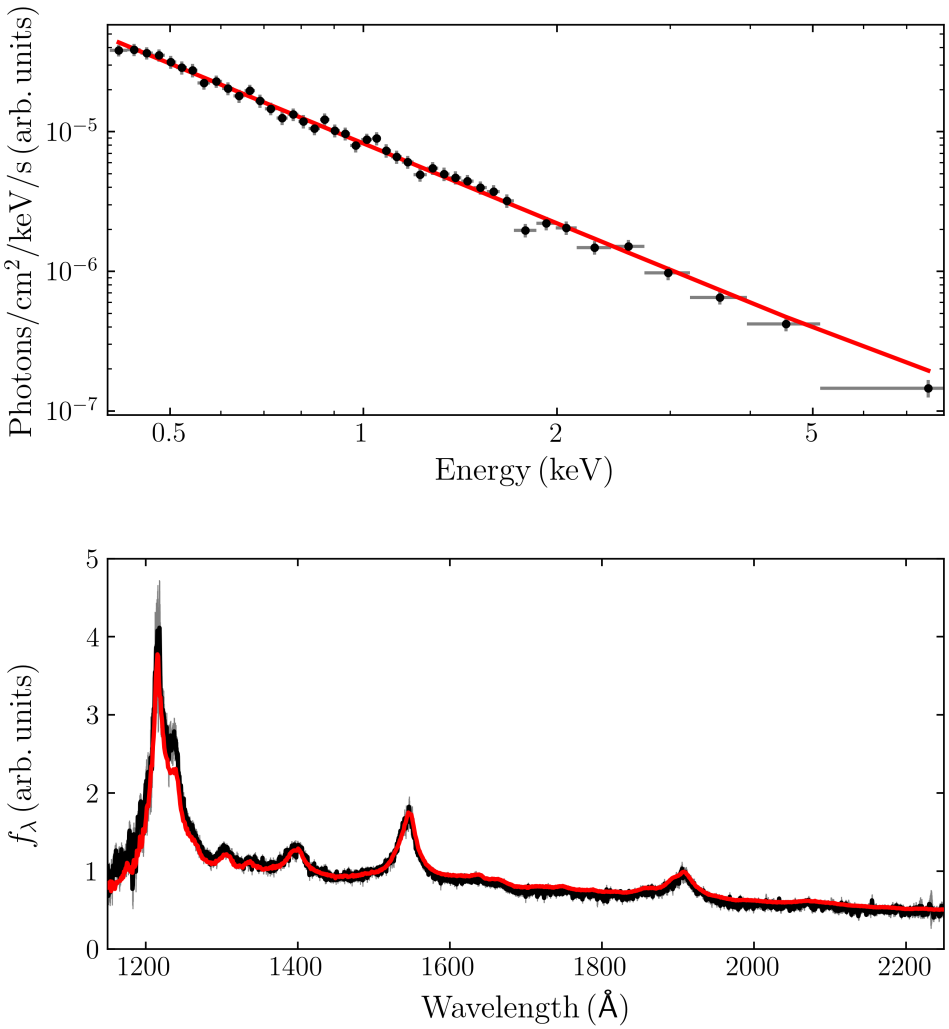

Figure 5.5: *Average X-ray and UV spectral properties of the SDSS-XMM and SDSS-Chandra subsamples in the* $z = 3.0$-3.3 *redshift range. Upper panel: stacked X-ray emission; its power law model photon index* $\Gamma = 1.89 \pm 0.01$ *is perfectly compatible with the average value of* $\Gamma = 1.9$ *of "typical" unobscured (type 1) quasars (Reeves & Turner, 2000; Risaliti et al., 2009; Scott et al., 2011) shown by the solid red line. Lower panel: stacked SDSS spectrum compared with the average quasar spectrum from a large sample of SDSS quasars over a wide redshift and luminosity range Vanden Berk et al. (2001).*

an absolute calibration of the relation. This limit can be overcome by building a Hubble diagram with supernovae, averages of quasars at $z = 0.7$-1.3, and the average for the "golden" sample (Figure 5.6). For all the quasars in this diagram, the luminosity distances are calculated from the X-ray to UV relation cross-calibrated with supernovae in the $z = 0.7$-1.3 range. The observed tension between the average luminosity distance of the "golden" sample and the prediction of the flat ΛCDM model is $> 4\sigma$. The tension between the predicted and observed luminosity distances is obtained assuming a fixed X-ray to UV luminosity ratio.

An equivalent result can be obtained by assuming a fixed cosmological model and comparing the fits with the relation at low and high redshifts. To this end, we assume a flat ΛCDM model with $\Omega_{\rm M} = 0.3$ and fit the X-ray to UV luminosity relation to the sample at $z = 0.7$-1.3 (815 quasars from Lusso et al. 2020), to the one analysed here of 130 quasars at $z > 2.5$, and the "golden" sample in the redshift interval $z = 3.0$-3.3. In all the fits we obtain a slope fully consistent within uncertainties: $\gamma = 0.588 \pm 0.020$, $\gamma = 0.590 \pm 0.030$ and $\gamma = 0.609 \pm 0.021$ for the low-redshift, the full $z > 2.5$ and the "golden" samples, respectively. If we assume no redshift evolution, we also expect the same value for the normalization parameter β. We obtain instead $\beta_{0.7-1.3} = 0.003 \pm 0.008$, $\beta_{z>2.5} = 0.145 \pm 0.024$ and $\beta_{3.0-3.3} = 0.195 \pm 0.046$, for the low-redshift, the full $z > 2.5$ and the "golden" samples, respectively. To perform the regression analysis, we have normalized $L_{\rm X}$ and $L_{\rm UV}$ to the values of luminosity such that the intercept is zero for the low-redshift sample.

The difference, $\Delta\beta$, between the intercepts of the low-redshift and the "golden" ($z = 3.0$-3.3) samples implies a $\sim 4\sigma$ deviation from the flat ΛCDM model, which increases to $> 5\sigma$ when considering the full $z > 2.5$ sample. This is shown in Figure 5.7, where the values of the intercept β of the $L_{\rm X} - L_{\rm UV}$ are plotted as a function of redshift for the low-redshift (i.e., $z = 0.7$-1.3 from Lusso et al. (2020), black square), the $2.503 < z < 4.423$, and the golden $3.0 < z < 3.3$ quasar samples analysed in the present work (red stars). The points are plotted at the average redshift value corresponding to the three quasar samples: $\langle z \rangle = 0.990$, 2.956, and 3.136 for the low-redshift, the $z > 2.5$ and the "golden" samples, respectively. The observed discrepancy is similar to that found in our previous works (e.g. Risaliti & Lusso, 2019; Lusso et al., 2019; Bargiacchi et al., 2021). We have performed the same analysis by assuming a flat wCDM model, obtaining similar findings. The important improvement is that the result presented here is based only on a sample for which a complete spectroscopic analysis directly indicates an extremely small intrinsic dispersion, and the absence of any systematic effect in the flux measurements.

A difference between the β values for the low- and the high-redshift samples was also observed by Khadka & Ratra (2021, see also Khadka & Ratra 2022), who assumed several cosmological models and analysed the $L_{\rm X}$–$L_{\rm UV}$ in different

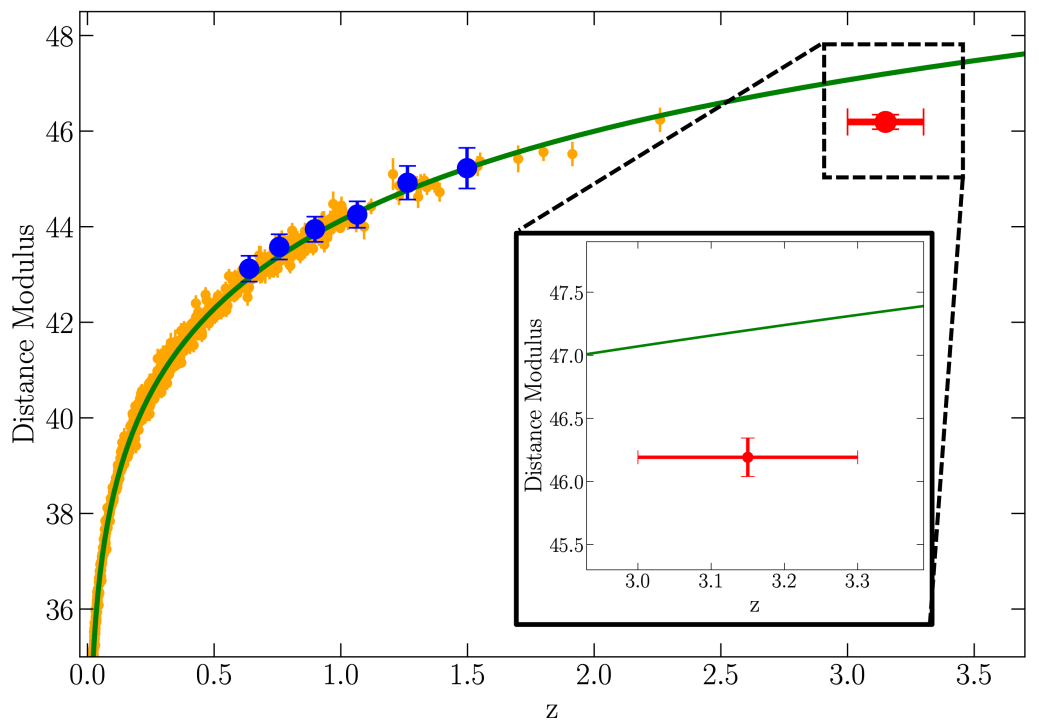

Figure 5.6: *Hubble Diagram of Pantheon supernovae (orange points) Scolnic et al. (2018), quasars at redshifts* $z = 0.7$-1.3 *(blue points), and quasars at redshifts* $z = 3.0$-3.3 *(red point). The luminosity distances for quasars are calculated using the parameters* γ *and* β *as described in the text, i.e. assuming that these parameters do not change with redshift, and adopting the best-fit flat* Λ*CDM model for supernovae. Each quasar point represents the average for all the quasars in the corresponding redshift interval.*

redshift intervals. Under the latter authors' assumptions that the $L_{\rm X}$–$L_{\rm UV}$ correlation parameters should neither evolve with redshift nor with the cosmological model, any discrepancy between the correlation parameters would be attributed to the non-standardizable nature of the quasar sample. The first assumption is valid only for the slope of the $L_{\rm X} - L_{\rm UV}$ relation, and indeed we demonstrated that the γ values between the low- and high-redshift samples are fully consistent within 1σ statistical uncertainty. The second assumption instead implies that a given cosmological model (or a set of different models) can define whether a specific dataset of astrophysical objects can be standardised for cosmological purposes. We note, however, that according to the standard scientific method any attempt to invalidate an empirical result should be data-driven, rather than resorting to any model chosen a-priori to determine the reliability of the data themselves.

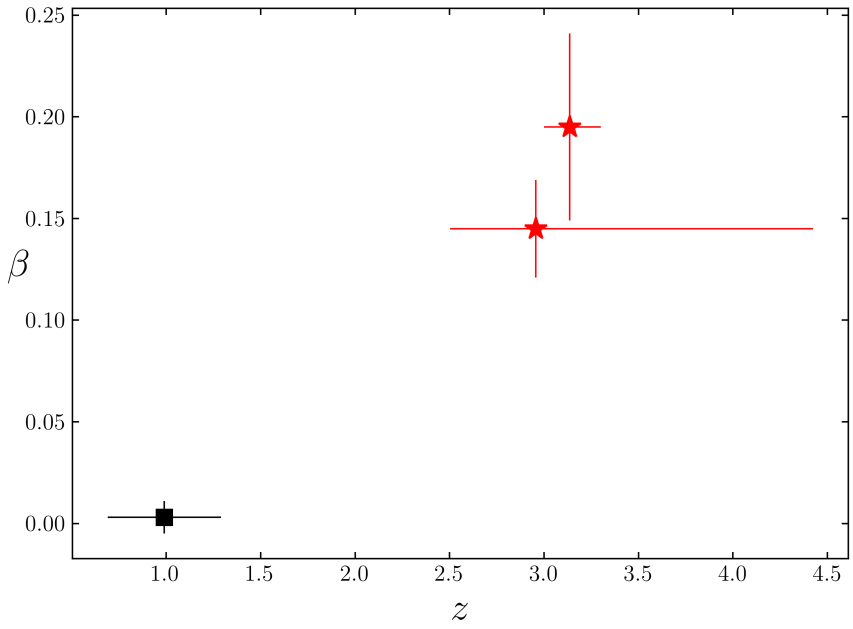

Figure 5.7: *Values of the intercept β of the $L_{\rm X} - L_{\rm UV}$ for the low-redshift (i.e., $z = 0.7$-1.3, 815 quasars from Lusso et al. 2020, black square), the $2.503 < z < 4.423$, and the "golden" $3.0 < z < 3.3$ quasar samples analysed in the present work (red stars). For the luminosity values we assumed a flat ΛCDM model ($\Omega_{\rm M} = 0.3$). The points are plotted at the average redshift of each quasar sample: $\langle z \rangle = 0.990$, 2.956, and 3.136 for the low-redshift, $z > 2.5$, and "golden" samples, respectively. The horizontal bars represent the full redshift intervals.*

5.5 - **Conclusions**

We presented a sample of 130 quasars at $z > 2.5$ for which we performed a complete X-ray and UV spectral analysis. The sample was blindly selected following our well established method that excludes absorbed and/or biased objects. We obtained the striking result of reducing the intrinsic dispersion of the luminosity relation down to $\delta \approx 0.12$ dex.

For a subsample of 30 sources at redshift $z \approx 3$ we were able to further reduce δ to 0.09 dex, thanks to the fact that in the said narrow redshift window we have high-quality pointed X-ray observations for roughly half the subsample. This single-handedly proves the robustness of the usage of quasars as standardizable candles, as an intrinsic dispersion of 0.09 dex is entirely accountable for considering quasar variability and inclination effects.

Furthermore, our work shows how crucial the possibility is of using high-quality X-ray observation for the determination of the unabsorbed X-ray flux of cosmological quasars.

Finally, we compared the normalization β of the luminosity relation computed with our $z \sim 3$ sample with respect to the one extrapolated with the flat ΛCDM model starting from a $z = 0.7$-1.3 redshift bin. We obtained a $> 4\sigma$ deviation, which is analogous to the one that can be obtained by fitting the whole Hubble diagram as we did in our previous works.

6 Conclusions

This thesis covers a wide range of scientific interest, from tidal disruption events to quasars. The red thread linking the various Chapters is the accretion onto supermassive black holes. This phenomenon is analyzed in its different time scales, from the days-months of TDEs to the years-centuries of QSOs.

This thesis is also a collection of different techniques. Theoretical/analytical arguments are supported by numerical simulations, observational investigations are carried out in multiple bands of the electromagnetic spectrum in order to grab a full picture of the studied sources, archival researches and catalog manipulation are successfully performed when statistical studies are the goal.

Chapter 1 focuses on the analytical/numerical investigation of the tidal disruption of a star in the particular scenario where a stellar rotation counter-act the tidal effects. Our main results are that no disruption actually occurs. Electromagnetic emission should however originate from such event as a result of some of the stellar material, partially stripped during the flyby, reaccreting onto the stellar core.

Interestingly the luminosity/spectral behaviour predicted by our simulations is compatible with an observed flare from our Galactic centre. This couples with the possibility of observing the survived star during a possible future flyby of “our" SMBH.

Chapter 2 is centred on the theoretical analysis of fragmentation of tidal streams. When a TDE occurs the stellar material forms a tidal stream of gas. Our analysis focused on the physical properties of said stream, with particular interest on its gravitational stability. The point was triggered by the fact that if fragmentation occurs it could reflect on the lightcurve of the TDE.

Our results shed light on the behaviour of the tidal streams and at the same time identify a satisfying criterion to determine whether a stream will collapse or not. We were able to clarify that, while in the part of stream ejected from the hole fragmentation occurs at late times, in the to-be-accreted part of the stream no fragmentation take place and hence no observational outcome is to be expected.

In particular no enhancement of the luminosity of the event and/or temporal variability is expected.

Chapter 3 addresses a slightly different issue: rather than focusing on the properties of TDEs it is centred on the archival search for undetected TDEs and other possibly interesting high-luminosity super-soft sources (peculiar AGN and/or intermediate massive black holes). The Chapter illustrates the cross-match of optical and X-ray catalogs and subsequent X-ray spectroscopic analysis of a sample of ≈ 60 sources. The power of our method is highlighted by the fact that, through a blind search, we were able to retrieve the vast majority of known TDEs and other interesting sources.

Along with these known sources we identified 9 interesting objects, 4 out of which are most promising TDE candidates. Moreover, for one sources we obtained a follow-up observation with *XMM-Newton* and we found that its luminosity has dropped by a factor 20. This, coupled with the fact that one other source show significant variability, strongly favor a TDE explanation for our sources which are the first ever TDEs identified by a pure spectroscopic analysis.

Chapter 4 is entirely QSOs-oriented. It is nested in a series of works from our group which aim to build a sample of quasars for cosmological usage. QSOs are not readily usable as standard candles, they can however be standardized thanks to the non-linear relation existing between their UV/optical and X-ray luminosities. This relation has been known for decades, but only recently, thanks to the method developed by our group and the progressive enlargement of QSO catalogs, it has been possible to apply it in order to retrieve cosmological results comparable with other well-established cosmological probes.

The Chapter goal is to present the selection procedure through which we build a new sample of cosmological QSOs, doubling the dimension of previous compilation of similar samples. We did so by including objects with photometric redshift and from the recently published eROSITA AGN catalog.

Our addition on one hand increase significantly the statistic of our sample, on the other hand allow us to test with unprecedented accuracy the robustness of our method with respect to a series of factor such as the instrument used to retrieve X-ray data, the nature (photometric or spectroscopic) of the redshift, the X-ray photon index of our sources.

Finally, Chapter 5 narrows the focus of the previous. As the physical mechanism from which the non-linear relation employed in the standardization of QSOs is still unknown, a crucial point in our method is the reduction of the relation dispersion.

In previous works the dispersion of the relations lied around 0.20-0.22 dex. Performing complete spectroscopic analysis on both the X-ray and UV/optical

spectra of sources at a narrow high-redshift bin, we were able to reduce the observed dispersion of the relation up to the astonishing result 0.09 dex. this single-handedly proves once more the robustness of our method and that a physical mechanism linking the UV/optical and X-ray emission in quasars truly exists.

Bibliography

Ahn C. P., et al., 2012, ApJS, 203, 21

Ahumada R., et al., 2019, arXiv e-prints, p. arXiv:1912.02905

Aihara H., et al., 2011, ApJS, 193, 29

Aihara H., et al., 2018, PASJ, 70, S4

Alexander T., Kumar P., 2001, ApJ, 549, 948

André P., Di Francesco J., Ward-Thompson D., Inutsuka S. I., Pudritz R. E., Pineda J. E., 2014, in Beuther H., Klessen R. S., Dullemond C. P., Henning T., eds, Protostars and Planets VI. p. 27 (arXiv:1312.6232), doi:10.2458/azu_uapress_9780816531240-ch002

Antonucci R., 1993, ARA&A, 31, 473

Arcodia R., Merloni A., Nandra K., Ponti G., 2019, A&A, 628, A135

Arcodia R., et al., 2021, Nature, 592, 704

Arnaud K. A., 1996, in Jacoby G. H., Barnes J., eds, Astronomical Society of the Pacific Conference Series Vol. 101, Astronomical Data Analysis Software and Systems V. p. 17

Auchettl K., Guillochon J., Ramirez-Ruiz E., 2017, ApJ, 838, 149

Ayal S., Livio M., Piran T., 2000, ApJ, 545, 772

Bachetti M., et al., 2014, Nature, 514, 202

Bade N., Komossa S., Dahlem M., 1996, A& A, 309, L35

Baldwin J. A., 1977, ApJ, 214, 679

Bär R. E., Weigel A. K., Sartori L. F., Oh K., Koss M., Schawinski K., 2017, MNRAS, 466, 2879

Bargiacchi G., Risaliti G., Benetti M., Capozziello S., Lusso E., Saccardi A., Signorini M., 2021, A&A, 649, A65

Barrows R. S., Mezcua M., Comerford J. M., 2019, ApJ, 882, 181

Bañados E., et al., 2017, Nature, 553, 473–476

Bisogni S., Lusso E., Civano F., Nardini E., Risaliti G., Elvis M., Fabbiano G., 2021, arXiv e-prints, p. arXiv:2109.03252

Blagorodnova N., et al., 2017, ApJ, 844, 46

Bloom J. S., et al., 2011, Science, 333, 203

Bogdanović T., Eracleous M., Mahadevan S., Sigurdsson S., Laguna P., 2004, ApJ, 610, 707

Boller T., Brandt W. N., Fabian A. C., Fink H. H., 1997, MNRAS, 289, 393

Boller T., et al., 2002, MNRAS, 329, L1

Bonnerot C., Rossi E. M., Lodato G., Price D. J., 2016, MNRAS, 455, 2253

Brandt W. N., Laor A., Wills B. J., 2000, ApJ, 528, 637

Brown G. C., Levan A. J., Stanway E. R., Tanvir N. R., Cenko S. B., Berger E., Chornock R., Cucchiaria A., 2015, MNRAS, 452, 4297

Brunner H., et al., 2021, arXiv e-prints, p. arXiv:2106.14517

Bugli M., Guilet J., Müller E., Del Zanna L., Bucciantini N., Montero P. J., 2018, MNRAS, 475, 108

Calderone G., Nicastro L., Ghisellini G., Dotti M., Sbarrato T., Shankar F., Colpi M., 2017, MNRAS, 472, 4051

Carter B., Luminet J. P., 1982, Nature, 296, 211

Carter B., Luminet J.-P., 1983, A& A, 121, 97

Castangia P., Panessa F., Henkel C., Kadler M., Tarchi A., 2013, MNRAS, 436, 3388

Cenko S. B., et al., 2012, ApJ, 753, 77

Chandrasekhar S., 1939, An introduction to the study of stellar structure. Chicago, Ill., The University of Chicago press [1939]

Chandrasekhar S., 1987, Ellipsoidal Figures of Equilibrium. Dover Books on Mathematics, Dover, https://books.google.it/books?id=EKdr1RIaQi0C

Chilingarian I. V., Katkov I. Y., Zolotukhin I. Y., Grishin K. A., Beletsky Y., Boutsia K., Osip D. J., 2018, ApJ, 863, 1

Churazov E., Khabibullin I., Sunyaev R., Ponti G., 2017, MNRAS, 465, 45

Civano F., et al., 2016, ApJ, 819, 62

Clarke T. E., Randall S. W., Sarazin C. L., Blanton E. L., Giacintucci S., 2013, ApJ, 772, 84

Colless M., et al., 2001, MNRAS, 328, 1039

Colless M., et al., 2003, arXiv e-prints, pp astro–ph/0306581

Coughlin E. R., Armitage P. J., 2018, MNRAS, 474, 3857

Coughlin E. R., Nixon C., 2015, ApJ, 808, L11

Coughlin E. R., Nixon C. J., 2019, ApJ, 883, L17

Coughlin E. R., Nixon C. J., 2020, arXiv e-prints, p. arXiv:2002.07318

Coughlin E. R., Nixon C., Begelman M. C., Armitage P. J., Price D. J., 2016a, MNRAS, 455, 3612

Coughlin E. R., Nixon C., Begelman M. C., Armitage P. J., 2016b, MNRAS, 459, 3089

Coughlin E. R., Armitage P. J., Nixon C., Begelman M. C., 2017, MNRAS, 465, 3840

Coughlin E. R., Armitage P. J., Lodato G., Nixon C. J., 2019, Space Sci. Rev., 215, 45

Del Zanna L., Matteini L., Landi S., Verdini A., Velli M., 2015, Journal of Plasma Physics, 81, 325810102

Della Valle M., Izzo L., 2020, A&A Rev., 28, 3

Donley J. L., Brandt W. N., Eracleous M., Boller T., 2002, AJ, 124, 1308

Driver S. P., et al., 2011, MNRAS, 413, 971

Duarte Puertas S., Vilchez J. M., Iglesias-Páramo J., Kehrig C., Pérez-Montero E., Rosales-Ortega F. F., 2017, A&A, 599, A71

Esquej P., Saxton R. D., Freyberg M. J., Read A. M., Altieri B., Sanchez-Portal M., Hasinger G., 2007, A&A, 462, L49

Esquej P., et al., 2008, A&A, 489, 543

Esquej P., et al., 2013, A&A, 557, A123

Evans C. R., Kochanek C. S., 1989, ApJ, 346, L13

Evans I. N., et al., 2010, ApJS, 189, 37

Farrell S. A., Webb N. A., Barret D., Godet O., Rodrigues J. M., 2009, Nature, 460, 73

Feigelson E., Townsley L., Güdel M., Stassun K., 2007, Protostars and Planets V, pp 313–328

Feng H., Tao L., Kaaret P., Grisé F., 2016, ApJ, 831, 117

Flesch E. W., 2021, arXiv e-prints, p. arXiv:2105.12985

Foreman-Mackey D., Hogg D. W., Lang D., Goodman J., 2013, PASP, 125, 306

Friedman A., 1922, Zeitschrift für Physik, 10, 377

Gafton E., Rosswog S., 2019, MNRAS, 487, 4790

Gallagher S. C., Brandt W. N., Sambruna R. M., Mathur S., Yamasaki N., 1999, ApJ, 519, 549

Gezari S., 2012, in EPJ Web Conf.. p. 03001, doi:10.1051/epjconf/20123903001

Gezari S., Halpern J. P., Komossa S., Grupe D., Leighly K. M., 2003, ApJ, 592, 42

Gezari S., et al., 2009, ApJ, 698, 1367

Gierliński M., Middleton M., Ward M., Done C., 2008, Nature, 455, 369

Giustini M., Miniutti G., Saxton R. D., 2020, A&A, 636, L2

Golightly E. C. A., Coughlin E. R., Nixon C. J., 2019, ApJ, 872, 163

Grappin R., Velli M., 1996, J. Geophys. Res., 101, 425

Green P. J., et al., 1995, ApJ, 450, 51

Guillochon J., Ramirez-Ruiz E., 2013, ApJ, 767, 25

Haardt F., Maraschi L., 1991, ApJ, 380, L51

Haardt F., Maraschi L., 1993, ApJ, 413, 507

Haardt F., Maraschi L., Ghisellini G., 1994, ApJ, 432, L95

Hayasaki K., Stone N., Loeb A., 2013, MNRAS, 434, 909

Hayasaki K., Stone N., Loeb A., 2016, MNRAS, 461, 3760

Ho L. C., Kim M., Terashima Y., 2012, ApJ, 759, L16

Holoien T. W.-S., et al., 2016, MNRAS, 455, 2918

Hung T., et al., 2017, ApJ, 842, 29

Inutsuka S.-I., Miyama S. M., 1992, ApJ, 388, 392

Jeans J. H., 1902, Philosophical Transactions of the Royal Society of London Series A, 199, 1

Jones D. H., et al., 2009, MNRAS, 399, 683

Kaaret P., Feng H., Roberts T. P., 2017, ARA&A, 55, 303

Kagaya K., Yoshida S., Tanikawa A., 2019, arXiv e-prints, p. arXiv:1901.05644

Kankare E., et al., 2017, Nature Astronomy, 1, 865

Khabibullin I., Sazonov S., Sunyaev R., 2014, MNRAS, 437, 327

Khadka N., Ratra B., 2021, MNRAS, 502, 6140

Khadka N., Ratra B., 2022, MNRAS, 510, 2753

Kochanek C. S., 1994, ApJ, 422, 508

Komossa S., 2012, in EPJ Web Conf.. p. 02001, doi:10.1051/epjconf/20123902001

Komossa S., 2015, Jo. High-Energy Astrophys., 7, 148

Kostić U., Čadež A., Calvani M., Gomboc A., 2012, in EPJ Web Conf.. p. 07004, doi:10.1051/epjconf/20123907004

Kuijken K., et al., 2019, A&A, 625, A2

La Franca F., Bianchi S., Ponti G., Branchini E., Matt G., 2014, ApJ, 787, L12

LaMassa S. M., Heckman T. M., Ptak A., 2012, ApJ, 758, 82

Lacy J. H., Townes C. H., Hollenbach D. J., 1982, ApJ, 262, 120

Lacy M., et al., 2013, ApJS, 208, 24

Landi S., Matteini L., Hellinger P., Verdini A., Travnicek P. M., Burgess D., 2014, in EGU General Assembly Conference Abstracts. p. 6884

Lavaux G., Hudson M. J., 2011, MNRAS, 416, 2840

Law-Smith J., Guillochon J., Ramirez-Ruiz E., 2019, ApJ, 882, L25

Lidman C., et al., 2016, PASA, 33, e001

Lin D., Carrasco E. R., Grupe D., Webb N. A., Barret D., Farrell S. A., 2011, ApJ, 738, 52

Lin D., Irwin J. A., Godet O., Webb N. A., Barret D., 2013, ApJ, 776, L10

Lin D., et al., 2015, ApJ, 811, 43

Lin D., et al., 2016, ApJ, 821, 25

Lin D., et al., 2017a, Nature Astronomy, 1, 0033

Lin D., Godet O., Ho L. C., Barret D., Webb N. A., Irwin J. A., 2017b, MNRAS, 468, 783

Liptai D., Price D. J., Mandel I., Lodato G., 2019, arXiv e-prints, p. arXiv:1910.10154

Liske J., et al., 2015, MNRAS, 452, 2087

Liu F. K., Li S., Chen X., 2009, ApJ, 706, L133

Liu Z., et al., 2016, MNRAS, 459, 1602

Liu T., et al., 2021, arXiv e-prints, p. arXiv:2106.14522

Lodato G., 2012, in European Physical Journal Web of Conferences. p. 01001 (arXiv:1211.6109), doi:10.1051/epjconf/20123901001

Lodato G., Rossi E. M., 2011, MNRAS, 410, 359

Lodato G., King A. R., Pringle J. E., 2009, MNRAS, 392, 332

Lusso E., 2020, Frontiers in Astronomy and Space Sciences, 7, 8

Lusso E., Risaliti G., 2016, ApJ, 819, 154

Lusso E., Risaliti G., 2017, A&A, 602, A79

Lusso E., et al., 2010, A&A, 512, A34

Lusso E., Worseck G., Hennawi J. F., Prochaska J. X., Vignali C., Stern J., O'Meara J. M., 2015, MNRAS, 449, 4204

Lusso E., Piedipalumbo E., Risaliti G., Paolillo M., Bisogni S., Nardini E., Amati L., 2019, A&A, 628, L4

Lusso E., et al., 2020, A&A, 642, A150

Lyke B. W., et al., 2020, ApJS, 250, 8

Maksym W. P., et al., 2014, The Astronomer's Telegram, 6834, 1

Mallick L., Dewangan G. C., 2018, ApJ, 863, 178

Marchesi S., et al., 2016, ApJ, 817, 34

Melnyk O., et al., 2013, A&A, 557, A81

Menzel M. L., et al., 2016, MNRAS, 457, 110

Merloni A., 2003, MNRAS, 341, 1051

Merloni A., et al., 2012, arXiv e-prints, p. arXiv:1209.3114

Mickaelian A. M., Harutyunyan G. S., Sarkissian A., 2018, Astronomy Letters, 44, 351

Middleton M. J., Sutton A. D., Roberts T. P., Jackson F. E., Done C., 2012, MNRAS, 420, 2969

Middleton M. J., Heil L., Pintore F., Walton D. J., Roberts T. P., 2015, MNRAS, 447, 3243

Miniutti G., Fabian A. C., Brandt W. N., Gallo L. C., Boller T., 2009, MNRAS, 396, L85

Miniutti G., Saxton R. D., Rodríguez-Pascual P. M., Read A. M., Esquej P., Colless M., Dobbie P., Spolaor M., 2013, MNRAS, 433, 1764

Miniutti G., et al., 2019, Nature, 573, 381

Mortlock D. J., et al., 2011, Nature, 474, 616–619

Nardini E., et al., 2019, A&A, 632, A109

Nealon R., Price D. J., Bonnerot C., Lodato G., 2018, MNRAS, 474, 1737

Nicastro F., 2000, ApJ, 530, L65

Nolthenius R. A., Katz J. I., 1982, ApJ, 263, 377

Ostriker J., 1964, ApJ, 140, 1056

Paolillo M., et al., 2017, MNRAS, 471, 4398

Pâris I., et al., 2014, A&A, 563, A54

Pâris I., et al., 2018, A&A, 613, A51

Paturel G., Petit C., Prugniel P., Theureau G., Rousseau J., Brouty M., Dubois P., Cambrésy L., 2003, A&A, 412, 45

Peebles P. J. E., 1980, The large-scale structure of the universe. Princeton University Press

Phinney E. S., 1989, in Morris M., ed., IAU Symposium Vol. 136, The Center of the Galaxy. p. 543

Piconcelli E., Jimenez-Bailón E., Guainazzi M., Schartel N., Rodríguez-Pascual P. M., Santos-Lleó M., 2005, A&A, 432, 15

Pierre M., et al., 2016, A&A, 592, A1

Pinto C., et al., 2017, MNRAS, 468, 2865

Predehl P., et al., 2021, A&A, 647, A1

Price D. J., et al., 2017, PHANTOM: Smoothed particle hydrodynamics and magnetohydrodynamics code, Astrophysics Source Code Library (ascl:1709.002)

Rakshit S., Stalin C. S., Chand H., Zhang X.-G., 2017, ApJS, 229, 39

Rees M. J., 1988, Nature, 333, 523

Reeves J. N., Turner M. J. L., 2000, Monthly Notices of the Royal Astronomical Society, 316, 234

Ricci C., et al., 2020, ApJ, 898, L1

Risaliti G., Lusso E., 2015, ApJ, 815, 33

Risaliti G., Lusso E., 2019, Nature Astronomy, 3, 272

Risaliti G., Young M., Elvis M., 2009, ApJ, 700, L6

Ryu T., Krolik J., Piran T., Noble S. C., 2020, arXiv e-prints, p. arXiv:2001.03501

Sacchi A., Lodato G., 2019, MNRAS, 486, 1833

Sacchi A., Lodato G., Toci C., Motta V., 2020, MNRAS, 495, 1227

Salvato M., et al., 2021, arXiv e-prints, p. arXiv:2106.14520

Saxton R. D., Read A. M., Esquej P., Komossa S., Dougherty S., Rodriguez-Pascual P., Barrado D., 2012, A&A, 541, A106

Saxton R., Komossa S., Auchettl K., Jonker P. G., 2021, Space Sci. Rev., 217, 18

Scolnic D. M., et al., 2018, ApJ, 859, 101

Scott A. E., Stewart G. C., Mateos S., Alexander D. M., Hutton S., Ward M. J., 2011, MNRAS, 417, 992

Shakura N. I., Sunyaev R. A., 1973, A& A, 24, 337

Shectman S. A., Landy S. D., Oemler A., Tucker D. L., Lin H., Kirshner R. P., Schechter P. L., 1996, ApJ, 470, 172

Shen Y., et al., 2011, ApJS, 194, 45

Sheng Z., Wang T., Ferland G., Shu X., Yang C., Jiang N., Chen Y., 2021, ApJ, 920, L25

Shu X. W., Wang T. G., Jiang N., Wang J. X., Sun L. M., Zhou H. Y., 2017, ApJ, 837, 3

Shu X. W., Wang S. S., Dou L. M., Jiang N., Wang J. X., Wang T. G., 2018, ApJ, 857, L16

Stone N. C., Vasiliev E., Kesden M., Rossi E. M., Perets H. B., Amaro-Seoane P., 2020, Space Sci. Rev., 216, 35

Sun L., Shu X., Wang T., 2013, ApJ, 768, 167

Svirski G., Piran T., Krolik J., 2017, MNRAS, 467, 1426

Tananbaum H., et al., 1979, ApJ, 234, L9

Tejeda E., Gafton E., Rosswog S., Miller J. C., 2017, MNRAS, 469, 4483

Terashima Y., Kamizasa N., Awaki H., Kubota A., Ueda Y., 2012, ApJ, 752, 154

Toba Y., et al., 2014, ApJ, 788, 45

Toci C., Galli D., 2015, MNRAS, 446, 2110

Toci C., Galli D., Verdini A., Del Zanna L., Landi S., 2018, MNRAS, 474, 1288

Urquhart R., Soria R., 2016, MNRAS, 456, 1859

Urry C. M., Padovani P., 1995, PASP, 107, 803

Vanden Berk D. E., et al., 2001, AJ, 122, 549

Véron-Cetty M. P., Véron P., 2006, A&A, 455, 773

Véron-Cetty M. P., Véron P., 2010, A&A, 518, A10

Vigneron Q., Lodato G., Guidarelli A., 2018, MNRAS, 476, 5312

Wang J.-M., Du P., Valls-Gabaud D., Hu C., Netzer H., 2013, Phys. Rev. Lett., 110, 081301

Wang F., et al., 2021, ApJ, 907, L1

Watson M. G., et al., 2001, A&A, 365, L51

Webb N. A., et al., 2020, arXiv e-prints, p. arXiv:2007.02899

Weymann R. J., Morris S. L., Foltz C. B., Hewett P. C., 1991, ApJ, 373, 23

Wilkes B. J., Elvis M., 1987, ApJ, 323, 243

Yoon J. H., Schawinski K., Sheen Y.-K., Ree C. H., Yi S. K., 2008, ApJS, 176, 414

Zamorani G., et al., 1981, ApJ, 245, 357

Zauderer B. A., et al., 2011, Nature, 476, 425

Zhang W., Yu W., Yan Z., 2016, The Astronomer's Telegram, 8644, 1